People's Democratic Republic of Algeria
Ministry of Higher Education & Scientific Research

National Polytechnic School
Process Control Laboratory

This dissertation is submitted for the degree of:

Doctor of Science

In
Electrical Engineering
Specialty : Automatic

By

Boudjana Said

Control and Supervision of a Photovoltaic Pumping Station Based on Multicell Inverter Topologies

Examined on: 07/10/2021 by a committee composed of:

President:	Mr. Boucherit Mohamed Seghir	Professor, ENP
Supervisor:	Mr. Tadjine Mohamed	Professor, ENP
Co-supervisor:	Mr. Deneai Mouloud	Doctor, Hertfordshire (UK)
	Mr. Bali Noureddine	Professor, USTHB
	Mr. Benmansour Khalifa	Professor, ESDAT
Examiners:	Mr. Bouchhida Ouahid	Professor, Univ, Media
	Mr. Chakir Messaoud	MCA, ENP

– ENP 2021 –

People's Democratic Republic of Algeria
Ministry of Higher Education & Scientific Research

National Polytechnic School
Process Control Laboratory

This dissertation is submitted for the degree of:

Doctor of Science

In
Electrical Engineering
Specialty : Automatic

By

Boudjana Said

Control and Supervision of a Photovoltaic Pumping Station Based on Multicell Inverter Topologies

Examined on: 07/10/2021 by a committee composed of:

President:	Mr. Boucherit Mohamed Seghir	Professor, ENP
Supervisor:	Mr. Tadjine Mohamed	Professor, ENP
Co-supervisor:	Mr. Deneai Mouloud	Doctor, Hertfordshire (UK)
	Mr. Bali Noureddine	Professor, USTHB
	Mr. Benmansour Khalifa	Professor, ESDAT
Examiners:	Mr. Bouchhida Ouahid	Professor, Univ, Media
	Mr. Chakir Messaoud	MCA, ENP

– ENP 2021 –

REPUBLIQUE ALGERIENNE DEMOCRATIQUE ET POPULAIRE

Ministère de l'Enseignement Supérieur et de la Recherche Scientifique

Ecole Nationale Polytechnique
Laboratoire de Commande des Processus

Thèse de Doctorat en science
Spécialité : Automatique

Présenté par :

Boudjana Said

Commande et supervision d'une station de pompage photovoltaïque à base de convertisseur multicellulaire

---

Soutenue publiquement le: 07/10/2021, devant le jury composé de:

Président:	Mr. Boucherit M. Seghir	Professeur, ENP S
Directeur de thèse:	Mr. Tadjine Mohamed	Professeur, ENP
Co- Encadreur:	Mr. Deneai Mouloud	Docteur, Hertfordshire (UK)
	Mr. Bali Noureddine	Professeur, USTHB
	Mr. Benmansour Khalifa	Professeur, ESDAT
Examinateurs:	Mr. Bouchhida Ouahid	Professeur, Univ, Media
	Mr. Chakir Messaoud	MCA, ENP

– ENP 2021 –

ملخص:

في هذه الأطروحة تم تطوير محكم قوي جديد للعاكسات متعددة الخلايا. بحيث أخذ بعين الاعتبار الطبيعة الهجينة لهذا العاكس ، التي يمثلها وجود ديناميكيات مستمرة ومنفصلة ، في أجزاء تصميم النمذجة والتحكم. في البداية تم تصميم وبناء محكم في تشكيل الحلقة (LSC) للتحكم في محول التيار المباشر (DC/DC) لزيادة الكسب العالي مع نقطة وسطية لتوليد النبضات لتزويد العاكس. بعد ذلك ، باشرنا بتطوير محكم جديد في تشكيل الحلقة الهجينة القوية المتتالية لعاكس ثلاثي الخلايا. ثم مناقشة النموذج الهجين للعاكس بالتفصيل. وقد خلصنا إلى تطوير الديناميكيات المستمرة لكل وضع و تحديد مستوى جهد الخرج الأساسي. ثانيًا ، تمت دراسة قيد التقارب للانتقال بين الأنماط الهجينة وتم اقتراح حالة جبرية جديدة من أجل الوفاء بهذا القيد. علاوة على ذلك، اقتراحنا خوارزمية هجينة جديدة من أجل ضمان موازنة توزيع جهد المكثفات العائمة في هذه الخوارزمية ، وكذلك التحكم في حالات العاكس مباشرة من خلال جدول اختيار محدد مسبقًا. تتمثل مزايا هذا التحكم الهجين في تقليل وقت التنفيذ من خلال اعتماد المعالجة المتوازية وخصائص المتانة الذاتية.

من أجل تحسين أداء وكفاءة النظام الكهروضوئي ، تم تقديم وحدة تحكم في الوضع الانزلاقي التسلسلي (SMC) لنظام GPV لتنظيم التيار من النظام الكهروضوئي إلى حمل العاكس. أخيرًا ، و من أجل التحقق من الخوارزمية الجديدة واختبارها ، تمت دراسة تطبيق العاكس في الضخ الشمسي باستخدام محرك تحريضي ثلاثي الطور (IM) مقترنًا بحمل مضخة طرد مركزي.

الكلمات الدالة: الحد الأقصى لتتبع نقطة الطاقة (MPPT)، محول التعزيز(DC-DC)، تحكم حلقة تشكيل، عاكس متعدد الخلايا، نظام هجين، التحكم بطريقة انزلاقية، محرك لاتزامني ثلاثي الطور، أنظمة الضخ الكهروضوئية المستقلة.

Résumé :

Ce travail porte sur le développement d'une nouvelle commande robuste d'onduleurs multicellulaires. La nature hybride de cet onduleur, représentée par la présence de dynamiques continues et discrètes, est prise en considération durant la phase de modélisation et de conception de la commande. Pour cela, une commande par Loop-Shaping (LSC) a été conçue et développée pour contrôler un convertisseur de courant continu (DC / DC) à gain élevé avec un point médian pour générer les impulsions de commande de l'onduleur. Ensuite, une nouvelle commande de LS robuste hybride en cascade d'un onduleur à trois cellules est développée. Le modèle hybride de l'onduleur est discuté en détail. La dynamique continue pour chaque mode est développée et le niveau de tension de sortie sous-jacent est déterminé. Dans un second temps, la contrainte d'adjacence pour la transition entre modes hybrides est étudiée et une nouvelle condition algébrique est proposée afin de satisfaire cette contrainte. De plus, un nouvel algorithme hybride est proposé afin d'assurer une répartition équilibrée des tensions des condensateurs volants. Dans cet algorithme, les états de l'onduleur sont directement contrôlés via une table de sélection prédéfinie. Les principaux avantages de cette commande hybride sont la réduction du temps d'exécution en adoptant des propriétés de traitement parallèle et de robustesse intrinsèque.

Afin d'améliorer les performances et l'efficacité du système PV, un contrôleur à mode glissant en cascade (SMC) est proposé afin de réguler le courant du système PV à la charge de l'onduleur. Enfin, pour vérifier et tester le nouvel algorithme, une application de l'onduleur en pompage solaire est mise en œuvre à l'aide d'un moteur à induction triphasé (IM) couplé à une pompe centrifuge.

Mots-clés : Poursuite du point de puissance maximale (MPPT), Convertisseur boost DC-DC, Commande Loop-Shapin, Onduleur multicellulaire, Système hybride, Commande par Mode de Glissement, Moteur asynchrone triphasé, systèmes de pompage PV autonomes.

Abstract:

This work relates to the development of a new robust control approach for multi-cell inverters. The hybrid nature of this inverter, represented by the presence of continuous and discrete dynamics, is taken into account in the modeling and control design parts. First, a Loop-Shaping Control (LSC) is designed to control a high gain DC/DC boost converter with a midpoint to generate the pulses for supplying the inverter. Next, a new cascaded hybrid robust loop shaping control of three cell inverter is developed. The hybrid model of the inverter is discussed in details. The continuous dynamics for each mode is developed and the underlying output voltage level is determined. Secondly, a new algebraic condition is proposed in order to fulfill this constraint. Furthermore, a hybrid automata defining all possible transitions respecting the adjacency rule is given. Then, a new hybrid algorithm is proposed in order to ensure a balanced distribution of the flying capacitors voltages. In this algorithm, the states of the inverter are directly controlled through a predefined selection table. The advantages of this hybrid control are the reduction of the execution time by adopting parallel processing and its intrinsic robustness properties.

In order, to improve the performance and efficiency of the Photovoltaic (PV) system, a cascade sliding mode controller (SMC) is proposed to regulate the current from the PV system to the load of the inverter. Finally, this new control structure is applied to a solar pumping inverter driving a three-phase induction motor (IM) coupled to a centrifugal pump load.

Keywords: Maximum Power Point Tracking (MPPT), DC-DC boost converter, Loop-Shaping controller, Multicell inverter, Hybrid system, Sliding mode control, Three-phase induction motor, stand-alone PV pumping systems.

Acknowledgements

<div dir="rtl">

رَبِّ أَوْزِعْنِيٓ أَنْ أَشْكُرَ نِعْمَتَكَ ٱلَّتِيٓ أَنْعَمْتَ عَلَىَّ وَعَلَىٰ وَٰلِدَىَّ وَأَنْ أَعْمَلَ صَٰلِحًا تَرْضَىٰهُ وَأَدْخِلْنِي بِرَحْمَتِكَ فِي عِبَادِكَ ٱلصَّٰلِحِينَ

</div>

My Lord, inspire me that I should be thankful for Your blessing with which You have blessed me and my parents, and that I may do good works that will please You. Admit me, by Your Mercy, among Your righteous worshipers.

Table of contents

List of figures

List of tables

Nomenclature

Abbreviation

ADALINE	Adaptive Linear Neuron.
CHB	Cascade H-Bridge Converter.
ESP	Electrical Submersible Pump.
FC	Flying Capacitor.
GPV	Photovoltaic Generator.
HSMC	Hybrid Sliding Mode Control.
IFOC	Iderict Field-Oriented Control
IM	Induction Motor.
LS	Loop Shaping.
MMC	Modular Multilevel Converter.
MPPT	Maximum Power Point Traking.
NPC	Neutral Point Converter.
PWM	Pulse Width Modulation.
NPSH	Net Positive Suction Head.
RCC	Ripple Correlation Control.
SMC	Sliding Mode Control.
SPV	Stand-Alone PV.
P&O	Perturb & Observe.
THD	Total Dynamic Head.

Symbols

ω_{Bp}	rad/s	Frequency range.
ΔG		Modeling error.
d_i		Input perturbation.
C_{dc}		dc-link capacitance.
d_o		measurement errors.
e_i		Current error.
e_{vi}		Voltage error.
G_N		Nominal transfer function.
G_{VD}		Transfer function from Duty Ratio to Output voltage.
I_L	A	Load current .
I_{ref}	A	Reference current.
J	kg/m^2	Inertia.
q_i		Modes.
S_k		Switches.
v_L	V	Input voltage.
V_o	V	Inverter output voltage.
α		Levels.
η_M		Efficiency Motor.
η_{Mp}		Efficiency Motor-Pump.
η_p		Efficiency Pump.
ω_n	rad/s	Mechanical speed of the rotor.
ρ	kg/m^3	Density of fluid.
f_e	m	Fittings.
F_l	m	Friction loss.
g	m/s^2	acceleration of gravity.
H	m	Differential head.
L_t	m	Total length of pipe.
n_f		Number of same fittings.
P		Number of poles pair.
P_e	W	Electrical power
P_H	W	Hydraulic power
P_l	m	Pumping level
P_{SH}	W	Shaft power
Q	m^3/H	Flow of water
S		sensitivity
$S(x)$		Sliding surface.
T		complimentary sensitivity.
T_e	Nm	Electromechanical torque.
T_L	Nm	Load torque.
V_i		Lyapunov function.
V_r	m	Vertical rise.
V_{ref}	V	Voltage reference.
u_{eq}		equivalent control.
u_n		nonlinear control.

Chapter 1

Introduction

Chapter 1

Introduction

1.1 Motivation

Global demand for energy has become increasingly important, as evidenced by the rise in energy consumption. Electrical energy converted into one form or another through power electronics which is are growing exponentially today. The development of new semiconductor devices and power converter topologies which are able to produce, efficiently, all of the required energy have become essential.

Modular Multilevel Converter (MMC) is currently the most promising topology for medium / high power applications due to their high efficiency, high-quality waveforms, and flexible scalability [78, 101]. Since its early design in 2001, the MMC attracted attention of both industrial and academic research communities [142, 8, 35].

The most popular multilevel converter topologies are the Neutral Point Clamped (NPC), the Flying Capacitor (FC) and the Cascaded H-Bridge (CHB) [44, 120].

Among these converters, flying capacitor multi-cell inverters design based on series association of elementary commutation cells are well studied for applications in renewable energy conversion or generation. The multi-cell converter has emerged in the early 90's and became one of the most widely used topology because of their high input voltage range, thus, they can be used in large size solar fields [80, 74]. The multi-cell nature of these inverters offers a very high energy efficiency over a very wide range of power with the appropriate choice of the number of cells to be used in the circuit. This is an indisputable advantage for conversion applications for renewable energy systems [68, 67, 31, 119].

Solar pumping is one of the promising applications of the use of multicell converters. It is a very interesting alternative for supplying isolated sites with water.

This advantage is counterbalanced by the complexity of control due to the significant increase
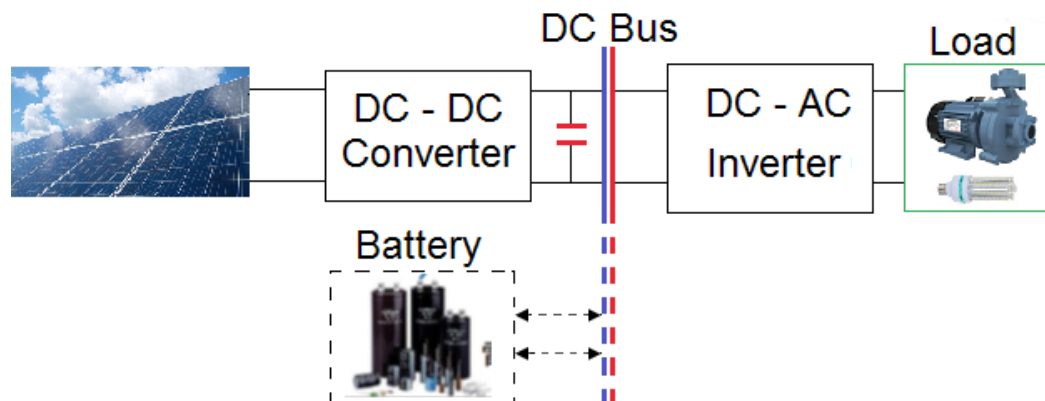
Fig. 1.1 Stand-Alone PV System

in the number of variables to be controlled in this complex system structure. The coupling between cells, which leads to further improvements in the system performance, adds to this complexity. The modeling of the whole system; dc/dc, inverters and load are generally difficult. Indeed, it contains continuous variables (voltages and currents) and discrete variables (switches, or a discrete location). In order to maintain proper operation of an inverter over time, a control must regulate the voltages and distribute the stresses equitably on each switch on the one hand, and on the other hand keep the same characteristics of the switch point.

Stand-Alone PV System

A stand-alone photovoltaic (PV) system is an off-grid system that can be used to power communication systems, air services, hospitals, and remote sites..., it can do so without the need for another source of power (Fig. 1.1) [38, 46, 130].

A typical stand-alone PV system consists of solar panels, power components, and a storage device (batteries). However, the battery's main disadvantage in stand-alone PV systems is its high cost and bulky size. As a result, some stand-alone topologies have made use of a PV system without a battery as in our work.

Regarding a power stage, stand-alone photovoltaic (PV) systems can be one or two stages, in terms of power. A two-stage inverter configuration used a boost converter followed by an inverter as shown in Fig. 1.2. Hence, in single stage inverter configurations, the PV generator is connected directly to the inverter, removing a DC / DC boost converter (Fig. 1.3). Due to its lower weight, higher efficiency, and smaller size, the single-stage PV configuration is the most promising technology [146, 64, 151]. As a result, there is a current trend towards the adoption of single-stage inverter configurations.
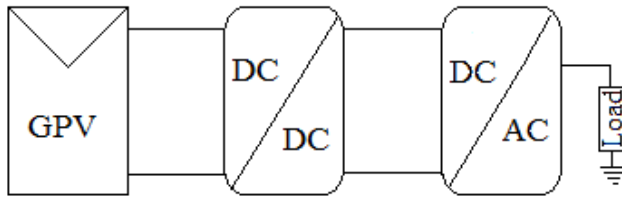
Fig. 1.2 Dual-stage inverter.   Fig. 1.3 One stage inverter.
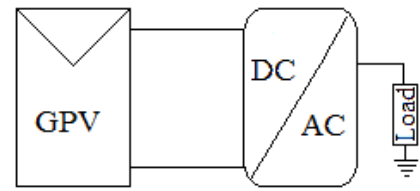
1.2   Objectives of the research project

This research work aims to develop a new robust control of multicell inverters in order, to improve the stability and dynamic performance of PV systems. It should be noted that a photovoltaic water pumping system is not the goal of this research, it is just an application. A simulation study has been carried out using the simulation software PSim.

1.3   Major Contributions and Outline of the Dissertation

The most significant contributions of this thesis are summarized as follows: Apart the Introduction (this chapter), the thesis is composed of different chapters according to the following organization:

Chapter 2: The purpose of this chapter is to design, build, and control a new direct current (DC / DC) converter for use in PV power system applications. This chapter is made up of four parts: the first part is devoted to the transfer of the maximum power to the load (MPPT), the second part focuses on the DC / DC converter, the third part will study the method of control of the dc / dc and the last part present the simulations results and discussions.

The control objectives of this system are divided into two stages. The first is for the DC/DC converter where the MPPT control algorithm is responsible for extracting the maximum energy and the second control is the Loop-Shaping strategy for controlling the high gain boost converter with a midpoint to generate the impulses.

Although the actual incorporation of energy storage is outside the scope of this thesis, a provision to include optional energy storage will also be investigated. In this work, PSim (Powersim) is used to implement the PV system model , power converters and relevant controllers. It gives the possibility of implementing algorithms easily using blocks in C language.

Chapter 3: In this chapter, a robust loop shaping control of three cell inverter is proposed. The hybrid nature of this inverter, represented by the presence of continuous and discrete dynamics, is taken into account in the modeling and control design parts. Firstly, the instantaneous inverter model is derived and the control problem is formulated as a two cascaded current/voltages loops. Then, the hybrid model of the inverter is discussed in details. The continuous dynamics for each mode is developed and the underlying output voltage level is determined. Secondly, the adjacency constraint for the transition between hybrid modes is studied and a new algebraic condition is proposed in order to fulfill this constraint. Furthermore, a hybrid automata defining all possible transitions respecting the adjacency rule is given. Thirdly, the controller synthesis of the current loop is transformed to a robust control problem and then it is designed offline using loop shaping method in order to ensure robust stabilization of the load current in the presence of load parametric variations and measurement errors. Fourthly, a new hybrid algorithm is proposed in order to ensure balancing of the flying capacitors voltages. In this algorithm, the states of the inverter are directly controlled through a predefined selection table. The major advantages of this hybrid control are the reduction of the execution time by adopting parallel processing and intrinsic robustness properties. Asymptotic stability of the underlying tracking errors is proven using Lyapunov theory. Finally, a virtual experimental setup based on Power Sim software is performed in order to emulate the realistic behavior of the nonlinear inverter elementary elements. The results obtained show that the designed controller is able to successfully meet the design objectives.

Chapter 4: In order to enhance performance and efficiency of the new hybrid control studied in the previous chapter, two controllers are proposed. The first controller is used to improve the efficiency and track the maximum power point of photovoltaic generator under variable irradiance and load conditions. The second controller is a cascaded sliding mode control (SMC) to regulate the current loop while the hybrid control is used for the voltage loop. The proposed controller will be applied to the PV generator (GPV) to satisfy the necessary load requirements .

Chapter 5: To test the performance and stability of the newly designed hybrid control, this strategy will be implemented in a PV-powered water pumping system. The system consists of a submersible pump connected to a three-phase squirrel cage induction motor (IM) driven by a multicell voltage inverter. The overall control scheme consists of two control loops. The first controller is the RCC algorithm which aims to improve the efficiency at the point of maximum power of the GPV system; this algorithm is coupled with the Indirect

Field Oriented Control (IFOC) technique to generate a variable frequency PWM signal to control the IM Motor.

Chapter 6: Conclusion and Perspectives : The main conclusion of this dissertation, summarize the whole thesis and provides some potential recommendations for future research work.

Chapter 2

Loop-shaping control of a DC-DC boost converter

Chapter 2

Loop-shaping control of a DC-DC boost converter

2.1 Introduction

The purpose of this chapter is to design, build, and control a new direct current (DC / DC) converter for use in PV power system applications. This chapter is made up of four parts: the first part is devoted to the transfer of the maximum power to the load (MPPT), the second part will be focused on the converter DC/DC, the third part will study the method of control of the dc / dc and the last part will deal with simulations and results.

The control objectives of this system are divided into two stages. The first is for the DC/DC converter where the MPPT control algorithm is responsible for extracting the maximum energy and the second control is the Loop-Shaping command to control a high gain boost converter with a midpoint to generate the impulses.

A provision to include optional energy storage will also be considered, although the actual incorporation of energy storage is outside the scope of this thesis.

PSIM software has been used to achieve this objective. It is a complete modeling tool oriented towards power electronics. It gives the possibility of implementing algorithms easily using blocks in C language.

2.2 MPPT control

The V-I characteristic of the solar cell is non-linear and varies with irradiation and temperature. In general, there is a single point on the V-I or V-P curve, called Maximum Power Point

(MPP), where the entire PV system (generator, converter, etc.) operates with maximum efficiency and produces its maximum output power (Fig 2.1).
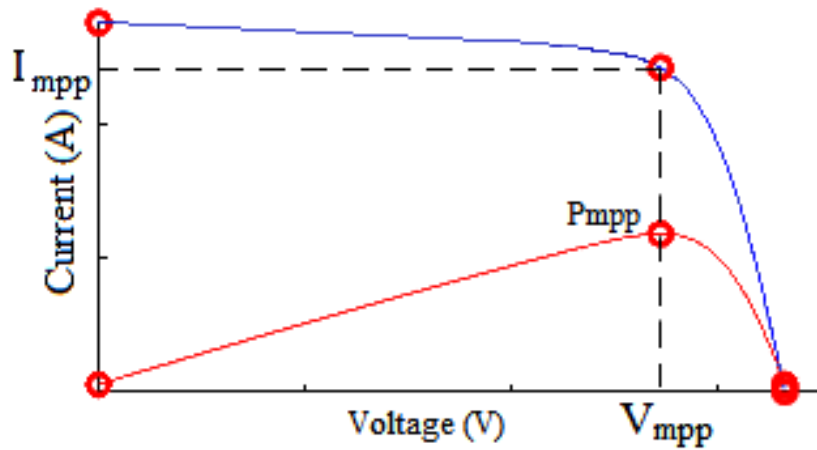
Fig. 2.1 Fractional Open Circuit Voltage

In order to understand the significance of an MPPT in a PV installation, consider the following: The module is directly connected to the load without MPPT is shown in Figure 2.2.a, the output power loss is obvious and the energy is not completely transferred as shown in Figure 2.2.b.
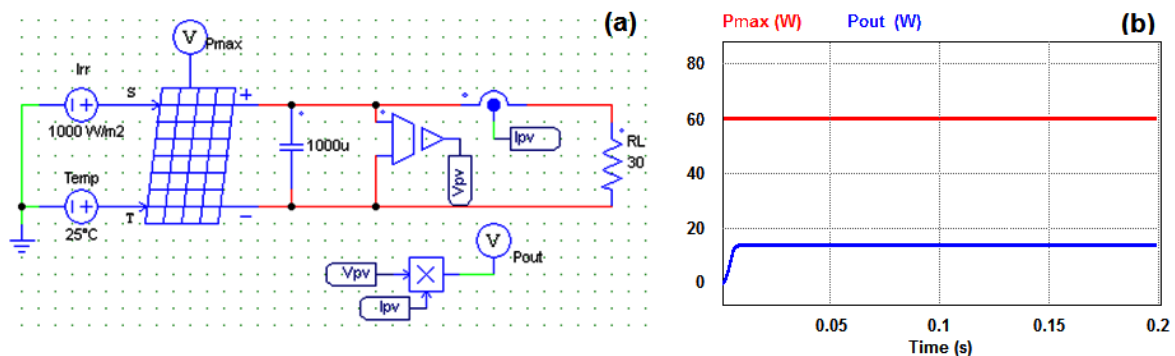
Fig. 2.2 Output Power of PV Array without MPPT in the PSIM environment

There are many MPPT methods available in the literature; MPPT techniques can be classified into three categories [69] (Fig 2.3). The first category is that of indirect methods. These methods, for example short circuit methods (SC) and open circuit methods (OC) [65] require knowledge of the characteristics of the photovoltaic generator. The techniques SC and OC MPPT are based on mathematical equations that cannot manage non-linearity. The direct methods guarantee higher energy conversion efficiency and do not require periodic parameter adjustment, as in the case of fractional techniques. The most used are the Perturb

& Observe (P&O) methods [92, 116, 63] or the incremental techniques (IC) [150, 13, 87]. The third category is soft computing (SC) techniques based on mathematical models due to the availability of high computing power and low cost. It's very sophisticated and has a high convergence speed.
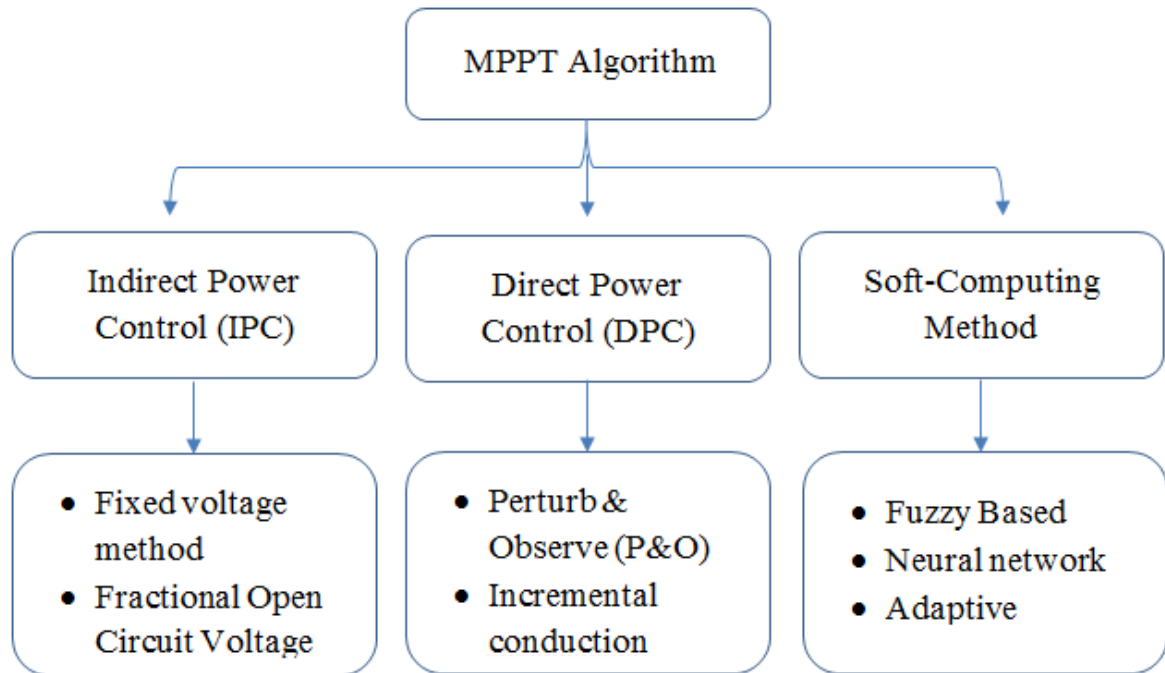
Fig. 2.3 The MPPT algorithm classification

The most used techniques are described in the following sections, choosing a method from each category and starting with the simplest method.

2.2.1   Indirect MPPT methods

These techniques require knowledge of the characteristics of the photovoltaic generator. The techniques SC and OC MPPT are based on mathematical relations which cannot manage non-linearity.

Fixed Voltage method (CV)

The constant voltage (CV) algorithm is the simplest MPPT control method. The operating point of the photovoltaic generator is maintained near the MPP by regulating the generator voltage and by adapting it to a fixed reference voltage V_{ref}. The V_{ref} value is defined equal to the V_{mpp} of the characteristic PV module (see table 2.1).

In this algorithm, V_{mpp} is calculated as:

$$V_{mpp} = k * V_{oc} \tag{2.1}$$

Where k is usually between 0.7 and 0.9. This algorithm is simple, but its accuracy is low,

Table 2.1 PV module (specification (LG 330)

Prameter	Value
Maximum power [W]	325 *w*
MPP Voltage Vmpp [V]	33.7 *V*
MPP Current Impp [A]	9.65 *A*
Open Circuit Voltage Voc [V]	40.9 *A*
Short Circuit Current Isc [A]	10.23 *V*

and determining best value of k is difficult. In Reference [102], The methods of fractional open circuit voltage (Voc) [20] and fractional short-circuit current (Isc) [143] exploit the completely linear relationship between Voc or Isc and the value, respectively, of the voltage or current at the MPP condition. For best results, use both techniques [100]. These techniques do not reach the PPM precisely in any environmental profile. In addition, according to [15], the measurement of temperature and sunshine requires expensive devices. This measure has become more expensive for the entire photovoltaic installation.

2.2.2 Direct MPPT methods

These methods guarantee higher energy conversion efficiency and do not need a periodic adjustment of the parameter, as in the case of fractional techniques. The most used are the Perturb & Observe (P&O) methods [1, 2] or the incremental techniques (IC) [128]. Other solutions have recently been developed to manage partial shading with several local MPPs. They provide a robust global MPP using particle swarm optimization methods (PSO) [110, 145, 71] or procedures to study certain regions of the i-v curve [75, 3].

P&O method

P&O algorithms work by periodically disturbing (i.e. increasing or decreasing) the voltage or current across the network and comparing the PV output power with that of the previous disturbance cycle. If the operating voltage of the PV generator changes and the power increases ($dP/dV > 0$), the control system moves the operating point of the PV generator in

this direction; otherwise, the operating point is moved in the opposite direction. In the next perturbation cycle, the algorithm continues in the same way.

 A common problem in P&O algorithms is that the voltage across the network is disturbed at
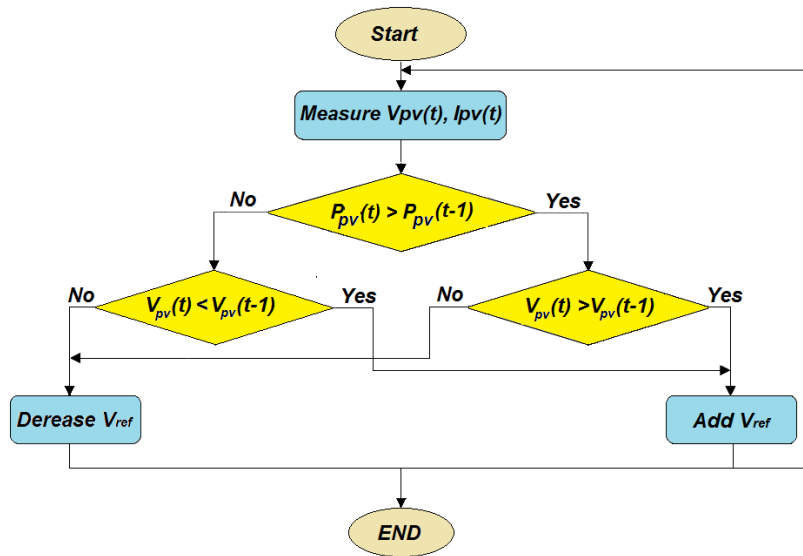
Fig. 2.4 Flowchart of P&O algorithm

each MPPT cycle; therefore, when the MPP is reached, the output power oscillates around the maximum, causing a loss of power in the PV system. This is especially true under constant or slowly varying atmospheric conditions.

2.2.3   Soft computing method

Recently, the soft computing (SC) techniques have been extensively applied to enhance the efficiency of the MPPT [108, 147, 121, 112, 111, 90, 88, 51]. The methods are considered full of promise with higher efficiency and excellent performance under varying environmental conditions. This is due to the availability of high computing power and low cost. SC methods comprise many different algorithms: fuzzy logic control (FLC), artificial neural networks (ANNs), evolutionary computation (including genetic algorithms (GAs), differential evolution (DE), particle swarm optimization (PSO)) [127], ant colony systems (ACSs)), and chaotic search (CS) [77].

ADALINE MPPT

Adaptive Linear Neuron (ADALINE) based on mathematical model of human brain neuron with multi-inputs and single-output. ADALINE updates the weights online by using LMS

(Least Mean Square), RLS (Recursive Least Square) and KF (Kalman Filter) recursive algorithm) [147]. The most ADALINE weights are using an iterative linear LMS algorithm in order to minimize the error e(k) [16], The common structure of an artificial neuron has been depicted in figure 2.5.
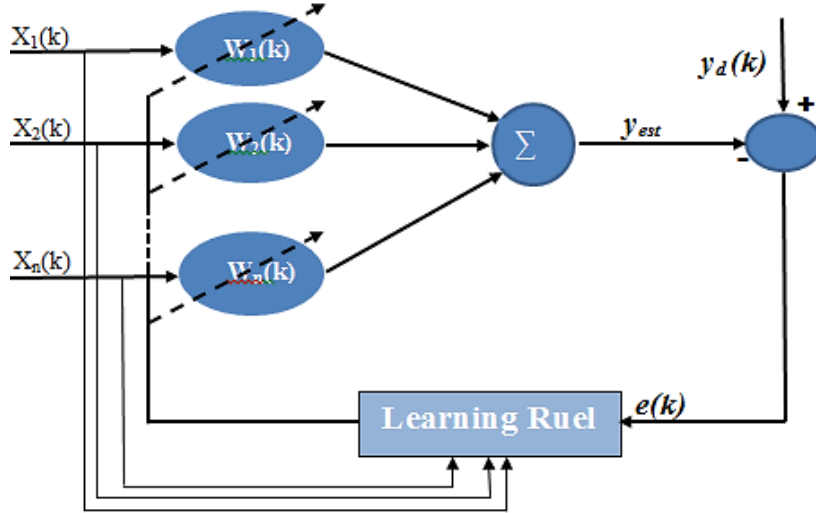
Fig. 2.5 Basic architecture of Adaline neural network.

Where $X = [x_1, x_2, ..., x_{n-1}, x_n]$ represents inputs vector, b is a constant value called bias of neuron, $W = [w_1, w_2, ..., w_{n-1}, w_n]$ is the weighting vector. As well, $P = [x_1 * w_1, x_2 * w_2, ..., x_{n-1} * w_{n-1}, x_n * w_n]$ represents the sum of weighing inputs, f is called activation function and y=f(P) is output of neuron. T is a linear activation function and an estimated output $y_{est}(k)$.

A weight is modified using the following formula [52]:

$$y_k = \sum_{i-1}^{n} x(i)_k w_k = x_i^k w_k \tag{2.2}$$

The most ADALINE weights are updated by using an iterative linear LMS algorithm in order to minimize the error e(k).

$$w_{k+1} = w_k + \mu e_k x_k \tag{2.3}$$

Where μ is the learning parameter. To ensure stability and convergence of the ADALINE algorithm, most practical applications choose μ control as follows:

$$0 < \mu < 2 \tag{2.4}$$

2.3   Proposed topology

The circuit is shown in Fig 2.6 this converter is composed by the Boost converter and Cuk converter [105, 104], The fundamental advantage of this converter is to reduce the number of switches and inductors compared to the isolated converters. Additionally, the voltage stress across the switch is moreover decreased along with the reduction in input current ripple. The voltage polarity at the output of the Cuk is reversed regarding the voltage polarity at the input side. Both converters have the same DC input current, while the Cuk converter, unlike the boost converter, has an inverted voltage gain.
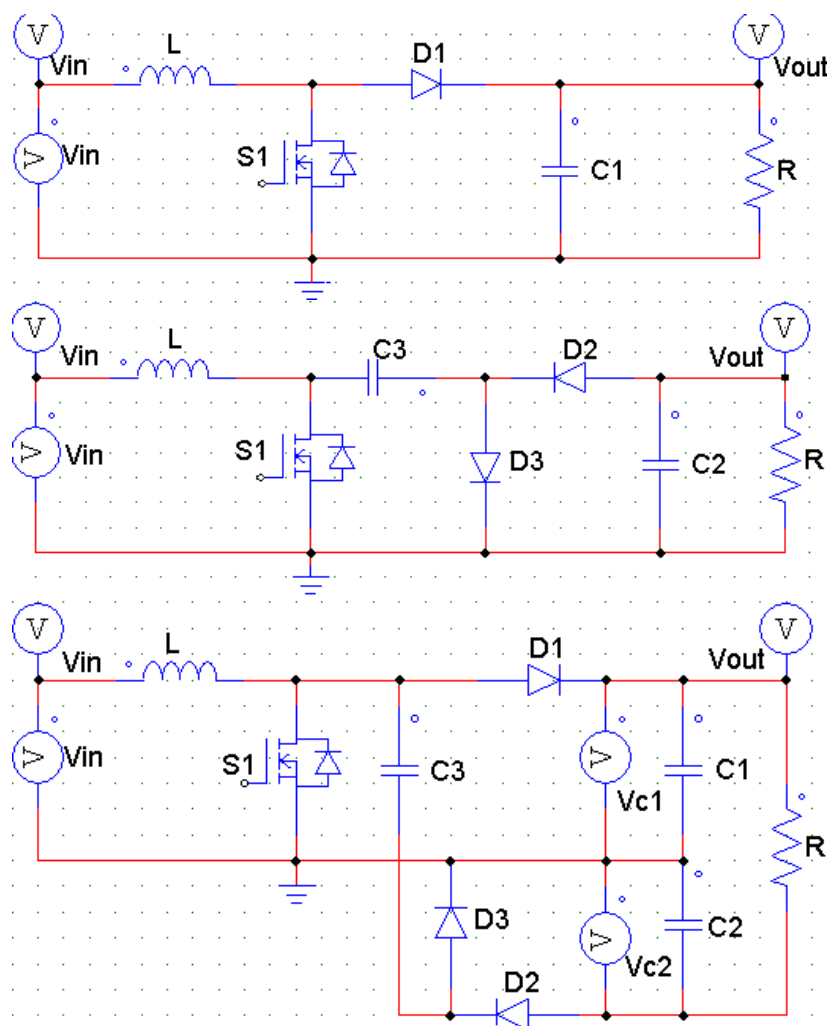
Fig. 2.6 Boost, Cuk, Boost/Cuk

2.3.1   Operating mode

There are two operating modes Fig 2.7:

Mode 1

The power switch S_1 is turned on, the diode D_1 and D_3 are OFF for its inverse biased, therefore, the current in inductor L will increase, C_1 and C_2 are charged in parallel. To avoid the invalid state variables can be taking into consideration the series resistance R of capacitor C_3. According to the circuit theory, the equations for describing this mode can be derived as follows (Fig 2.7a).

$$\begin{cases} L\frac{di_L}{dt} = V_{in} \\ C_1\frac{dv_{c1}}{dt} = -i_R = -\frac{V_{c1}+V_{c2}}{R} \\ C_2\frac{dv_{c2}}{dt} = i_{c3} - i_R = \frac{V_{c3}+V_{c2}}{r} - \frac{V_{c1}+V_{c2}}{R} \\ C_3\frac{dv_{c3}}{dt} = -\frac{V_{c3}-V_{c2}}{R} \end{cases} \tag{2.5}$$

Mode 2

The power Switch S_1 is turned off; the Diode D_1 and D_3 are ON for Its Forward biased Voltage. According to the circuit theory, the equations for describing this mode can also be derived as follows (Fig 2.7b):

$$\begin{cases} L\frac{di_L}{dt} = V_{in} - V_{c1} \\ C_1\frac{dv_{c1}}{dt} = (i_L - i_{c3}) - i_{c2} = i_L - \frac{V_{c1}-V_{c3}}{r} - \frac{V_{c1}+V_{c2}}{R} \\ C_2\frac{dv_{c2}}{dt} = -i_R = -\frac{V_{c1}+V_{c2}}{R} \\ C_3\frac{dv_{c3}}{dt} = \frac{V_{c1}-V_{c3}}{r} \end{cases} \tag{2.6}$$

(a) Boost

(b) Boost/Cuck
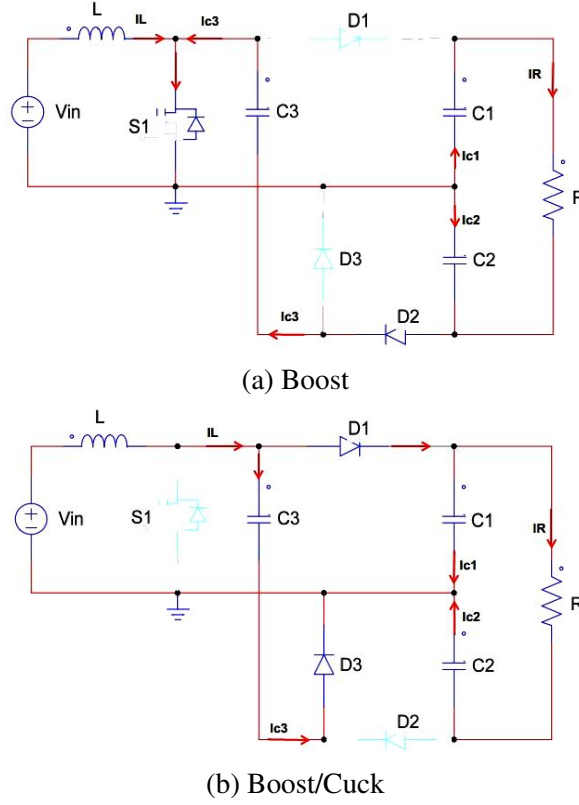
Fig. 2.7 The power flows of the two operation modes

2.3.2   State Space equations

Based on the average method and the eqs: 2.5 and 2.6, the average model of this open-loop step-up converter can be easily obtained as follows (eq 2.5).

$$
\begin{bmatrix} L\frac{d\hat{i}_L}{dt} \\ \frac{d\hat{v}_{c1}}{dt} \\ \frac{d\hat{v}_{c2}}{dt} \\ \frac{d\hat{v}_{c3}}{dt} \end{bmatrix} =
\begin{bmatrix}
0 & -\frac{1-D}{L} & 0 & 0 \\
-\frac{1-D}{C_1} & -\left(\frac{1-D}{C_1 r} + \frac{1}{C_1 R}\right) & -\frac{1}{C_1 R} & -\frac{1-D}{C_1 r} \\
0 & -\frac{1}{C_2 R} & -\left(\frac{1}{C_2 R} + \frac{D}{C_2 r}\right) & -\frac{D}{C_2 r} \\
0 & \frac{1-D}{C_3 r} & \frac{D}{C_3 r} & -\frac{1}{C_3 r}
\end{bmatrix}
\begin{bmatrix} \hat{i}_L \\ \hat{v}_{c1} \\ \hat{v}_{c2} \\ \hat{v}_{c3} \end{bmatrix} +
\begin{bmatrix} \frac{1}{L} \\ 0 \\ 0 \\ 0 \end{bmatrix} * \hat{v}_{in}
$$

$$
+
\begin{bmatrix}
0 & \frac{1}{L} & 0 & 0 \\
-\frac{1}{C_1} & \frac{1}{C_1 r} & 0 & -\frac{1}{C_1 r} \\
0 & 0 & -\frac{1}{C_2 r} & \frac{1}{C_2 r} \\
0 & -\frac{1}{C_3 r} & \frac{1}{C_3 r} & 0
\end{bmatrix}
\begin{bmatrix} i_L \\ V_{c1} \\ V_{c2} \\ V_{c3} \end{bmatrix} \hat{d}
$$

$$
(2.7)
$$

A state space description is a canonical form for writing the differential equations that describe a system. Although the state space averaged model has been derived using ideal components.

2.3.3 Transfer Function of Hybrid Boost-Cuk converter

Transfer function from Duty Ratio (Control) to Output voltage $G_{VD}(s)$ of Hybrid Boost-Cuk converter:

$$G_{VD}(s) = C(sI - A)^{-1}B \tag{2.8}$$

where: $C = \begin{bmatrix} 0 & 1 & 0 & 0 \end{bmatrix}$ and I: identity matrix.

The parameters of Hybrid Boost-Cuk converter are given as follow in table 2.2:

Table 2.2 Design parameters used for simulation [105]

Prameter	Symbol	Value
Input voltage	V_{in}	48 V
Output voltage	$V_{out} = V_{c1}$	220 V
Capacitors	$C_1 = C_2$	1000 μ
Inductor	L	5 mH
Resistor	R	50 Ohm
Switching frequency	f_s	20000 Hz

2.4 Robust Loop shaping design

2.4.1 The loop-shaping technique

Loop shaping is a classical method based on open-loop. The basic idea of loop shaping approach is to specify the performance of a system, before designing the controller. In order to achieve performance and robustness, it is necessary to ensure a high magnitude open-loop gain at low frequencies is required for load disturbance attenuation, and small magnitude open loop gain at high frequencies is advantageous for a good attenuation of measurement noise or unmodeled dynamics perturbations [37, 140]. see figures 2.8 and 2.9.
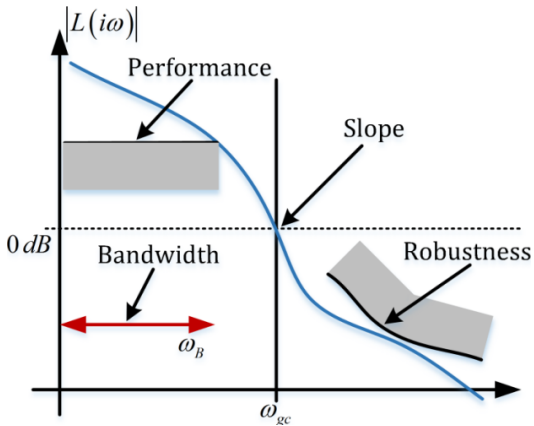
Fig. 2.8 Loop shaping behavior
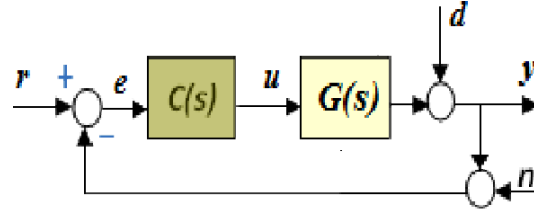
Fig. 2.9 Loop shaping block diagram

where: r : reference signal (to be tracked by the output y) d : external perturbation (referred to the output) n : sensor noise, e :error, y : output signal, u control signal.

$$y = \frac{G(s)C(s)}{1+G(s)C(s)}r + \frac{1}{1+G(s)C(s)}d - \frac{G(s)C(s)}{1+G(s)C(s)}n \qquad (2.9)$$

$$y = \frac{L}{1+L}r + \frac{1}{1+L}d - \frac{L}{1+L}n \qquad (2.10)$$

$$y = Tr + Sd - Tn \qquad (2.11)$$

Where: S : sensitivity, T : complimentary sensitivity.

$$L = G(s)C(s) = G_{0L} \qquad (2.12)$$

Robust tracking and disturbance rejection design is obtained by reducing the transfer function from d to y, which is called sensitivity. Further, the transfer function from n to y can be examined in order to achieve sensor noise rejection.

This is accomplished by choosing a compensator, a lead, a lag, or a Lead-lag that gives a loop transfer function with the desired shape.

If we chose $C(s)$, such as L is much great than one. The closed loop transfer function become:

$$y = r, with \begin{cases} \frac{L}{1+L} \simeq 1 \\ \frac{1}{1+L} \simeq 0 \end{cases} \qquad (2.13)$$

2.4.2 Open loop Transfer Function

From the equation (2.7), the transfer function between duty cycle as the control variable and the voltage across V_{c1} as a controlled variable, and after neglecting the higher order system, it can be approximated by a second-order system:

$$G_{VD}(s) = \frac{-332.66s + 5914}{s^2 + 2,098s + 13.38} \tag{2.14}$$

2.4.3 Controller Design

The controller will be obtained using a frequency loop shaping technique and closed-loop specifications that follow.

Closed-loop specifications:

- Track a reference with finite steady-state error $ed < 0.2$.

- Rise-time of unit step response $\hat{s} < 20\%$.

In the loop shaping synthesis, the $C(s)$ controller is designed in a series of steps, the first step is to determine a static performance $C_1(s)$, and the second step is dynamic performance specifications.

The form of the static performance controller is: $C_1(s) = \frac{K_c}{s}$. where K_c is the controller gain. To ensure steady state error is less than 0.02,

$$\lim_{x \to +\infty} e(t) = \lim_{s \to 0} SE(s) = \lim_{s \to 0} S(R(s) - C_1 G(s)) = \frac{1}{1 + K_c G(0)} < 0.2 \tag{2.15}$$

So, $K_c < 0.012$, finally, can be choose $K_c = 0.01$. Let's examine the current open loop gain $L_1(s) = C_1 G(s)$ for $s = jw_c$. where: w_c the desired crossover frequency. If we assume controller closed-loop responses for dynamic performance is similar to 2nd-order under damped systems [40]:

$$C_2(s) = \frac{1}{1 + \frac{2\zeta}{w_n}s + \frac{1}{w_n^2}s^2} \tag{2.16}$$

A bandwidth of closed-loop system is the range of frequencies at $-3dB$:

$$B_3 \simeq \frac{3}{t_r} \tag{2.17}$$

Where t_r: time rise.
From of step response (G_{vd}) 2.14: $t_r = 0.06s$, $B_3 = 50\,rad/s$.

Or: $w_c \simeq [0.5, 0.8]B_3 = 32\,rad/s$.

The percentage overshoot (PO) is:$\hat{s} \simeq 0.85M_r - 1$ and $M_p \simeq \frac{2.3 - M_r}{1.25}$, so $M_p \simeq = 0.71\,rad = 40\,deg$. (where M_p is peak overshoot)

- $\|32.5j\| = -48\,dB$

- $\angle(32.5j) = -32\,deg$

At $w_c = 32.5\,rad/s$ needs to increase the gain by $\Delta M = 0 + 48 = 48\,dB$, and the phase by $\Delta\phi = (180 - 40) - 32 = 108\,deg$. From the figure 2.10, a suitable compensator for dynamic
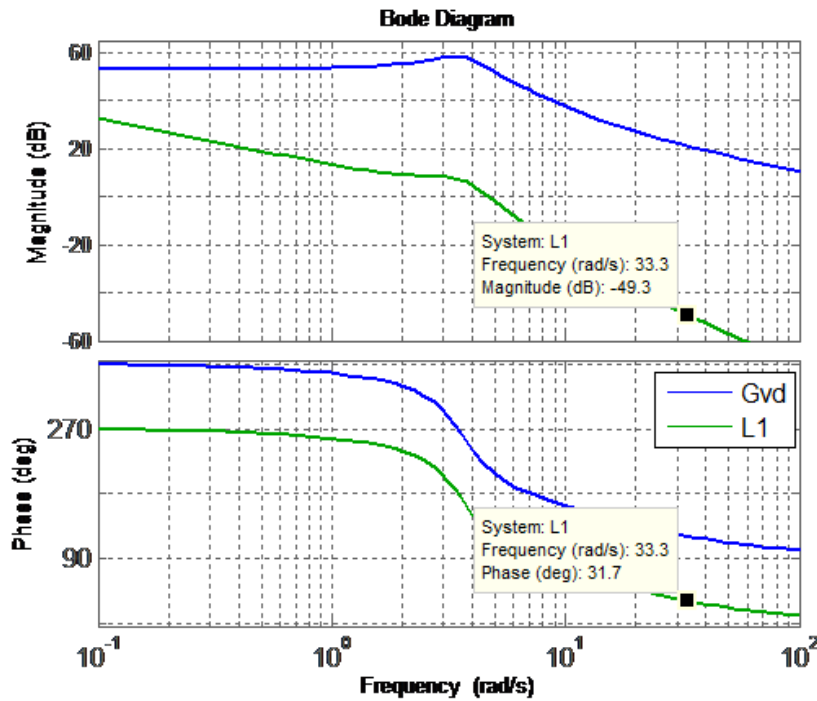
Fig. 2.10 Open loop voltage transfer function (G_{vd}, L_1)

performance to accomplish this is a lead compensator, which has the form:

From the figure 2.11, a suitable compensator for dynamic performance to accomplish this is a lead compensator, which has the form:

$$C_2(s) = \frac{1 + \alpha\tau s}{1 + \tau s} \quad \tau > 0, \quad 0 < \alpha < 0 \tag{2.18}$$
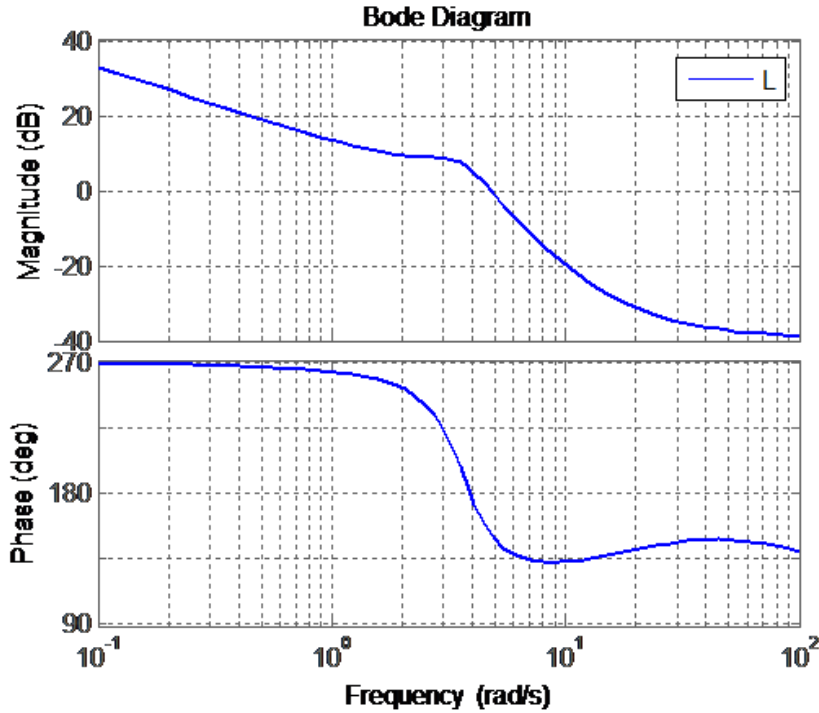
Fig. 2.11 Bode plot of hybrid Boost-Cuk converter feedback controlled

if we set $\alpha = 0.05$ and $w_c = \frac{1}{\tau\sqrt{\alpha}}$, so $\tau = 0.05\,s$.
The final controller will be:

$$C(s) = C_1(s)C_2^2(s) \tag{2.19}$$

2.5 Simulation Results

The DC/DC converter fed by a photovoltaic generator with energy storage is represented in figure 2.12, the overall proposed design has been numerically simulated by using the environment of Power-Sim on the basis of the parameters indicated in Table 2.2. A string of 4 PV modules ($LG330A$) connected in 02 series/ 02 parallel has been adopted as PV source. The maximum power generated by the PV generator is $P_{max} = 1200\,w$. The main characteristics of the PV generation system are summarized in Table 2.3.

2.5.1 Simulation with Battery

The first proposed conversion of the PV system with battery. Under natural conditions, the temperature fixed specifically at $25C$, MPPT control of Pv with P&O method control is
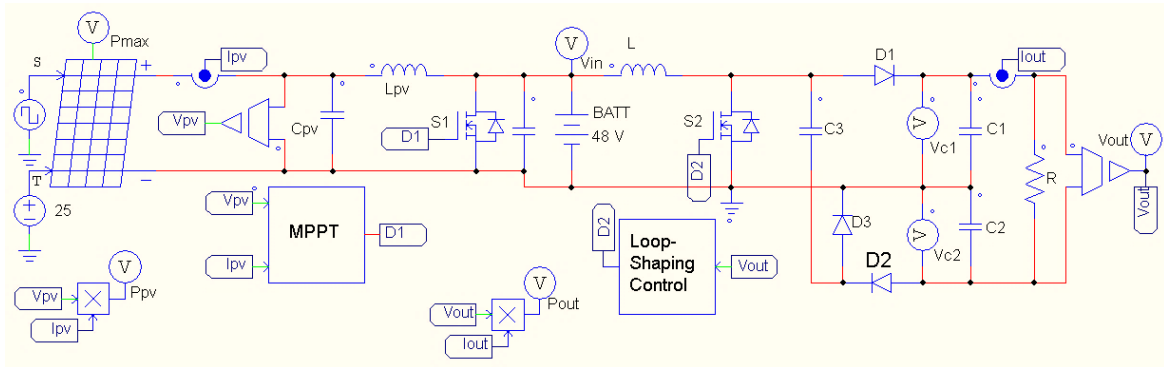
Fig. 2.12 PSIM schematic of proposed conversion structure and the mid-point boost

Table 2.3 GPV Specifications

Photovoltaic Panel LG Neon2 330w	
Prameter	Value
MPP Voltage (V_{mpp})	34.1 V
MPP Current (I_{mpp})	9.69 A
Solar panels in series	2
Solar panels in parallel	2
Power delivered (P)	1300 W

shown in fig 2.13, To verify the possible impact when solar irradiance changes linearly, with amplitude range between 1000 to 600 W/m^2, the MPPT controller respond quickly under step change of solar irradiance. (Fig 2.13.a)

It can be seen in figure 2.13.(b) the performance of the MPPT controller, the whole maximum power ($P_{max} = 1200\,w$) is supplied to the load (P_{out}), despite variations in solar radiation input power is almost the same. The voltage across the PV array after a rapid change of irradiance does not change as shown in fig 2.13.c. On the other hand the current changes according to the solar irradiation (Fig 2.13.d).

It is important to note here that the power extracted from the GPV is almost completely delivered at the output of the dc/dc converter thanks to the important role of the MPPT controller, on the other hand, no change in the output power, even though the change in solar irradiance (Fig 2.14.a), this is due to the fact that the missed of power is compensated by the battery (Fig 2.14.b).

In the steady-state operation mode illustrated in (fig 2.14.c) its well shown a response of the output voltage V_{cl} and V_{c2}. Note that the two tensions follow the reference voltage after a certain undulation. The application of Loop Shaping controller ensures robustness against
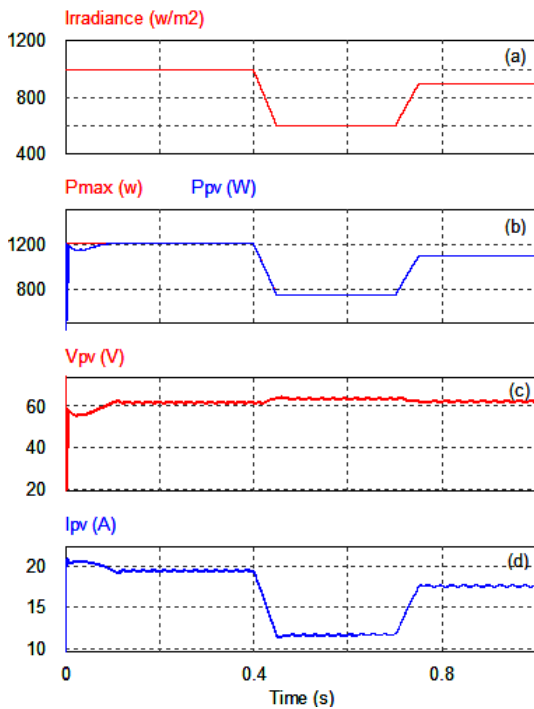
Fig. 2.13 GPV output power,
voltage, current
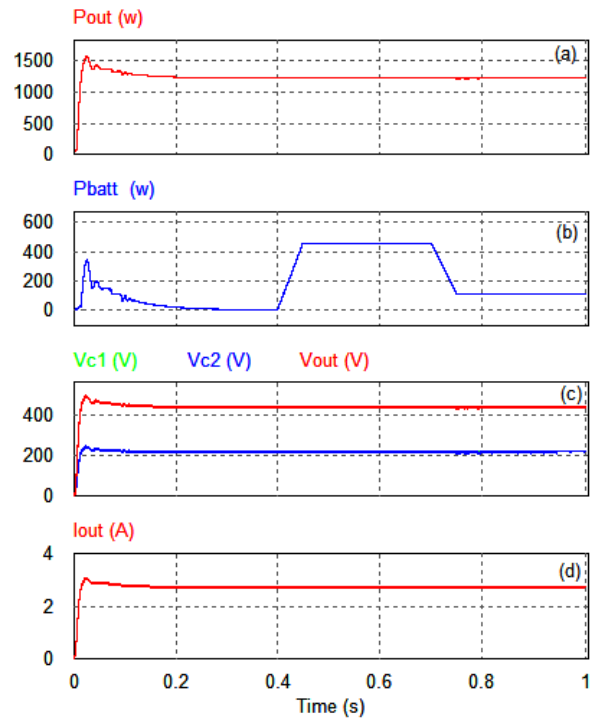
Fig. 2.14 Power, output voltage
of the boost converter

model uncertainties and unmeasured disruptions, providing a systematic framework. Figure 2.14.*d* shows the current delivered to the load. The current does not change due to the energy stored by battery.

2.5.2 Simulation without Battery

The second proposed conversion of the battery-less PV system which is used Psim schematic with MPPT for simulations is illustrated in figure 2.15.

In order to evaluate the conversion of the structure of the PV system without battery and the performance of the MPPT algorithm, a simulation test in which the PV panel is exposed to a variation in irradiance as shown in figure 2.16.*a*.

The GPV output power (P_{pv}) and the dc/dc converter output power (P_{out}) shown in figure 2.16.*b*. The P_{out} (Fig. 2.17.*b*) is slightly less than the power P_{pv} due to power losses in the power semiconductors switches (transistor, diodes, ...) and passive components (resistor, inductor...).

The voltage V_{pv} slightly varies according to the variations of the solar irradiations fig 2.16.*c*,
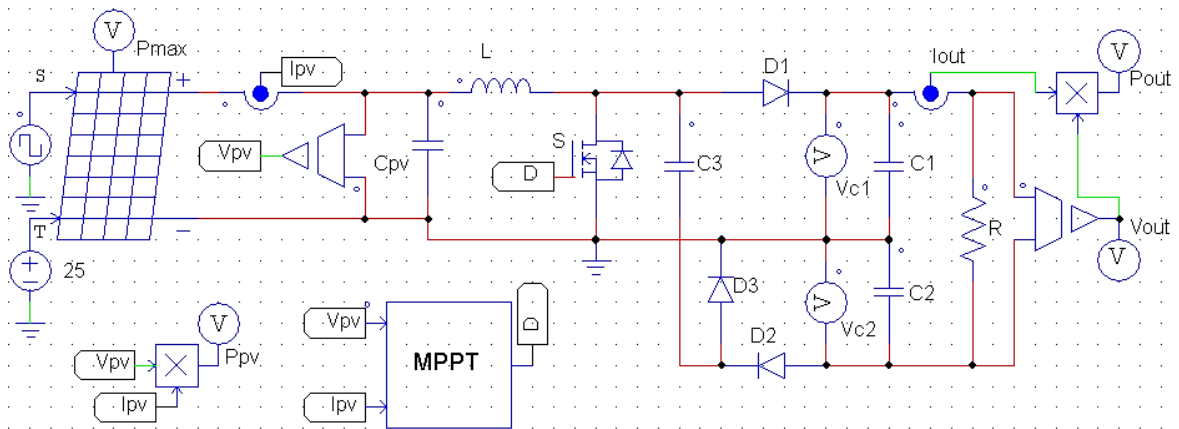
Fig. 2.15 PSIM schematic of DC/DC boost converter without battery

whilst the output current of the GPV varies linearly with the variations of the solar irradiations fig 2.16.*d*.
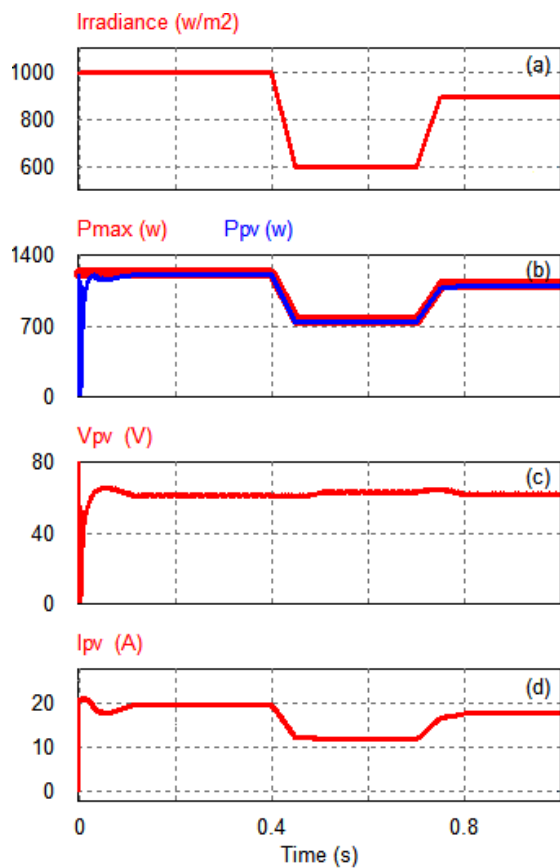
Fig. 2.16 GPV output power, voltage, current without battery
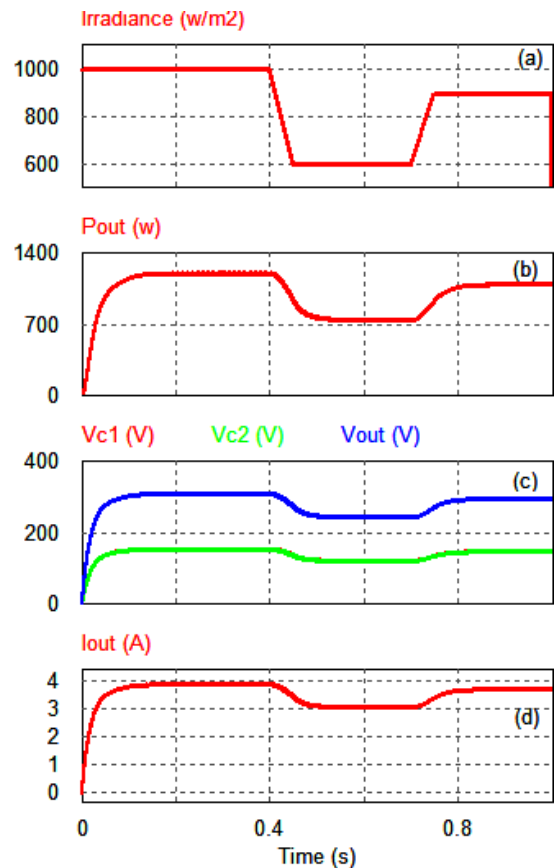
Fig. 2.17 Power, output voltage of the boost converter without battery

Looking at figure 2.16 and table 2.3, it can be seen that the controller adapts the PV panel output in order to obtain the maximum power for any irradiance level. It appears that the controller has a very fast response.

2.6   Conclusion

In this chapter, the different components of a DC / DC conversion system for photovoltaic energy conversion system have been presented. The first section presented the different types of MPPT algorithms. The second section introduced the mathematical model of a DC/DC boost converter (boost/cuk). The system transfer function is used to optimally select the parameters of the DC/DC step-up converter. Loop shaping involves specifying the performance of a system at the beging before the controller is designed to achieve performance and robustness. It has been accomplished by ensuring high amplitude at low frequencies which is required for load disturbance attenuation and gain open loop low amplitude at high frequencies, this method was easy to implement and gave desired results using the Power-sim enviroment.

Chapter 3

On Cascaded loop shaping/hybrid mode control design of three cell inverter

Chapter 3

On Cascaded loop shaping/hybrid mode control design of three cell inverter

3.1   Itroduction

Dynamical Hybrid Systems represent a multidisciplinary area which has been developed over the past decade and extends between the limits of computer science, control theory and mathematics. A hybrid system is capable of representing complex physical systems with discrete and continuous sub-systems that interact with each other [24, 17, 7].

Switching circuits in power electronics dedicated to energy conversion are considered as a good example of dynamical hybrid systems, because they are intrinsically hybrid in their nature indeed, power switching devices have discrete inputs, continuous outputs, and disturbances that are either continuous, such as parametric variation in a load, or discrete, as in a fault state of a particular switch [57, 91, 5].

Among these switching systems, flying capacitor multi cellular inverters designed on series association of elementary commutation cells are well studied for applications in renewable energy conversion or generation. Multi cellular converters have emerged in the early 90s and became one of the most widely used topologies because of their high input voltage range, thus, they can be used in large size solar fields [80, 74] . Indeed, they offer the possibility of obtaining a very high energy efficiency over a very wide range of power by allowing the variation of the number of operational cells. This is an indisputable advantage for conversion applications in renewable energy systems. This advantage is counter balanced by the control difficulty due to the significant increase in the number of variables to be controlled.The coupling between cells adds to this complexity.

The modeling of multi cellular inverters is generally difficult. Indeed, it contains continuous

variables (voltages and currents) and discrete variables (switches, or a discrete location). In the literature, models have been developed to describe the harmonic, averaging, and instantaneous, behaviors of the multi cellular inverter. The average model [109] consists of calculating the average value of all variables during one sampling period; nevertheless, this model cannot represent the natural balancing of floating voltage.

The harmonic model [41] consists of calculating the harmonic voltage phases and their magnitudes by considering the load current in steady-state operation. The instantaneous model [124] deals with time-evolution of all variables including the discrete location of the switch states. Usage of this model is delicate because the design of controllers is difficult since the inverter exhibits a mixture of continuous and discrete dynamics.

Besides, the control objective for multicell inverters is to design the binary control switches such that the load current (i_L) tracks the desired reference current (i_{ref}), while imposing to the capacitors voltages (v_{c_1}) balanced references. The control of multi cellular inverters has been the subject of extensive research during the last decades (see [129, 113, 73] and references therein). The classical control algorithm employed in open-loop is a PWM (Pulse Width Modulation) control [85, 16], the natural balancing of the voltage of the capacitors is carried out naturally provided that the current source has a finite impedance load [131, 144, 93].

But the dynamics of this natural balancing are quite slow. Conventional *PI* controllers for Stacked multi cellular inverter have been proposed [62] with space vector modulation (SVM) control for regulating the floating voltages. Input/output decoupling via feedback linearizing control has been investigated and reported [48, 148]. This method allows by an algebraic transformation to decouple the dynamics of each state variable with respect to each other, but this method exhibits a singularity and the saturation of commands in the vicinity of a zero charge current. In the work reported in [125], the sliding mode is proposed for control of the inverter. Further, the sliding mode observer is studied [19, 84, 70] to estimate the floating voltages. The obtained controller ensures robust performances in the presence of load parametric variations. The authors of [50, 9] use the model predictive control (MPC) for multi cellular converters. This approach is based on a state predictor and may lead to poor performances. In [18] a purely hybrid control approach is proposed based on the inverter instantaneous model. The developed control exhibits better performances, however the resulting algorithm is complex and time consuming.

In this chapter, a cascaded hybrid robust control of three cell inverter is suggested. The hybrid nature of this inverter, represented by the presence of continuous and discrete dynamics, is taken into account in both the modeling and control design parts. First, the three cell instantaneous model is derived and the control problem is formulated as two cascaded current/voltages loops. Then, the hybrid model of the inverter is discussed in detail. Secondly,

the adjacency constraint for the transition between modes is studied and a new algebraic condition is developed in order to fulfill this constraint. Thirdly, the current loop is rearranged as a robust control problem by taking into consideration the parametric variations of the load and the discretization error between the required continuous voltage and the discrete voltage level generated by the inverter. The loop shaping method is used in order to ensure robust stabilization of the load current to its desired value. The latter method is a frequency domain robust control design method that requires to translate the system's performance into constraints on the open loop's transfer function before calculating the controller.

Finally, a new control algorithm is proposed, based on the hybrid model, to guarantee balanced distribution of the flying capacitors' voltages. The robustness of the proposed control design approach is discussed and simulations are performed through realistic environment. The chapter is organized as follows. Section 2 gives the nonlinear state space model of the three cell inverter and formulates the control objectives. Section 3 presents the hybrid model with eight operating modes and discusses the adjacency constraint. Section 4 is devoted to the design of the loop-shaping controller and the development of the new control algorithm. Section 5 gives simulation results and robustness tests. Some remarks are summarized at the end the chapter.

3.2   Inverter Model and Problem Formulation

Instantaneous model

Each of the inverter's cells contains two complementary power electronics components and is controlled by a binary switch S_k, The signal S_k is equal to 1 when the upper switch of the cell is conducting and 0 when the lower complementary switch of the cell is conducting. These cells are associated in series with R, L load and separated by capacitors that can be considered as continuous sources to these cells (Fig.3.1). The inverter has two floating voltage sources v_{c_1} and v_{c_2}. In order to ensure a normal functioning, it is necessary to guaranty a regulated distribution of these voltages to their equilibrium values that are equal to $\frac{E}{3}$ and $\frac{2E}{3}$ respectively.

Applying Kirchhoff's laws, the three cells inverter is described by the following set of differential equations:
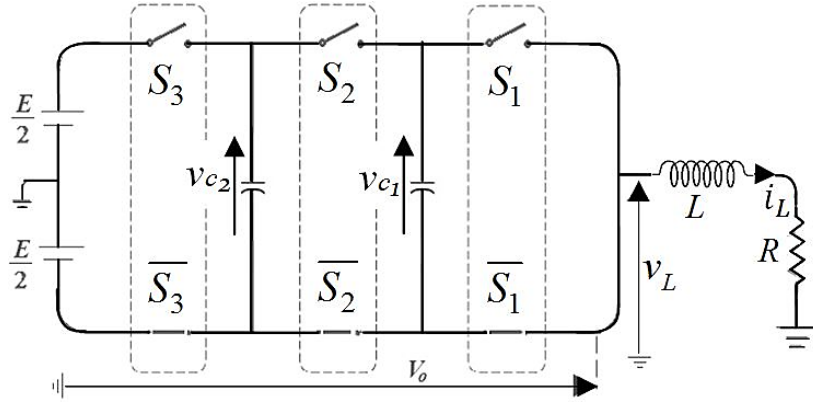
Fig. 3.1 Three–multicell inverter

$$
\begin{cases}
\frac{dv_{c_1}}{dt} = \frac{S_2 - S_1}{C_1} i_L \\[2mm]
\frac{dv_{c_2}}{dt} = \frac{S_3 - S_2}{C_2} i_L \\[2mm]
\frac{di_L}{dt} = -\frac{S_2 - S_1}{L} v_{c_1} - \frac{S_3 - S_2}{L} v_{c_2} - \frac{R}{L} i_L + \frac{E}{L}\left(S_3 - \frac{1}{2}\right)
\end{cases}
\tag{3.1}
$$

This model combines continuous variables (the current i_L and the voltages v_{c_1} and v_{c_2}) and discrete variables (the switches S_1, S_2 and S_3). System 3.1 gives the exact evolution of the inverter. The continuous states vector is $x = [x_1, x_2, x_3]^t$, where x_1 and x_2 represent the floating voltages v_{c_1} and v_{c_2}, x_3 represent the load current i_L. The control signals are the binary inputs S_k.

3.2.1   Control problem formulation

The control objectives are to design the binary control signals S_k such that:

1. Ensuring robust regulation of the load current to the desired current i_{ref}. In fact, the load parameters change in practice and the delivered voltage at the inverter output (V_o) has discrete levels while the load needs continuous input voltages (v_L). This leads to discretization errors that act as input perturbation.

2. Ensuring a good convergence of the voltages across the flying capacitors to their desired reference values given by $\frac{E}{3}$ and $\frac{2E}{3}$ respectively. This guaranties the balancing of voltages (v_{c_1}) and allows to limit the voltage constraints experienced by the power switches.
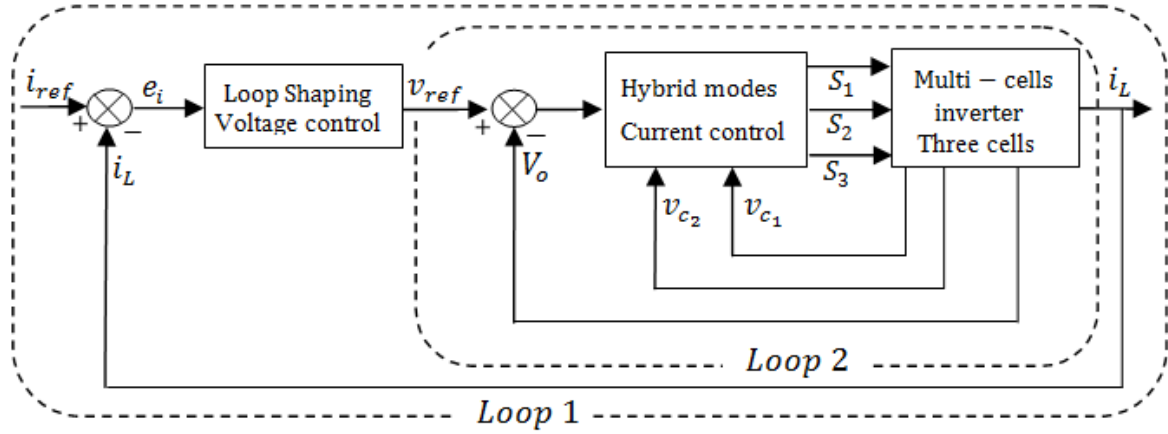
Fig. 3.2 Control loop design Strategy

In order to solve the first control problem (loop 1); the last equation of system (3.1) is rewritten as follows:

$$\frac{di_L}{dt} = -\frac{R}{L}i_L + \frac{v_L}{L} \tag{3.2}$$

where:

$$v_L = (S_1 - S_2)v_{c_1} + (S_2 - S_3)v_{c_2} + E(S_3 - \frac{1}{2}) \tag{3.3}$$

The transfer function from voltage v_L to the output current i_L is:

$$G(S) = \frac{i_L(S)}{v_L(S)} = \frac{1/L}{S + \frac{R}{L}} \tag{3.4}$$

The obtained transfer function will be used to design a robust current controller by loop shaping methodology.

The voltage regulation of the flying capacitors (the second control problem or loop 2) is handled using a new algorithm based on the hybrid model of the inverter. This algorithm defines the suitable switching inputs (S_k) at time intervals (t_k), that ensure the required load voltage while regulating the voltages v_{c_i}. The overall proposed control strategy is a cascaded control as shown in figure 3.2.

3.3 Hybrid Modeling and adjacency rule

3.3.1 Three-Cell inverter Hybrid Model

The instantaneous model of the three cell inverter developed above involves interacting discrete-event (the switches states), and continuous variable dynamics described by continuous differential equations. The hybrid model is completely described as follows:

Depending on the values of the discrete signals S_1, S_2 and S_3, eight configurations or modes are possible $Q = \{q_0, q_1, q_2, q_3, q_4, q_5, q_6, q_7\}$.

The output voltage V_o possesses 4 voltage levels: $-\frac{E}{2}$, $-\frac{E}{6}$, $\frac{E}{6}$ and $\frac{E}{2}$ (see Fig 3.3).

Modes	Switches			$V_o(V)$	Levels (α_i)
	S_3	S_2	S_1		
q_0	0	0	0	$-E/2$	-2
q_1	0	0	1		
q_2	0	1	0	$-\frac{E}{6}$	-1
q_4	1	0	0		
q_3	0	1	1		
q_5	1	0	1	$+\frac{E}{6}$	$+1$
q_6	1	1	0		
q_7	1	1	1	$+E/2$	$+2$

Table 3.1 Switching states and the output voltage levels
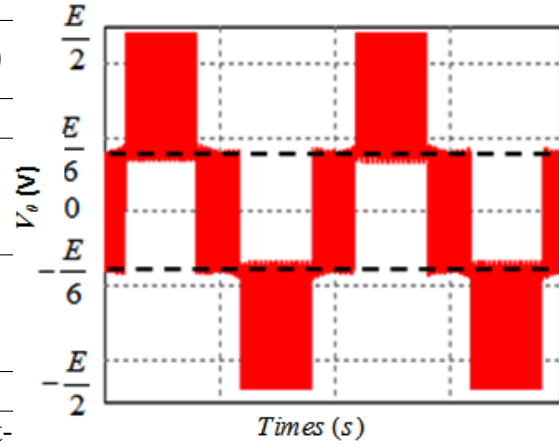
Fig. 3.3 Output voltage levels (V_o)

Each mode is defined in the space of $x_{q_i} = R^3$, $\forall q \subset Q$. The continuous dynamics can be given for each mode in the following form:

$$\frac{dx_i}{dt} = f_{q_i} = A_{q_i} X_{q_i} + B_{q_i} \tag{3.5}$$

- Mode $q = q_0$ ($S_3 = 0, S_2 = 0, S_1 = 0$) (Fig 3.4.a): The continuous variables dynamic equations are given by:

$$f_{q_0} = \begin{pmatrix} 0 & 0 & 0 \\ 0 & 0 & 0 \\ 0 & 0 & -\frac{R}{L} \end{pmatrix} X + \begin{pmatrix} 0 \\ 0 \\ -\frac{E}{2L} \end{pmatrix} \tag{3.6}$$
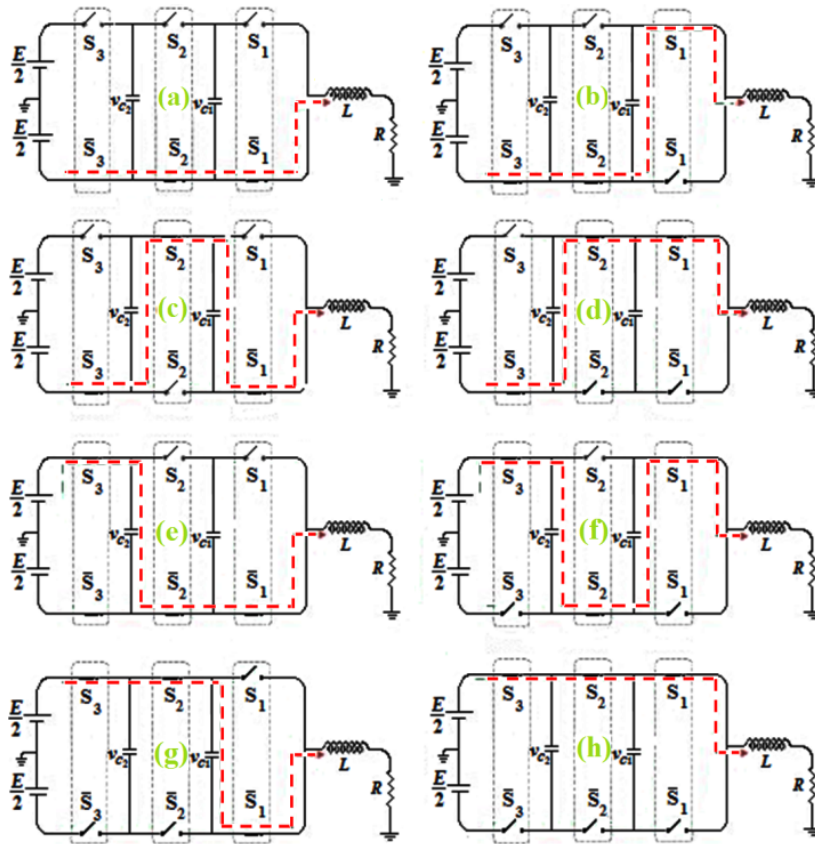
Fig. 3.4 Thrre cells inverter Hybrid Modes

In this mode, the voltage of the floating capacitor does not evolve but the charging current decreases exponentially. The output voltage is: $V_o = -\frac{E}{2}$.

- Mode $q = q_1$ ($S_3 = 0, S_2 = 0, S_1 = 1$) (Fig 3.4.b): The continuous variables dynamic equations are given by:

$$f_{q_1} = \begin{pmatrix} 0 & 0 & -\frac{1}{C_1} \\ 0 & 0 & 0 \\ \frac{1}{L} & 0 & -\frac{R}{L} \end{pmatrix} X + \begin{pmatrix} 0 \\ 0 \\ -\frac{E}{2L} \end{pmatrix} \tag{3.7}$$

In this mode, the capacitor C_1 is discharged and its energy is returned directly toward the load when the charging current is positive ($i_L > 0$). It is charged when the charging current is negative ($i_L < 0$). The output voltage is: $V_o = -\frac{E}{6}$.

- Mode $q = q_2$ $(S_3 = 0, S_2 = 1, S_1 = 0)$ (Fig 3.4.c): The continuous variables dynamic equations are given by:

$$f_{q_2} = \begin{pmatrix} 0 & 0 & \frac{1}{C_1} \\ 0 & 0 & -\frac{1}{C_2} \\ -\frac{1}{L} & \frac{1}{L} & -\frac{R}{L} \end{pmatrix} X + \begin{pmatrix} 0 \\ 0 \\ -\frac{E}{2L} \end{pmatrix} \tag{3.8}$$

In this mode, the capacitor C_1 is charged through C_2. The voltage v_{C_1} increases and the voltage v_{C_2} decreases when the charging current is $(i_L > 0)$. The inverse occurs when the charging current is negative $(i_L < 0)$. The output voltage is: $V_o = -\frac{E}{6}$.

- Mode $q = q_3$ $(S_3 = 0, S_2 = 1, S_1 = 1)$ (Fig 3.4.d): The continuous variables dynamic equations are given by:

$$f_{q_3} = \begin{pmatrix} 0 & 0 & 0 \\ 0 & 0 & -\frac{1}{C_2} \\ 0 & \frac{1}{L} & -\frac{R}{L} \end{pmatrix} X + \begin{pmatrix} 0 \\ 0 \\ -\frac{E}{2L} \end{pmatrix} \tag{3.9}$$

In this mode, the capacitor C_2 is discharged and its energy is returned directly toward the load when the load current is positive $(i_L > 0)$, it is charged when the charging current is negative $(i_L < 0)$. The output voltage is: $V_o = +\frac{E}{6}$.

- Mode $q = q_4$ $(S_3 = 1, S_2 = 0, S_1 = 0)$ (Fig 3.4.e): The continuous variables dynamic equations are given by:

$$f_{q_4} = \begin{pmatrix} 0 & 0 & 0 \\ 0 & 0 & \frac{1}{C_2} \\ 0 & -\frac{1}{L} & -\frac{R}{L} \end{pmatrix} X + \begin{pmatrix} 0 \\ 0 \\ \frac{E}{2L} \end{pmatrix} \tag{3.10}$$

In this mode, the capacitor C_2 is charged through the energy source E and the voltage v_{C_2} increases when the load current is positive $(i_L > 0)$, and vice versa when the charging current is negative $(i_L < 0)$. The output voltage is: $V_o = -\frac{E}{6}$.

- Mode $q = q_5$ ($S_3 = 1, S_2 = 0, S_1 = 1$) (Fig 3.4.f): The continuous variables dynamic equations are given by:

$$f_{q_5} = \begin{pmatrix} 0 & 0 & -\frac{1}{C_1} \\ 0 & 0 & \frac{1}{C_2} \\ \frac{1}{L} & -\frac{1}{L} & -\frac{R}{L} \end{pmatrix} X + \begin{pmatrix} 0 \\ 0 \\ \frac{E}{2L} \end{pmatrix} \qquad (3.11)$$

In this mode, the capacitor C_2 is charging through the energy source $E/2$ and the capacitor C_1 is discharged when the charging current is positive ($i_L > 0$). The inverse occurs when the charging current is negative ($i_L < 0$). The output voltage is: $V_o = +\frac{E}{6}$.

- Mode $q = q_6$ ($S_3 = 1, S_2 = 1, S_1 = 0$) (Fig 3.4.g): The continuous variables dynamic equations are given by:

$$f_{q_6} = \begin{pmatrix} 0 & 0 & \frac{1}{C_1} \\ 0 & 0 & 0 \\ -\frac{1}{L} & 0 & -\frac{R}{L} \end{pmatrix} X + \begin{pmatrix} 0 \\ 0 \\ \frac{E}{2L} \end{pmatrix} \qquad (3.12)$$

In this mode, the capacitor C_1 is charged through the energy source E and the voltage v_{C_1} increases when the load current is positive ($i_L > 0$), the inverse occurs when the charging current is negative ($i_L < 0$).The output voltage is: $V_o = +\frac{E}{6}$.

- Mode $q = q_7$ ($S_3 = 1, S_2 = 1, S_1 = 1$) (Fig 3.4.h): The continuous variables dynamic equations are given by:

$$f_{q_7} = \begin{pmatrix} 0 & 0 & 0 \\ 0 & 0 & 0 \\ 0 & 0 & -\frac{R}{L} \end{pmatrix} X + \begin{pmatrix} 0 \\ 0 \\ \frac{E}{2L} \end{pmatrix} \qquad (3.13)$$

In this case, energy is provided by the source of voltage $E/2$. The charging current increases and the voltage with the terminal of the capacitor remain unchanged.The output voltage is: $V_o = +\frac{E}{2}$.

3.3.2 Adjacency constraint

Transition between modes is possible. However, from a practical point of view there are some restrictions that reduce the number of admissible switches, to minimize energy loss.

The adjacency rule means that transition from one voltage level to another must be achieved by at most a unique change in the binary switches S_k. This allows minimum switching losses while achieving current tracking during operation. Taking into account the above constraint there exist 4 possible transitions from the q_i operating mode to q_j. In the sequel a new mathematical condition is proposed to achieve this rule.

Consider a sequence of time intervals $(t_0, t_1, t_2, \ldots, t_n)$ and let $(q_0, q_1, q_2, \ldots, q_n)$ the corresponding modes (Fig. 3.5). A mode q_i is written as $q_i = \begin{pmatrix} S_1^i \\ S_2^i \\ S_3^i \end{pmatrix}$, where S_j^i is the value
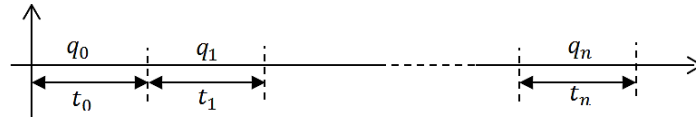
Fig. 3.5 Times with modes corresponding

(state) of the S_i switch at the time interval t_i. We have the following result:

Theorem 1: *Consider the three cell inverter operating during the time intervals $(t_0, t_1, t_2, \ldots, t_n)$. Then the adjacency constraint is satisfied if and only if:*

$$\sum_{k=1}^{3} \left(S_k^{i-l} - S_k^i \right)^2 = 1 \qquad i = 1, \ldots, n \qquad (3.14)$$

Proof:
$\Delta_k = (S_k^{i-1} - S_k^i)$ represents the change made on the switch between time intervals t_{j-1} and t_j. The possible values of Δ_k are 0, -1, 1. If there is no change in S_k then $\Delta_k = 0$. If S_k changes then $(\Delta_k)^2 = 1$. The adjacency constraint imposes at most, one transition between two time intervals t_{j-1} and t_j That is $\sum_{k=1}^{3} (\Delta_k)^2 = 1$.
End Proof:

Notice that the above result can be generalized to multicellular inverters with p cells. For the three cells inverters the admissible transitions in agreement to theorem 1 are given in the following automata:

Figure 3.6 shows the hybrid automaton of a three-cell inverter. The dynamics of each mode are indicated within each circle and the transitions allowed from one level to another level are indicated by arrows. Other transitions (example:$G(q_1, q_2)$) are not allowed because they do not respect the adjacency rule.

The established transitions are given in order to ensure an adjustment of the floating voltage v_{c_1} and the load current i_L around the reference values.
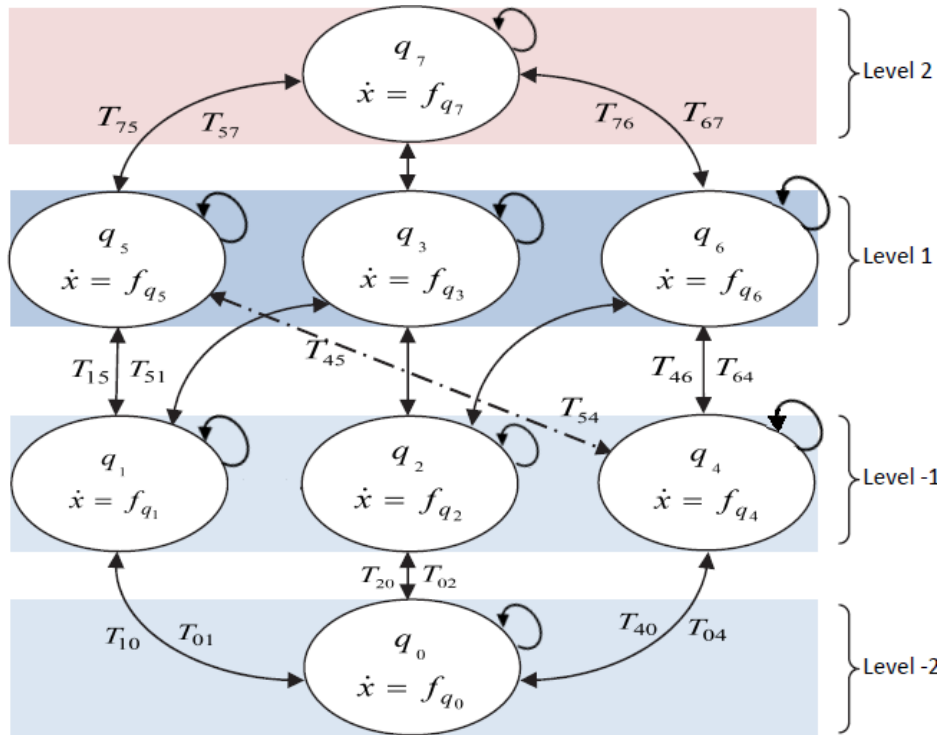
Fig. 3.6 Transition system for three-cell inverter

3.4   The Proposed Loop Shaping Hybrid Modes Control Strategy

This section defines the control scheme for the three cell inverter. The proposed control scheme is based on two stage cascaded loops, as shown in Figure 3.2. The first loop implements the output current control, assigning the voltage V_L that the load must receive in order to regulate the output current error $e_i = i_{ref} - i_L$. This loop is designed using loop shaping methodology. The second loop generates the required voltage level for loop 1 and ensures the regulation of the voltage errors $e_{v_1} = e_{v_{c_{1ref}}} - e_{v_{c_1}}$ and $e_{v_2} = e_{v_{c_{2ref}}} - e_{v_{c_2}}$. The voltage loop receives the voltage level reference from the current controller and the charge condition in each capacitor. Using switching state redundancies, the voltage controller drives directly the converter to keep the capacitors voltages balanced and guarantee the voltage level requested by the current controller.

3.4.1   Current control

The current controller must be robust since the load parameters R and L are time varying and the output inverter voltage (V_o) has discrete levels which introduce discretization errors that

act as input perturbation to the load.

Figure 3.7 shows the current control loop:
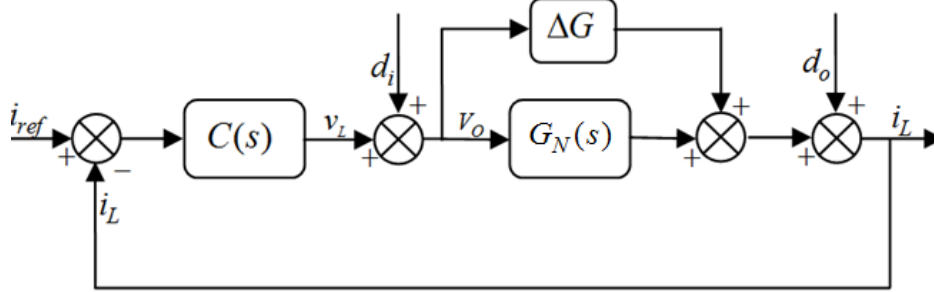
Fig. 3.7 Loop shaping block diagram

- d_i: is the input perturbation due to discretization levels of V_o.

- d_o:is the measurement errors modeled as output perturbation.

Let $G_N(s)$ the nominal transfer function corresponding the nominal values: R_N, L_N.

$$G_N(s) = \frac{b_N}{s + a_N} \tag{3.15}$$

where: $a_N = \frac{R_N}{L_N}$, $b_N = \frac{1}{L_N}$.

When the parameter varies as $R = R_N + \Delta R$ and $L = L_N + \Delta L$ the transfer function parameters change to $a = a_N + \Delta a$ and $b = b_N + \Delta b$, hence we obtain a new transfer function:

$$G(s) = G_N(s) + \Delta G(s) \tag{3.16}$$

The modeling error ΔG is unknown since it is related to parameter variations of the load. The perturbation d_o is due to errors in the measurement of the current i_L.

d_i: is the perturbation generated by the fact that has only discrete value ($-\frac{E}{2}$, $-\frac{E}{6}$, $+\frac{E}{6}$ and $+\frac{E}{2}$) while the requirement voltage v_L is continuous. It can be shown that: $d_i \leq \frac{|\frac{E}{2} - \frac{E}{6}|}{2} = \frac{E}{6}$.

The nominal closest loop system ($\Delta G = 0$) is governed by:

$$i_L = \frac{C(s)G_N(s)}{1 + C(s)G_N(s)} i_{ref}(s) + \frac{1}{1 + C(s)G_N(s)} d_o(s) + \frac{G_N(s)}{1 + C(s)G_N(s)} d_i(s) \tag{3.17}$$

Let $S_y = \frac{1}{1 + C(s)G_N(s)}$ and $T_y = \frac{C(s)G_N(s)}{1 + C(s)G_N(s)}$ One has:

$$i_L = T_y(s)i_{ref}(s) + S_y(s)d_o(s) + G_N(s)S_y(s)d_i(s) \tag{3.18}$$

Hence in order to achieve performance in the frequency range $[0, w_{B_p}]$. It must be $S_y \ll 1$ and $G_N S_y \ll 1$.

This can be formulated as $\|W(s)S_y(s) < 1\|$, where $W(s)$ is a low pass filter having high gain in the frequency range $[0, w_{B_p}]$.

This will give $i_L \simeq i_{ref}$ in the presence of perturbations d_i and d_o.

For uncertainty dynamics it is admitted that $|T_y(jw) < 1|$ in order to maintain stability in the presence of $\Delta(G)$. One has $|T_y(jw)| < -20\,dB$ for $w < w_{B_p}$.

Controller design

The first step is to determine a static performance controller $C_1(s)$, and the second step is to design a dynamic performance controller $C_2(s)$.

The corrector $C_1(s)$ ensures a high gain at low frequencies, which implies a minimization of the sensitivity function S_y and thus ensure a good accuracy in steady state.

The form of the static performance is: $C_1(s) = K_c$. From figure 8, to reach the extended plant $L_1(jw_c) = C_1(jw_c)G_N(jw_c)$ at the crossover frequency $w_c = \frac{R}{L} = 5000\,rad/s$. One has $C_1(s) = 200$.

In order to satisfy the dynamics specifications and ensure stability specifications, the current loop gain $L_1(jw_c)$ is examined at the crossover frequency (w_c), yielding:

- $\|L_1(j5000)\| = 23\,dB$.

- $\angle L_1(j5000) = -45\,deg$.

At (w_c), the gain needs to be decreased by: $\Delta M = 0 - 23 = -23\,dB$.

By evaluating the actual values of the extended plant magnitude and phase at the desired crossover frequency (see Fig. 3.8), a suitable compensator for dynamic performance to accomplish this is to use a lag compensator, which has the form:

$$C_2(s) = \frac{1 + 0.024\,s}{1 + 0.00133\,s} \tag{3.19}$$

The final controller is of the following form:

$$C(s) = C_1(s)C_2(s) = 200\,\frac{1 + 0.024\,s}{1 + 0.00133\,s} \tag{3.20}$$

From figure 3.9, one can see that the output perturbation d_0 is attenuated by $28\,dB$ in low frequency range. The input perturbation d_i due to discretization levels of the inverter voltage is attenuated by $45\,dB$. In the frequency range beyond $5000\,rad/s$, the robustness condition
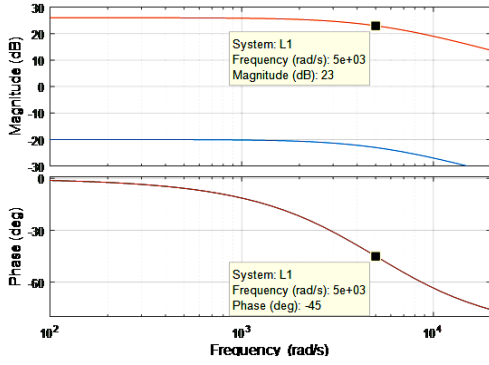
Fig. 3.8 Frequency response of L1(s) and plant
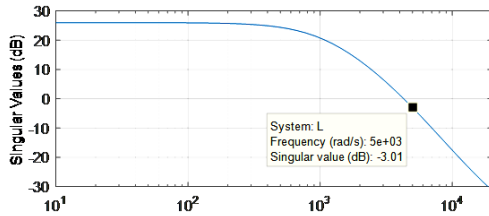
Fig. 3.9 Frequency response of Plant with controller
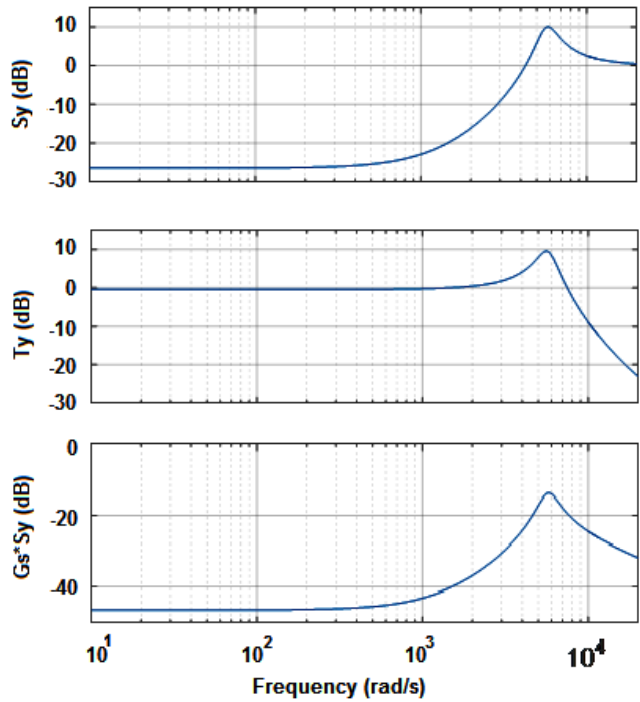
Fig. 3.10 Gain of frequency response of Sy,Ty and GSy

in the presence of the modeling error ΔG is satisfied since one has $|S_y(jw)| < -20\,dB$. The sensitivity function, the complementary sensitivity function and the load disturbance sensitivity are presented in Figure 3.10. It is apparent that the transfer function is close to unity over those frequencies, and the system exhibits good tracking characteristics. Finally, the transfer function from load disturbance d to process output y for the system, the transfer function goes to $-45\,dB$ for small frequencies, to reject plant disturbances.

3.4.2 Hybrid mode voltage control Strategy

In this section a new algorithm for voltage control is derived to ensure the asymptotic stability of the errors: $e_{v_1} = e_{v_{c_{1ref}}} - e_{v_{c_1}}$ and $e_{v_2} = e_{v_{c_{2ref}}} - e_{v_{c_2}}$.
One has the following result:

Theorem 2: Consider the three cell inverter and assume that the required level is α_i. If q_i is chosen as follows:

$$
q_i =
\begin{cases}
q_0 \ \ if \ \ \alpha_i = -2 \\
q_7 \ \ if \ \ \alpha_i = +2 \\
q_1 \ \ if \ \ i_L e_{v_{c_1}} > 0 \ \ \alpha_i = -1 \\
q_2 \ \ if \ \ (i_L e_{v_{c_1}} < 0) \ \& \ (i_L e_{v_{c_2}} > 0) \ \ \alpha_i = -1 \\
q_4 \ \ if \ \ i_L e_{v_{c_1}} < 0 \ \ \alpha_i = -1 \\
q_3 \ \ if \ \ i_L e_{v_{c_2}} > 0 \ \ \alpha_i = +1 \\
q_5 \ \ if \ \ (i_L e_{v_{c_1}} > 0) \ \& \ (i_L e_{v_{c_2}} < 0) \ \ \alpha_i = +1 \\
q_6 \ \ if \ \ i_L e_{v_{c_1}} < 0 \ \ \alpha_i = +1]
\end{cases}
\tag{3.21}
$$

Then the tracking errors ($e_{v_{c_1}}$ and $e_{v_{c_2}}$) are asymptotic stable.

Proof:

Consider the following Lyapunov function;

$$
V = \frac{1}{2} e_{v_{c_1}}^2 + \frac{1}{2} e_{v_{c_2}}^2
\tag{3.22}
$$

The time derivative is:

$$
\Delta V = \dot{V} = i_L e_{v_{c_1}} \frac{S_2 - S_1}{C_1} + i_L e_{v_{c_2}} \frac{S_3 - S_2}{C_2}
\tag{3.23}
$$

Taking into account the possible values of S_k, one has:

$$
\dot{V} =
\begin{cases}
\dot{V}_0 = \dot{V}_7 = 0 & if \ \ q_i = q_0 \, or \, q_7 \\
\dot{V}_1 = -\frac{i_L e_{v_{c_1}}}{C_1} & if \ \ q_i = q_1 \\
\dot{V}_2 = \frac{i_L e_{v_{c_1}}}{C_1} - \frac{i_L e_{v_{c_2}}}{C_2} & if \ \ q_i = q_2 \\
\dot{V}_3 = -\frac{i_L e_{v_{c_2}}}{C_2} & if \ \ q_i = q_3 \\
\dot{V}_4 = \frac{i_L e_{v_{c_2}}}{C_2} & if \ \ q_i = q_4 \\
\dot{V}_5 = -\frac{i_L e_{v_{c_1}}}{C_1} + \frac{i_L e_{v_{c_2}}}{C_2} & if \ \ q_i = q_5 \\
\dot{V}_6 = \frac{i_L e_{v_{c_1}}}{C_1} & if \ \ q_i = q_6
\end{cases}
\tag{3.24}
$$

If $\alpha_i = -1$ then there are three modes (q_1, q_2, q_4) that can give this output level. Computing $\dot{V}$ for three modes, one gets $\dot{V}_1 = -\frac{i_L e_{v_{c_1}}}{C_1}$, $\dot{V}_2 = \frac{i_L e_{v_{c_1}}}{C_1} - \frac{i_L e_{v_{c_2}}}{C_2}$ and $\dot{V}_4 = \frac{i_L e_{v_{c_2}}}{C_2}$. By selecting the mode that makes $\dot{V} < 0$. One gets the control signals given in the theorem .

For $\alpha_i = 1$ then there are three possible modes (q_3, q_5, q_6). Computing for three modes, one gets $\dot{V}_3 = -\frac{i_L e_{v_{c_2}}}{C_2}$, $\dot{V}_5 = -\frac{i_L e_{v_{c_1}}}{C_1} + \frac{i_L e_{v_{c_2}}}{C_2}$ and $\dot{V}_6 = \frac{i_L e_{v_{c_1}}}{C_1}$ By selecting the mode that makes $\dot{V} < 0$ one gets the sequence signals given in theorem 2.

Therefore, at each time interval $DeltaV \leq 0$ applying the second Lyapunov theorem, one can conclude that $\dot{V}$ is a semi definite function and therefore $e_{v_{c_1}}$ and $e_{v_{c_2}}$ are bounded. By applying La Salle theorem, the invariant set ensuring $\dot{V} = 0$ for all possible S_i is reduced to $e_{v_{c_1}} = e_{v_{c_2}} = 0$.

End proof:

3.5   Simulation Results

In this section, based on the above proposed hybrid LS control method, the simulation is done under PSIM (software power electronics simulations) in order emulate the realistic behavior of the overall system's components. In fact, PowerSim Software models better the realistic nonlinear behavior of the elementary elements of the inverter including non-perfect switches. For all the simulations the load is assumed to be inductive (with $R = 10\,Ohm$ and $L = 2\,mH$, the capacitor $C_1 = C_2 = 47\,\mu F$ and $E = 480V$ (Fig. 3.11). The states of the switches are
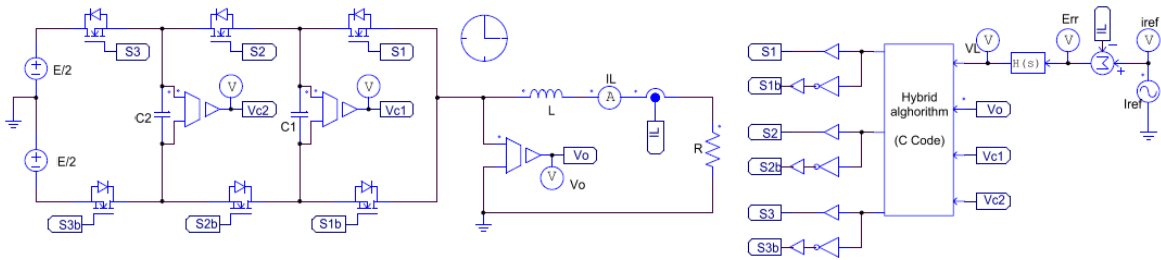
Fig. 3.11 LS/Hybrid control design of three cells inverter with PSIM software

shown in figure. 3.12, it can be notice that the adjacency rules are satisfied.

Figure 3.13 shows the load current, it has a sinusoidal form with a frequency of $50\,Hz$ and amplitude that does not exceed the maximum current $i_{max} = E/2R$. The same figure illustrates the voltages across capacitors C_1 and C_2. The voltage v_{c_1} increases and stabilizes around its reference.

The output voltage in the figure has four levels that respect adjacency and guaranties asymptotic stability of the tracking errors. The output voltage v_{c_1} is delayed with respect to
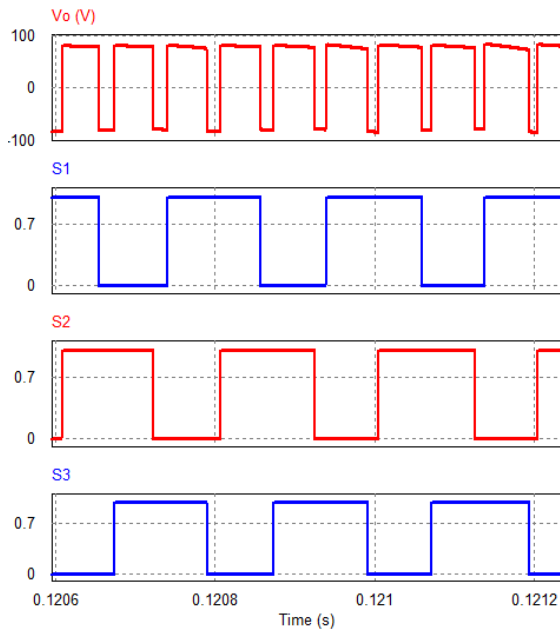
Fig. 3.12 Switches State
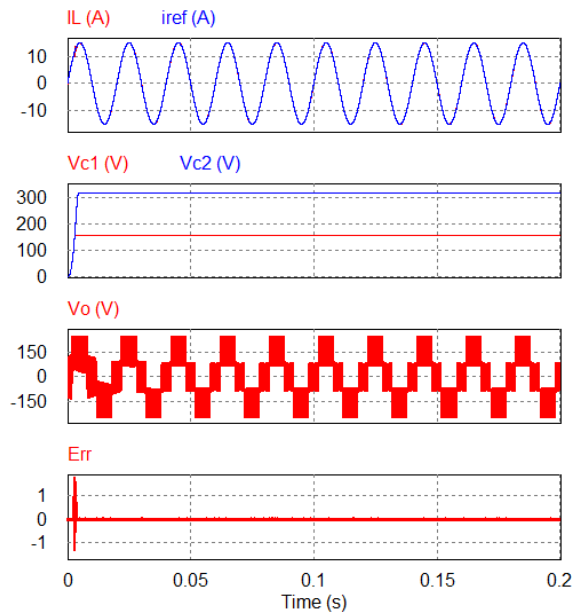
Fig. 3.13 HLS controller Nominal Test

the voltage v_{c_2} due to the initial conditions.

The tracking error $Err = i_{ref} - i_L$ is also plotted in figure 3.13. One can see the effect of voltage unbalancing in the transient time on the tracking error. The latter takes big values since the output voltage V_o cannot reach the desired level. In the steady state, the voltages are balanced and hence the tracking error (Err) is reduced.

The advantage of the hybrid control is highlighted since it does not require either the balancing circuit or the PWM, the inverter states are controlled directly through a predefined selection table. Also, the controller allows the stability of floating voltages v_{c_1} and v_{c_2}.

The FFT spectrum of the charging current is shown in fig. 3.14 and the current THD is 1.26 %. The direct control via the proposed selection table of theorem 2 removes harmonic distortion and gives a sinusoidal and inductive current.
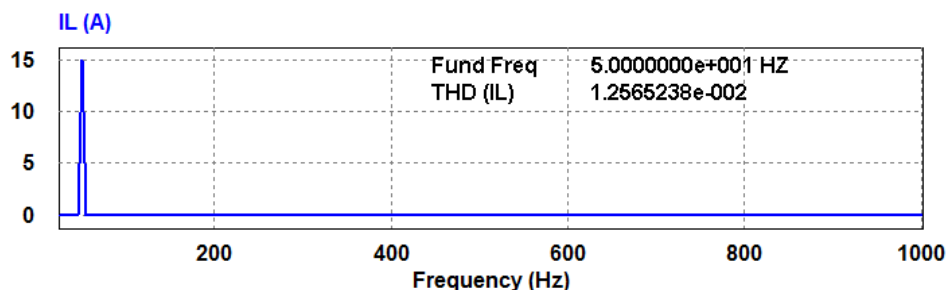
Fig. 3.14 Load current THD analysis

3.6   Robustness tests

Three robustness tests are considered.

3.6.1   Parametric variations

Robustness to load variations (R)

In order to test robustness to load variations, we perform sudden load variation of +100 % to -50 %. The results of this test are shown in Figure 3.15. Note that despite a change of the load *R* from 10 to 15 *Ohm*, the voltage at the terminal of the resistor is in phase and proportional to the load. Note also a slight voltage variation across the capacitors but the floating voltages remain stable.

Robustness to inductance variation (L)

Figure 3.16 shows the response to a sudden increase in inductance of +100 % ($L = 4$ *mH*), then a decrease of -50 % ($L = 1.5$ *mH*) of the latter. Note that the intermediate voltages across the capacitors (v_{c_1} and v_{c_2}) remain stable, the current remains sinusoidal despite a small ripple from the value ($L = 1.5$ *mH*).
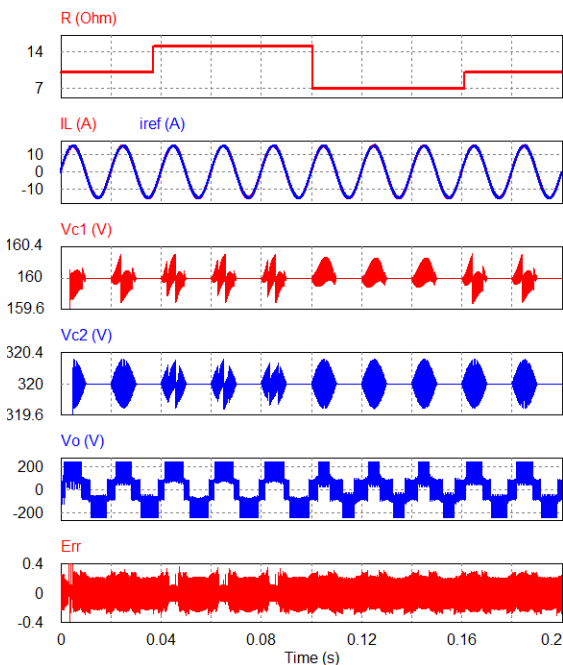
Fig. 3.15 Robustness to load (R) variation   Fig. 3.16 Robustness to inductance variation
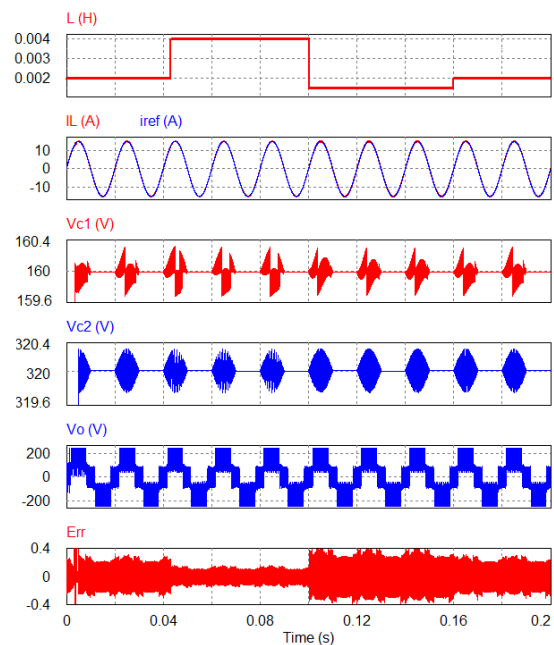
Robustness in frequency variations (f)

In this section, a robustness test to frequency variations applied to the reference signal is presented. For this, a lower frequency ($f = 40\ Hz$) and a frequency higher ($f = 80\ Hz$) than the nominal frequency were taken as the reference frequency. Figures 3.17 and 3.18 show that there are no changes in the floating voltages and the output voltage. Hence, the performances are maintained for variable frequency reference current.
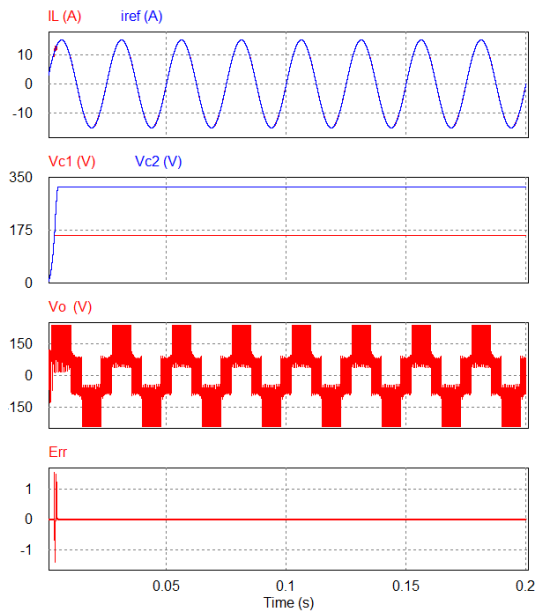
Fig. 3.17 Robustness to frequency variations ($f = 40\ Hz$)
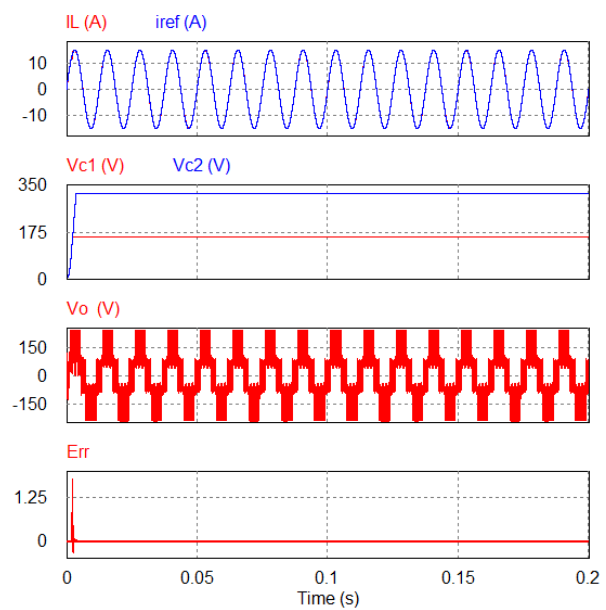
Fig. 3.18 Robustness to frequency variations ($f = 80\ Hz$)

3.6.2   Disturbance

In order to test the robustness of the control strategy under variable DC source voltage, adding at time $t = 0.04\ s$ a voltage of $40\ V$; and at the instant $t = 0.25\ s$, then lowering it from 520 to $440\ V$.

Figure 3.19 shows the evolution of the load current, it is clear that the tracking is maintained. Despite the source voltage drop with a variation of more than 16 % which is a strong disturbance for the system, the floating voltages quickly move to their new equilibrium values. The current then goes through a slight overshoot but is quickly regulated to follow the reference.
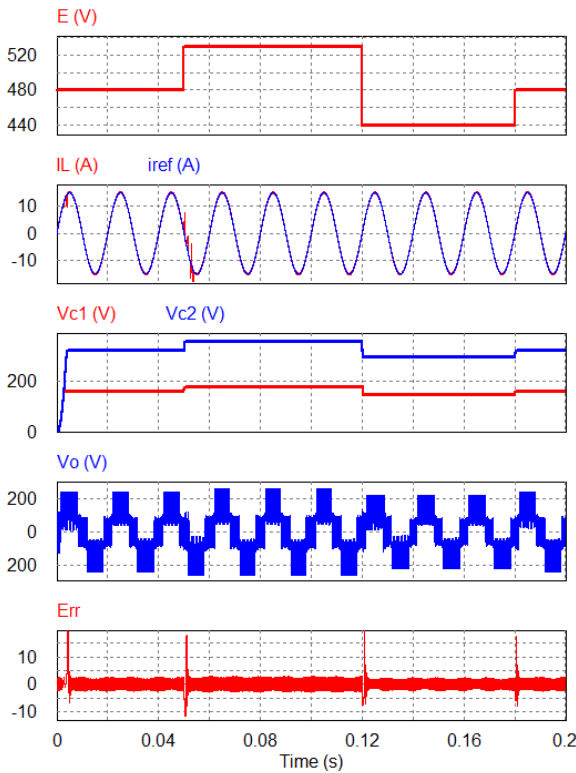
Fig. 3.19 HLS controller Disturbance test.
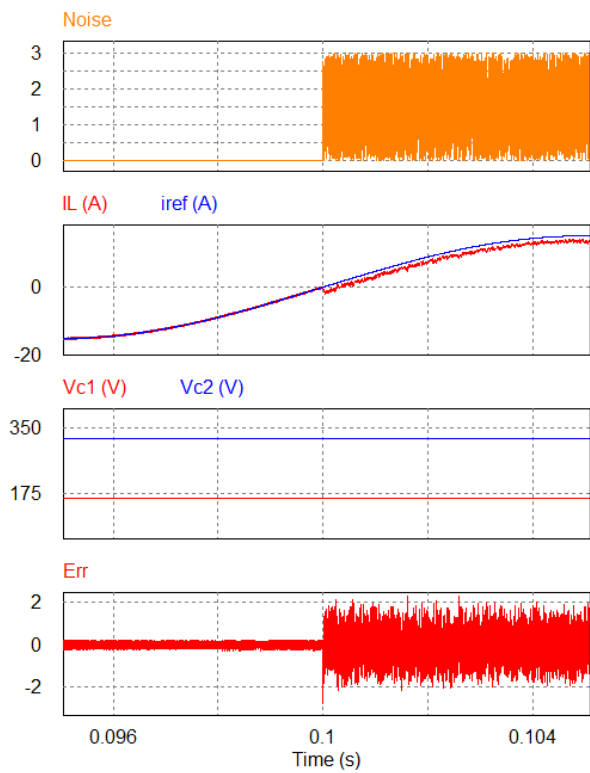
Fig. 3.20 HLS controller noise measurement test.

3.6.3   Measurement noise

A white noise is added to the charging current. The noise amplitude is about 3.5 V, that is 23 % of the peak load current. The effects related to current measurement noise are illustrated in figure 3.20. Despite a slight disturbance of the output current, the latter has virtually no influence. The only phenomenon that is remarkable is the increase in error.

3.7   Conclusion

In this chapter, a new cascaded hybrid robust loop shaping control of three cell inverter is developed. Firstly, the three cells instantaneous model is derived and the control problem is formulated as two cascaded current/voltages loops. Then, the hybrid model of the inverter is discussed. Secondly, a new algebraic condition is developed in order to fulfill the adjacency constraint that allows minimizing energy losses. Thirdly, the design of the two control loops is presented.

The proposed controller is derived by combining loop shaping method for the current loop and hybrid control for the voltage loop. To this end, a new hybrid control algorithm is

proposed based on the hybrid model of the inverter.

Of particular importance, asymptotic stability of the overall control system is proven by Lyapunov theory using a suitable Lyapunov function. In this algorithm, the states of the inverter are directly controlled by a predefined selection table that is chosen to force negativeness of the Lyapunov function time derivative.

The feasibility and effectiveness of the proposed control scheme is evaluated with intensive simulation in a virtual experimental setup. The obtained results show that the proposed control scheme is more efficient and robust compared to existing approaches. In fact, the proposed approach is very simple since it does not require either the balancing circuit or PWM. Furthermore, it reduces the execution time by using an offline HLS controller with a predefined selection table for the switches.

Chapter 4

Ripple-Correlation MPPT, Hybrid/Sliding-Mode control

Chapter 4

Ripple-Correlation MPPT, Hybrid/Sliding-Mode control

4.1 Introduction

In order to enhance the performance and efficiency of the new hybrid control studied in the previous chapter, two controllers are proposed. The first controller is used to improve the efficiency and track the maximum power point of the PV generator under variable solar irradiance conditions and variable load. This new controller is referred to in the literature as Ripple Correlation Control (RCC). The second controller consists of a cascaded sliding mode control (SMC) for the current loop and a hybrid control for the voltage loop. The proposed controller would ensure that energy is transferred from the PV generator (GPV) to the load while also regulating the load's requirements.

4.2 Sliding mode controller design

The system is highly nonlinear due to the inherent nonlinear characteristics of the PV generator and the load. Therefore, other control approaches are required to enhance the robustness and stability of the system. In this section, a Hybrid/Sliding Mode Control (HSMC) strategy is proposed to control the instantaneous active and reactive powers.
The aim of the HSMC is to ensure good performance and fast transient response under large parameter variations and external disturbances. This control strategy is well known for its robustness, stability and good dynamic response under the wide range of operating conditions [103, 82, 122, 89, 43].

The basic SMC is designed in two steps: (1) Design of a suitable sliding surface in the state space and (2) Bring the system state from any initial condition towards the desired equilibrium point of the state space when time tends to infinity [45].

4.2.1 Sliding surface design

The sliding surface is designed to achieve the desired system dynamics. To maintain the system on the sliding surface, a switching control law is developed that forces the system states to meet the reaching condition [55]. The switching control law is given by:

$$u_n = sign(S(x))$$ (4.1)

where $S(x)$ denotes the sliding surface. The above control law is a switching function which shows that the controller output depends on the sliding surface .

Referring to (Fig. 3.1) and using equations (3.1) and (3.2), the ac current side derivative can be written as:

$$\frac{di_L}{dt} = -\frac{R}{L}i_L + \frac{v_L}{L}$$ (4.2)

$$= ai_L + bu$$ (4.3)

where: $a = -\frac{R}{L}$ and $b = \frac{1}{L}$.

Defining the tracking error between the inverter output current and the pv reference current as $e = i_L - i_{ref}$, where i_L is the output current of the inverter, i_{ref} represents the pv reference current.

The inverter current of equation 4.3 can be treated as a first order system, Thus, the sliding function is given by:

$$S = H(e)$$ (4.4)

while the sliding surface can be written as:

$$S = i_L - i_{ref}$$ (4.5)

4.2.2 Controller design

The global control law u consists of two terms: the equivalent control term u_{eq} and the nonlinear control term u_n.

$$u = u_{eq} + u_n \tag{4.6}$$

During non-sliding mode, the control law u_n ensures that the condition of attractivity of the surface S, is expressed by:

$$u_n = k\, sign(S(x)) \tag{4.7}$$

Therefore, the global control law can be defined as:
During sliding mode, the surfaces S become zero as well as their derivatives:

$$\dot{S} = \frac{di_L}{dt} - \frac{di_{ref}}{dt} = ai_L + bV_L - \frac{di_{ref}}{dt} \tag{4.8}$$

where the equivalent control term u_{eq} can be obtained by solving the following equation:

$$\dot{S} = 0 \tag{4.9}$$

The existence condition for sliding mode operation can be obtained by using Lyapunov's direct method to solve $S\dot{S} < 0$, which gives the existence region of the sliding mode. Substituting (4.7) and (4.8) in (4.9), the equivalent control laws u_{eq} and u_n can be obtained as:

$$S[ai_L - \frac{di_{ref}}{dt} + bV_L] < 0 \tag{4.10}$$

$$u = V_L = \frac{1}{b}[-ai_L - k\, sign(S)] \tag{4.11}$$

4.3 Ripple correlation control MPPT

The maximum power point tracking (MPPT) algorithms are employed to improve the efficiency of the PV arrays. Several methods have been presented in Chapter 2. The main difficulty of these algorithms is to find an appropriate perturbation step size. In addition, these methods have a poor MPP tracking capability during sudden variations in solar irradiance. The Ripple Correlation Control (RCC) algorithm [117, 79, 22] is more efficient, has a

faster response, and does not require any external perturbation as compared to other MPPT algorithms [123, 136].It is suitable for single-phase configurations [23, 59].

4.3.1   Background

The RCC approach uses the converter current and voltage ripples as the perturbation to extract information about the operating point [60, 61]. The value of power derivative ($\frac{\partial P}{\partial v}$) is an important variable which defines the reference PV voltage v_{ref} in the dc-link voltage controller to reach the MPP [34].

The instantaneous value of the power injected into the load is:

$$P_{out}(t) = v_{out}(t)i_{out}(t) = V_m \cos(wt)I_m \cos(wt) = \frac{V_m I_m}{2}(1 + \cos 2wt) \tag{4.12}$$

Where V_m and I_m are the amplitude of the inverter voltage and current, and $w = 2\pi f$ is the inverter angular frequency ($f = 50Hz$). Assuming that voltage and power are periodic functions, the average components of voltage and power can be written as follows:

$$\bar{v} = \frac{1}{T}\int_{t-T}^{t} v(\tau)d\tau \tag{4.13}$$

$$\bar{p} = \frac{1}{T}\int_{t-T}^{t} p(\tau)d\tau \tag{4.14}$$

Hence, that the output voltage and power of the PV panels are given by:

$$v = \bar{v} + \check{v} \tag{4.15}$$

$$p = \bar{p} + \check{p} \tag{4.16}$$

where $\check{v}$ and $\check{p}$ are voltage and power alternative components (ripple components).

The maximum power-point operating voltage for a given temperature and irradiance is obtained by solving:

$$\frac{\partial P}{\partial v} = 0 \tag{4.17}$$

The derivative of the power with respect to the voltage ($\frac{\partial P}{\partial v}$) for the considered working point v_0 can be linearized around the nearby average operating $p_0 = p(v_0)$. This leads to the

following relation between power ripple and voltage ripple:

$$\check{p}(t) = (\frac{\partial p}{\partial v})_{v_0} \check{v}(t) \tag{4.18}$$

Then, the average of the product of p and v, is obtained as:

$$\int_{t-T}^{t} \check{p}(\tau)\check{v}(\tau)d\tau = (\frac{\partial p}{\partial v})_{v_0} \int_{t-T}^{t} \check{v}^2(\tau)d\tau \tag{4.19}$$

Therefore, the power derivative can be calculated as follows:

$$(\frac{\partial p}{\partial v})_{v_0} = \frac{\int_{t-T}^{t} \check{p}(\tau)\check{v}(\tau)d\tau}{\int_{t-T}^{t} \check{v}^2(\tau)d\tau} \tag{4.20}$$

4.3.2   Implementation of the RCC MPPT algorithm

In order to implement the RCC algorithm, the block diagram representing the estimation of $\frac{\partial P}{\partial v}$ by previous calculations is summarized in figure 4.1. Highpass filters (HPFs) can be used instead of (4.13) and (4.14), to extract ripple components. Lowpass filters (LPFs) can be used instead of the moving averaging integrals of (4.19).

According to equation (4.19), the sign of the integral corresponds to the sign of the power
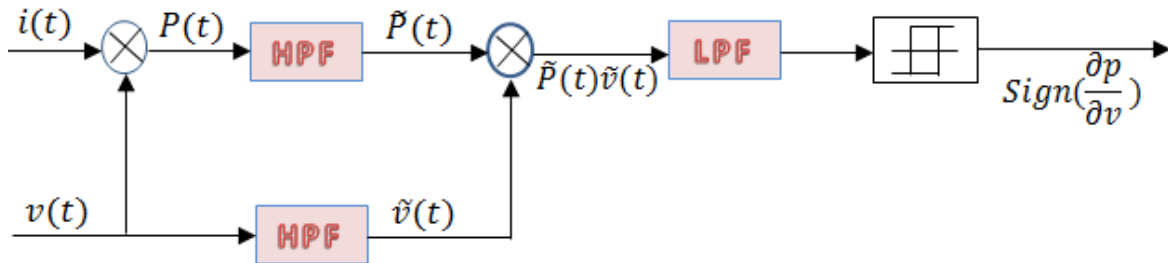
Fig. 4.1 Block diagram of the RCC algorithm

derivative ($\frac{\partial P}{\partial v}$):

$$sign(\int_{t-T}^{t} \check{p}(\tau)\check{v}(\tau)d\tau) = sign(\frac{\partial p}{\partial v})_{v_0} \tag{4.21}$$

The quantity $sign(\frac{\partial p}{\partial v})$ is a clear indication of the region where the PV panel is working (Fig 4.2):

- $(\partial p/\partial v)$ means: the sign function is +1,Then, The operating point is on the left hand side of the MPP on the (p, v) characteristic. ($\check{p}$ and $\check{v}$ are in phase agreement.)

- $(\partial p/\partial v)$ means $\check{p}$ and $\check{v}$ are in phase opposition. The operating point is on the right hand side of the MPP on the (p, v) characteristic.
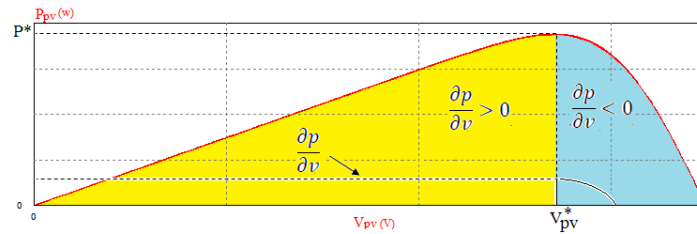
Fig. 4.2 Ripple Correlation Control Flow Diagram

Based on the relationships 4.19 and 4.21, integral control with a suitable gain can be applied over time to adjust ΔV. By adding the initial voltage reference (V^*), when $Sign(\partial p/\partial v) > 0$, the integrator increases by ΔV and is added to (V^*), conversely, when $Sign(\partial p/\partial v) < 0$, the (V^*) decreases by ΔV. The estimated voltage derivative of the power $(\partial p/\partial v)$, drives the working point toward the MPP and provides the reference dc-link voltage.

By tracking the reference value v^*_{ref} allows the PV panels to converge to the optimal operating condition $(\partial p/\partial v) = 0$ (maximum power operating point). The corresponding block diagram is depicted in fig 4.3).
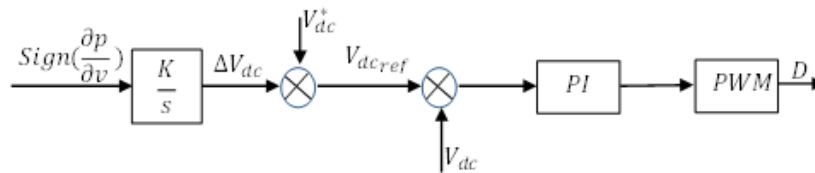
Fig. 4.3 Block diagram of the RCC algorithm to estimate DC-link voltage

4.4 Cascaded Sliding Mode /hybrid mode control design of three-cell inverter

Observing the internal topology of the multi-cell inverter and applying the previous two control strategies, it can be divided based on the number stages of processing power: Dual-stage inverter (With DC/DC stage) is shown in (Fig.1.2), inverter with one stage of power processing (Without DC/DC stage) shown in (Fig.1.3).

4.4.1   Dual stage inverter

In this configuration the MPPT is directly connected to the DC-DC stage. The main advantage of this method is that it has better control of each PV module see [28, 66, 32]. Regarding RCC MPPT, the reference voltage to control the DC-DC stage is shown in figure 4.4. Assuming that the power extracted by the generator is delivered to the load (i.e. $P_{pv} = P_L$), the reference voltage is calculated by dividing the power by the current drawn by a load.

The control of the multicell inverter is provided by two cascade loops. The first loop is the current control, is provided by SMC, as discussed previously. the second loop is the voltage control and is provided by the hybrid control, as we saw in the previous chapter.
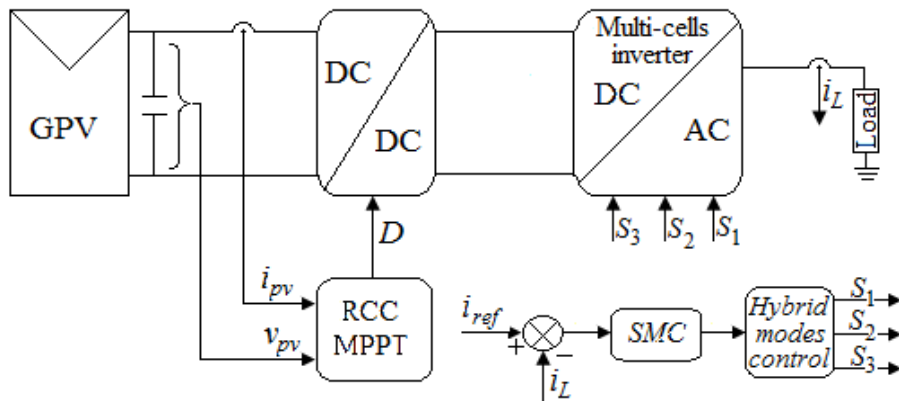
Fig. 4.4 Control of two stage inverter with HSMC control

4.4.2   One stage inverter

This configuration of the inverter includes the MPPT controller, the voltage boost, and the load current control in a single stage, which must handle all functions on its own.

Such a concept allows a low number of components, a low cost and a high efficiency compared to the traditional two power stage [152, 56]. To form a multi-string configuration, each string is connected to an inverter, which allows improving the reliability of the system; losses due to partial shading are minimized because each string can operate at its own MPPT. This increases the flexibility in the design of the PV system as new strings can be easily integrated into the existing system to increase its rated power.
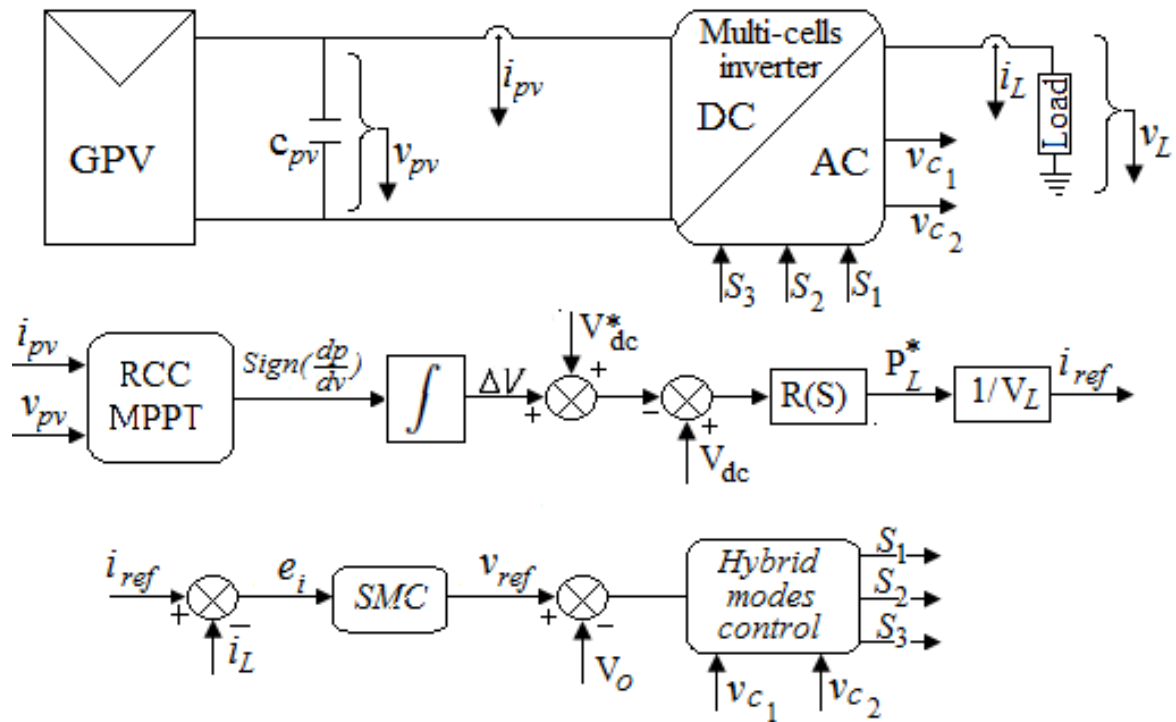
Fig. 4.5 Control of one stage inverter

Control method

In order to control the current of the inverter, we need the reference current (i_{ref}). Assuming the power extracted from the GPV is the same at the load, therefore, to calculate the output reference current, we divide by the output voltage (V_{out}).

Power Decoupling or Dc link

A single-stage inverter requires an input voltage which can be high enough to avoid a voltage increase so that the voltage switching ripple increases as well. To reduce PV side power ripples, a DC capacitor's size has to be kept as small as possible [14, 97]. The dc-link capacitance can be calculated according to the equation (4.22), witch gives the value of required decoupling capacitor 3, where I_{dc} and ΔV_{dc} are the input-current ripple and the dc link voltage ripple. asymmetric.

$$C_{dc} = \frac{i_{dc}}{2\pi f \Delta V_{dc}} \tag{4.22}$$
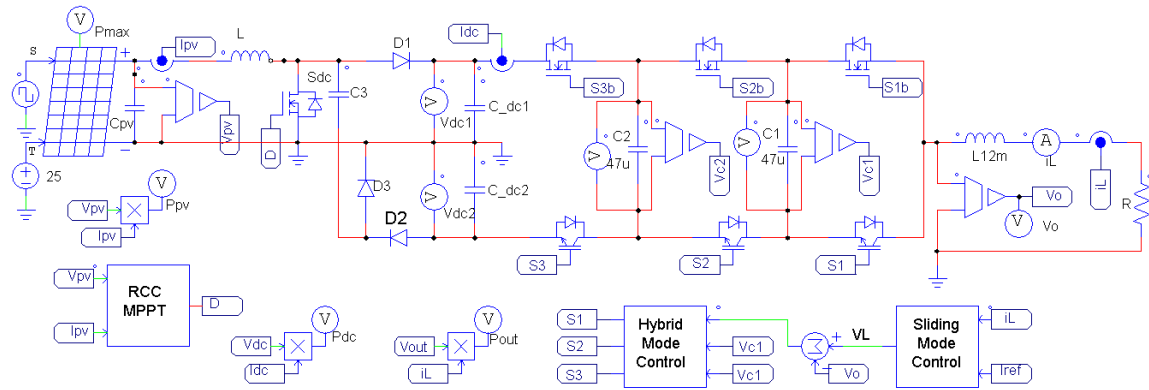
Fig. 4.6 SMC/hybrid control design of three cells inverter with PSIM software

4.5 Simulation Results

4.5.1 Dual stage inverter

In this configuration of figure 4.6, the control of the multicell inverter is provided by two cascaded loops. The first loop is the current control and is provided by SMC, while The second loop is the voltage control and is provided by hybrid control, as discussed in Chapter 3.

Figure 4.7 depicts the variation of solar irradiance values, as well as the effect of changing the maximum power delivered, current, and GPV voltage. It can be seen that the solar irradiation decreases at time $t = 2\,s$ from $1000\,W/m^2$ to $600\,W/m^2$, and then increases again at t = 3.75 s, to settle at $900\,W/m^2$. Despite this almost 40 % change in solar irradiation, the system remains stable and robust.

These results were obtained for a switch duty cycle of 0.6. Figure 4.8 shows the waveforms of the DC output voltage. It can be observed that the average output voltage is E=480 V and the voltages across the capacitors C_1 and C_2 are half of the total DC voltage. The sliding surface, controller output, AC current error, and control switches are presented in figure 4.9. The simulation results for step increase and decrease in power as a result of changes in solar irradiation are shown in figure 4.10.

4.5.2 One stage inverter

A single-stage photovoltaic inverter must achieve both functions in this case: extracting maximum power from the panel and generating a reference sinusoidal current wave for the current needed by the load.

Figure 4.13 shows the solar irradiance, the waveforms of the PV power, current, and voltage
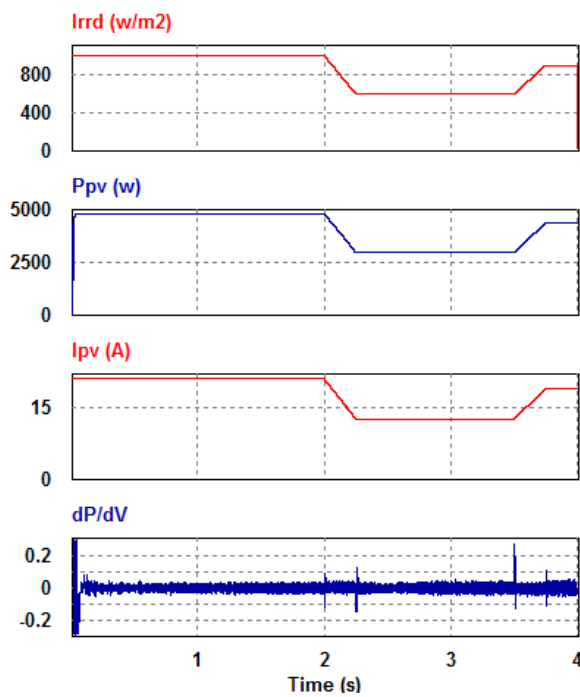
Fig. 4.7 Pv outputs power, current and voltage   Fig. 4.8 Boost converter output voltages
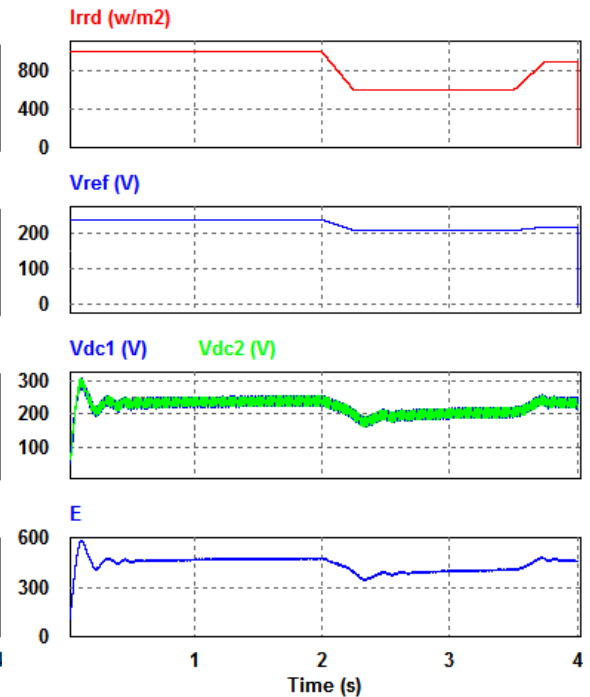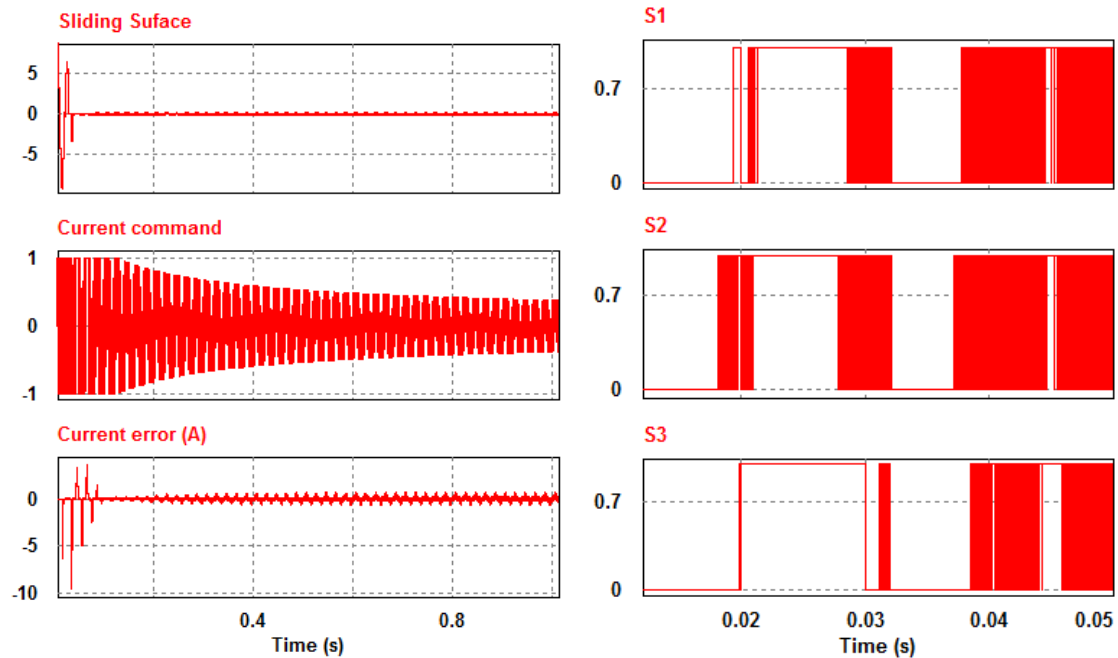
Fig. 4.9 Sliding surface, Current error and Control switches (S1, S2 and S3)
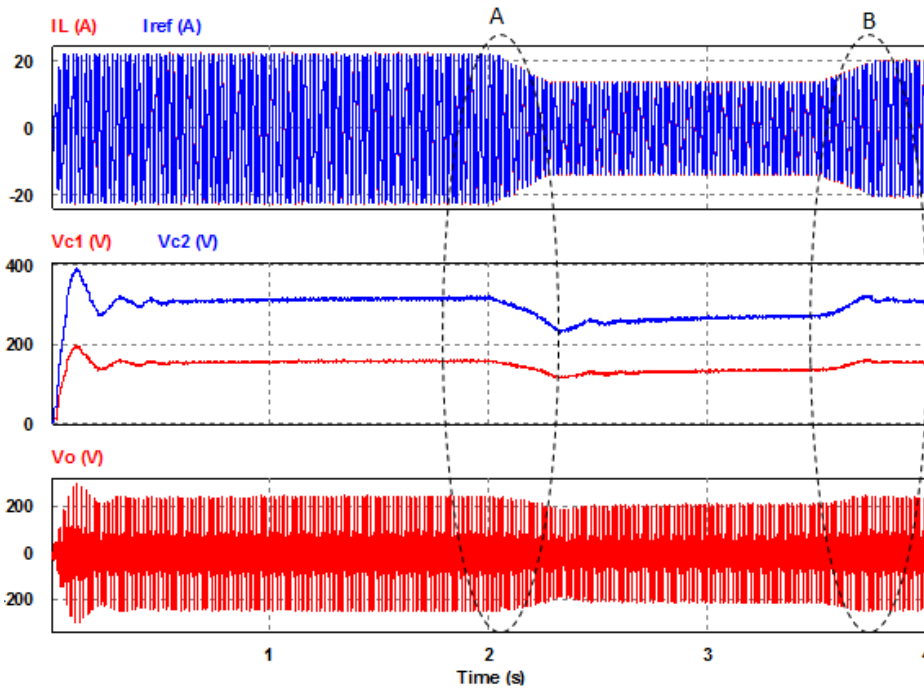
Fig. 4.10 Steady state response of current, floating and output voltage of the inverter
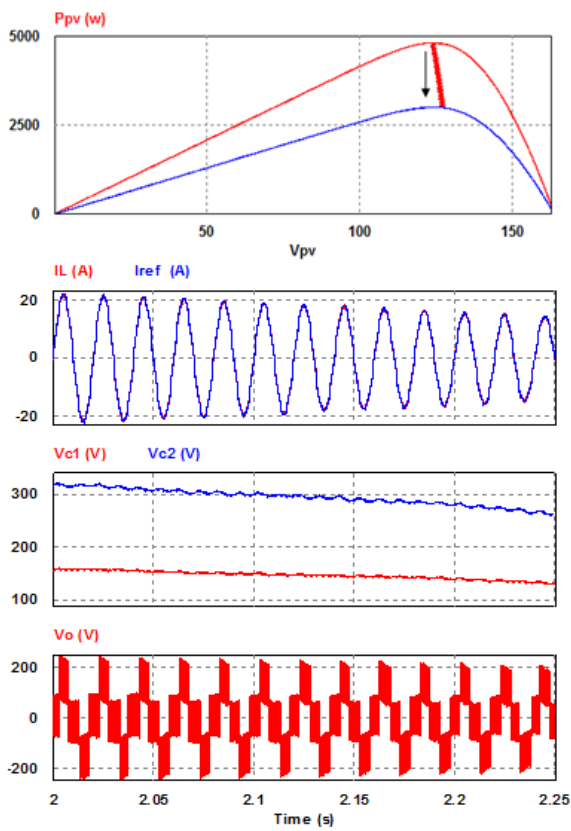
Fig. 4.11 Power decrease, case (A)   Fig. 4.12 Power increase, case (B)
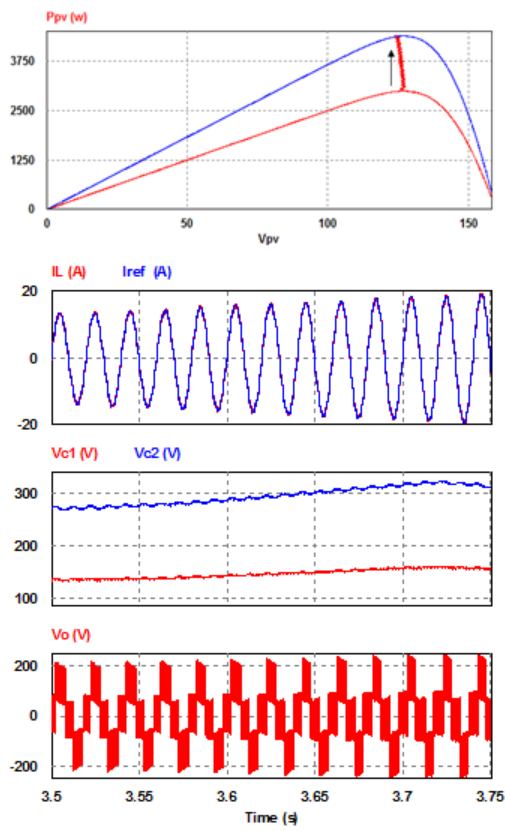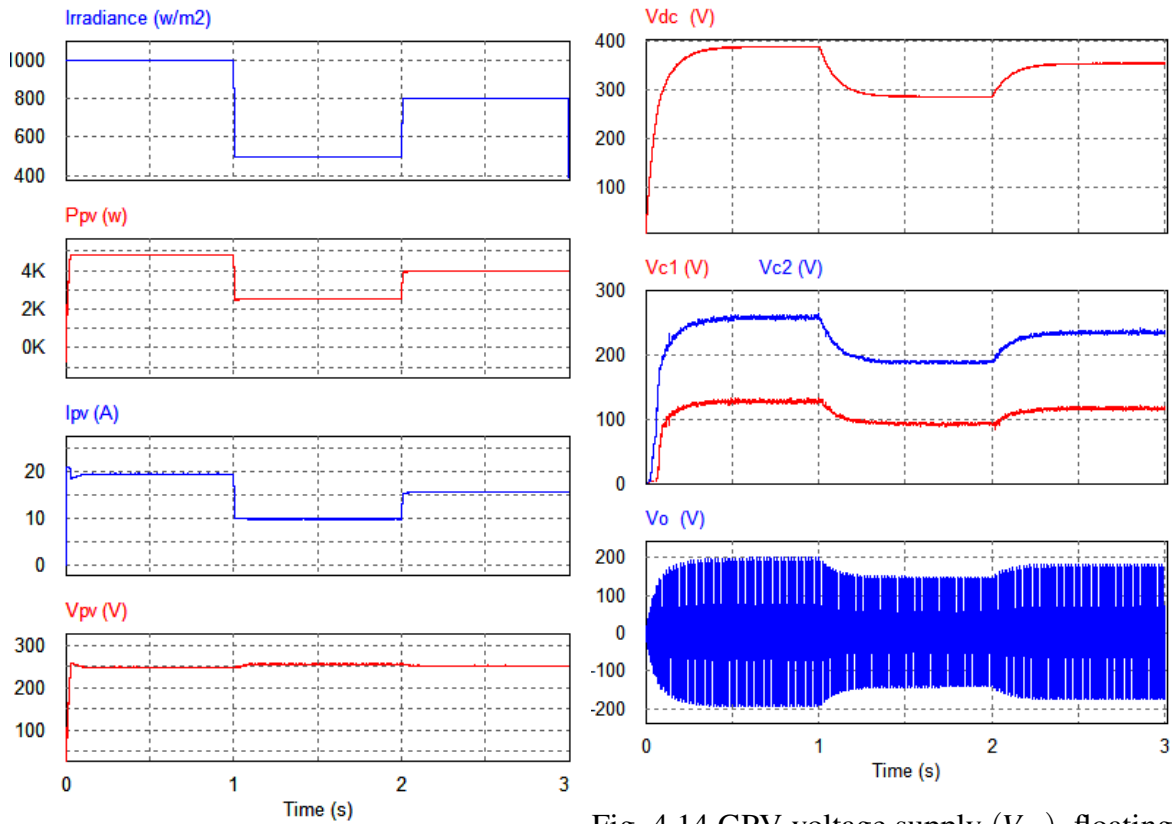
Fig. 4.13 Irradiance values, GPV output power, current and voltage.

Fig. 4.14 GPV voltage supply (V_{dc}), floating voltages (V_{c1}, V_{c2}) and output voltage of inverter (V_o).
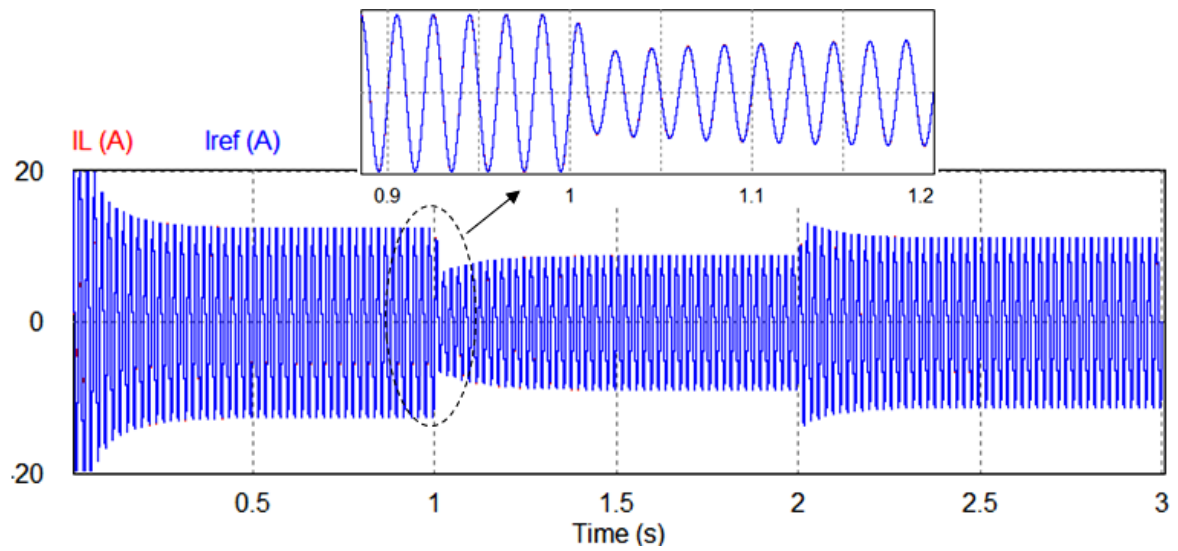
Fig. 4.15 Reference and load current of the inverter.

over $3\,s$.

At steady state, when the irradiation drops to half ($t = 1\,s$), the power drops to half as well, and when the irradiation rises at $t = 2\,s$, the power rises as well, owing to the proper operation of the mppt. When the power is at its peak ($P_{max} = 4830\,w$), the DC voltage is at its peak ($V_{max} = 388\,V$). The steady state and transient states depicted in the figure 4.14 both confirm the good performance achieved by the RCC-MPPT algorithm.

The proposed method, as shown in figure 4.14, balances the voltages of the Flying Capacitor multicel inverter to their target values of $V_{c1} = \frac{V_{dc}}{3} = 129V, V_{c2} = \frac{2V_{dc}}{3} = 259V$. Furthermore, despite the drop in the supply voltage, the floating voltages follow their reference values. This clearly demonstrates the ability of the proposed active voltage balancing method to perfectly track the dc link voltage and balance the voltages of the inverter at varying reference values.

As shown in fig 4.15, the reference current requested by the load is calculated by the following method: $I_{max} = P_{pv}/V_{dc} = 12.46A$. Despite its simplicity, this method allows all of the power delivered by the GPV to be transferred to the load.

4.6   Conclusion

In this chapter, a new cascaded control scheme combining a sliding mode control (SMC) for the load current and hybrid control for the voltage loop has been presented. A maximum power optimization based on the RCC algorithm has also been proposed. The proposed cascade control has been implemented and tested, successfully with a three-cell inverter topology.

In the case of a three cell inverter. A comparison of the proposed algorithms SMC and loop-Shaping,has shown that the control performance has been improved with faster transient response and enhanced dynamic performance and the stability.

Chapter 5

Performance of New Control Strategies for PV Pumping Applications

Chapter 5

Performance of New Control Strategies for PV Pumping Applications

5.1   Introduction

The aim of this chapter is to design new control strategies to improve the stability and dynamic performance of a PV-driven water pumping system. The system consists of a submersible pump connected to a three-phase squirrel cage induction motor (IM) driven by a multicell voltage inverter.

Water scarcity in arid and semi-arid regions is a serious concern for the population. Photovoltaic systems in isolated sites is a potential alternative solution to supply these sites with electricity and water. Solar photovoltaic-based water pumping is the ideal solution for water supply wherever the electricity grid is not accessible [138, 58].

Water pumping with solar photovoltaic was initially carried out with direct current motors because it did not require an inverter. However, in recent years, the induction motor has become more popular due to its several advantages such as simple construction, robustness, reliability, low cost, high efficiency and low maintenance as compared to DC motors [114, 72, 132].

In order to achieve MPP and optimum machine efficiency, most current photovoltaic pumping systems integrate a DC-DC converter between the modules and the inverter. Therefore, there is a need to use a single-stage controlled drive to pump water to reduce switching losses and the number of switches, thereby reducing the number of switches and losses. GPV should keep the MPP in a single stage [134, 106]. This configuration is ideal for medium powers, therefore better in terms of performance, size and cost [96].

The overall control scheme consists of two control loops. The first controller is the RCC algorithm which aims to improve the efficiency at the point of maximum power of the GPV system; this algorithm is coupled with the Indirect Field Oriented Control (IFOC) technique to generate a variable frequency PWM signal to control the IM Motor.

In the remainder of this chapter, firstly, the modeling of the IM will be studied, then the modeling and calculation of the necessary power of the pump and IM, and finally the system implemented using PSIM software and several simulations results are presented to demonstrate the performance of the proposed control scheme.
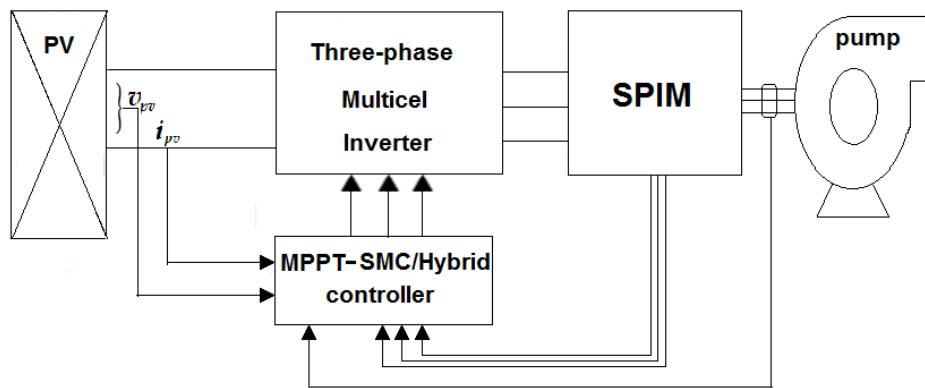
Fig. 5.1 Proposed photovoltaic water pumping system.

5.2 Three Phase Induction Motor

Three-phase induction motor is widely used in water pumping due to its robust construction and low cost, it has higher efficiency and lower than the DC motors [133, 27].

To improve the efficiency of the IM motor and minimize the number of required solar panels, the machine is connected in delta with 220 V instead of 380 V. This connection makes motor design really simple and efficient.

5.2.1 Modeling of Three Phase Induction Motor

Due to a large number of equations to be solved of the three-phase induction motor, using Park's transformation, The motor model can be represented by an equivalent two-phase machine [126, 115, 83]. The equivalent circuits of the IM are shown in Fig. 5.2.

The dynamic model equation of the three-phase induction motor can be represented in the d, q reference frame. The stator and rotor voltages components of the two-phase induction motor can be expressed as follows.

(a) D-axis circuit

(b) Q-axis circuit
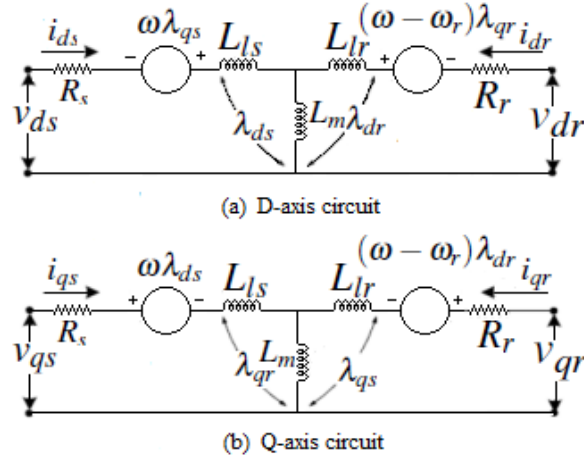
Fig. 5.2 d-q equivalent circuit of Induction Motor

$$\begin{cases} v_{ds} = R_s i_{ds} + \frac{d}{dt}\Psi_{ds} - \omega_r\Psi_{qs} \\ v_{qs} = R_s i_{qs} + \frac{d}{dt}\Psi_{qs} + \omega_r\Psi_{ds} \end{cases} \qquad (5.1)$$

$$\begin{cases} v_{dr} = 0 = R_r i_{dr} + \frac{d}{dt}\Psi_{dr} - (\omega - \omega_r)\Psi_{dr} \\ v_{qr} = R_r i_{qr} + \frac{d}{dt}\Psi_{qr} + (\omega - \omega_r)\Psi_{dr} \end{cases} \qquad (5.2)$$

The components of the stator and rotor flux linkages can also be expressed as:

$$\begin{cases} \Psi_{ds} = L_{ls} i_{ds} + L_m(i_{ds} + i_{dr}) \\ \Psi_{qs} = L_{ls} i_{qs} + L_m(i_{qs} + i_{qr}) \\ \Psi_{dr} = L_{lr} i_{dr} + L_m(i_{ds} + i_{dr}) \\ \Psi_{qr} = L_{lr} i_{qr} + L_m(i_{qs} + i_{qr}) \end{cases} \qquad (5.3)$$

The equation of motion of the mechanical system can be expressed by:

$$T_e - T_L = J\frac{d\omega}{dt} + f\omega \qquad (5.4)$$

The torque equation in dq coordinate is given by:

$$T_e = P\frac{L_m}{L_r}(\Psi_{dr} i_{qs} - \Psi_{qr} i_{ds}) \qquad (5.5)$$

Where: T_e and T_L are the electromechanical torque and load torque (N.m) respectively, P is the number of poles pair, J: represents the inertia Nm^2 and ω_n denotes the mechanical speed

rad/s of the rotor.

The IM parameters used in this study are provided in Table 5.1

Table 5.1 Induction motor parameters

Parameter	Value
Rated power (Pn)	4060 *w*
Rated voltage (Vn)	220 *V*
Rated current (full load) (In)	16.41 *A*
Rated Speed (Ω_n)	2863 *rpm*
Stator resistance (Rs)	0.7629 Ω
Rotor resistance (Rr)	0.5131 Ω
Stator inductance (Ls)	2.053e-06 *H*
Rotor inductance (Lr)	0.002945 *H*
Mutual inductance (Lm)	0.03747 *H*
Pole pair (P)	2

5.2.2 Field Oriented Control for Induction Motor

One of the most popular and most widely used control technique for IM drives is vector control or field-oriented control (FOC), which is designed for controlling the magnitude and phase of the voltage or current vectors [29, 39, 36, 118].

Important improvements have been made in the control of IM by combining FOC with modern control approaches. as recently described in the literature. for example, with backstepping [99, 30], Integral backstepping [81], input-output linearization [86] sliding modes [153, 98], passivity [139], fuzzy logic [53, 11], direct torque control [4, 10], among others.

This controller technique has been extensively applied to variable speed motors and motion control due to high dynamic performance. It can be operated successfully at very low frequencies.

The aim of FOC is to decouple the flux and torque, and keep them perpendicular to each other in order to generate the maximum torque. In that way, the flux and torque can be adjusted independently like in a separately excited dc motor [25, 95]. In this special reference frame the q-axis component of the rotor flux becomes zero. The rotor flux space vector becomes a

real variable: $\Psi_{qs} = 0$, so that $\Psi = \Psi_{dr}$. Equation 5.5 becomes

$$T_e = P\frac{L_m}{L_r}\Psi_{dr}i_{qs} \qquad (5.6)$$

IFOC drivers obtains the rotor flux orientation via an indirect way, which is achieved by the measured rotor shaft position and the calculate slip angle.

Field-Oriented Control of a current-fed induction motor

The current regulation loop in voltage source inverters offers significant advantages to improve the dynamics of the drive system. These inverters can achieve high dynamic current control with an excellent transient response as a result of a direct comparison of the inverter output current with the current reference signal.

To control the speed of the motor, it is necessary to control the stator currents of the machine in order to obtain the flux and the torque. It consists of a control system, a current controlled PWM inverter and an induction machine [137, 135, 42].

$$\begin{cases} i_{qs}^* = \frac{L_r T_e^*}{P L_m \Psi_r^*} \\ i_{ds}^* = \frac{(1+L_r)\Psi_r^*}{L_m} \end{cases} \qquad (5.7)$$

Figure 5.3 describes the methodology of IFOC for induction motor drives, The reference
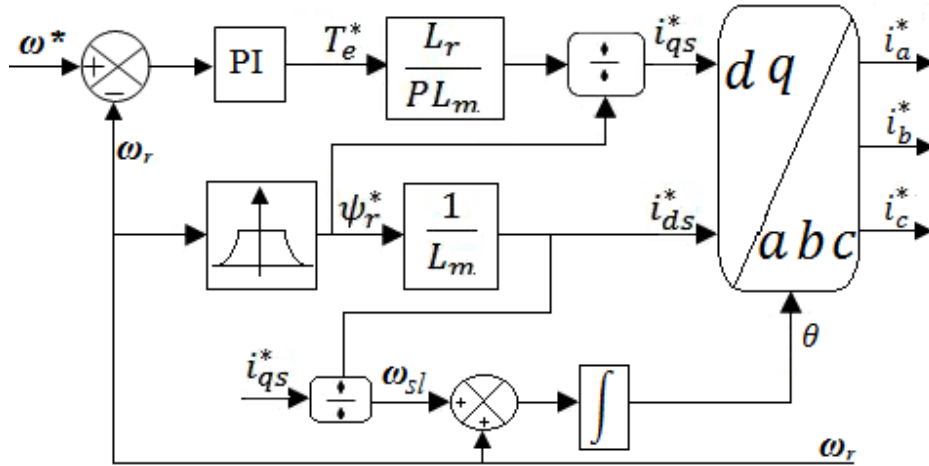
Fig. 5.3 IFOC diagram

torque T_e^* is obtained from the speed controller. This control signal is used as input for the stator reference current of the axis q via Eq. 5.5. The d-axis stator current reference value

through the field-weakening block is obtained by equation 5.7.

The details of the SMC Hybrid control on cascade control with the three-phase multicellular inverter and the three-phase induction motor are shown in figure 5.4.
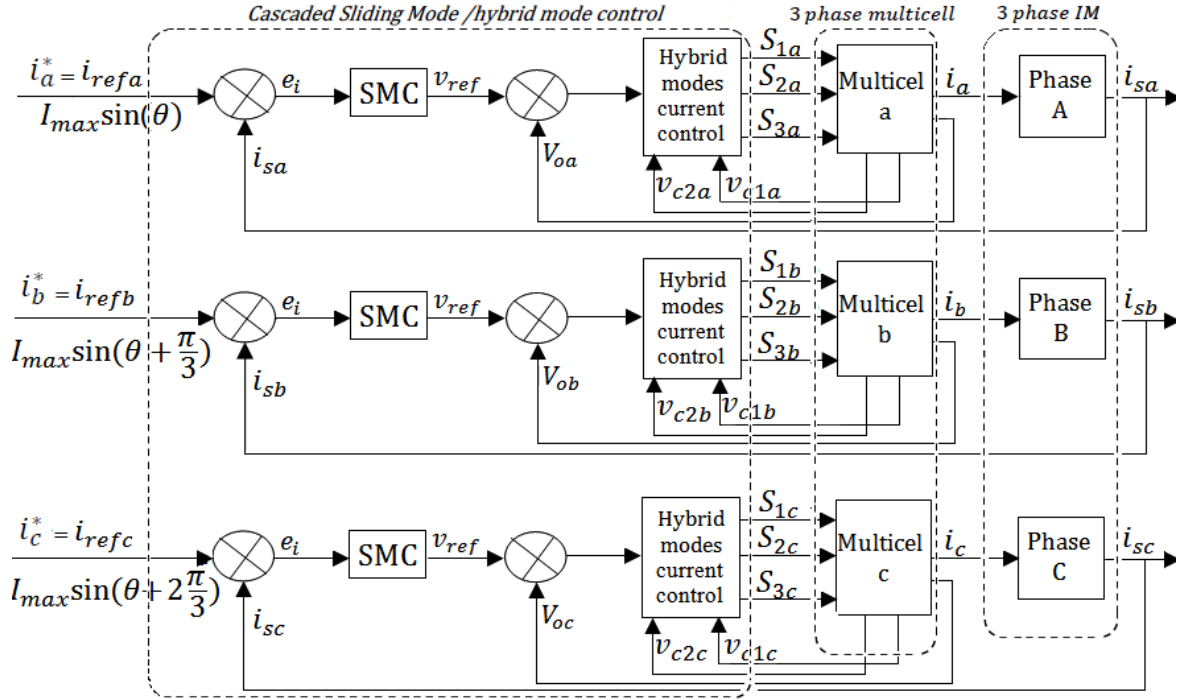
Fig. 5.4 Block diagram of the H/SMC control of three-phase induction motor

PI speed controller

The external speed regulation loop will be defined by the parameters (K_{pw} and K_{iw}). This can be established, from the equation of mechanics governing the dynamics of rotating system, the relationship between speed and electromagnetic torque:

$$\Omega = \frac{1}{Js+f}(T_e - T_L) \tag{5.8}$$

The closed loop transfer function of a control system is given by:

$$\frac{\Omega}{\Omega_n} = \frac{(K_p + \frac{K_i}{s})\frac{1}{Js+f}}{1 + (K_p + \frac{K_i}{s})\frac{1}{Js+f}} \tag{5.9}$$
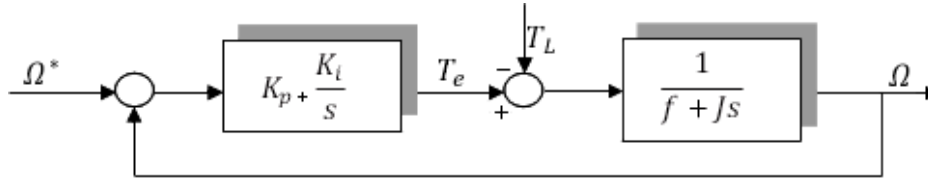
Fig. 5.5 Equivalent diagram of PI Controller of Speed Regulation

This reveals a characteristic polynomial that also defining second order dynamics. In the same way as previously (eq 2.9), By identification:

$$\begin{cases} \frac{1}{\omega_0^2} = \frac{1}{K_i}, K_i = \omega_0^2 \\ \frac{2\xi}{\omega_0} = \frac{K_p}{K_i} + \frac{f}{K_i}, K_p = 2\omega_0 J - f \end{cases} \tag{5.10}$$

5.3   Pump model and sizing

Depending on the unit head and water discharge, different pump models (centrifugal, impulse, etc.) may be used. Two types of water pumps are currently the most used for pumping: centrifugal and positive displacement. They are both designed to move water from one place to another continuously [94].

Electrical submersible pump (ESP) is that the most generally used petroleum production, geothermal machinery, and domestic water supply system thanks to its advantages of high lifting head,it is used for high flow rates and medium or shallow depths (10 to 100 meters) [107], It has good operating stability and a good range of flow adaptability [47, 33, 21]. To meet the power and design requirements of the submersible pump, the stator of the submersible motor is very narrow, giving rise to special characteristics of this type of submersible motor [149, 26, 76].

5.3.1   Calculation of Total Dynamic Head

The total dynamic head (TDH), it is important to determine the correct sizing and scale of pumping equipment needed, TDH is calculated as shown in Fig 5.6. [12, 6].

$$TDH = P_l + V_r + F_l \tag{5.11}$$
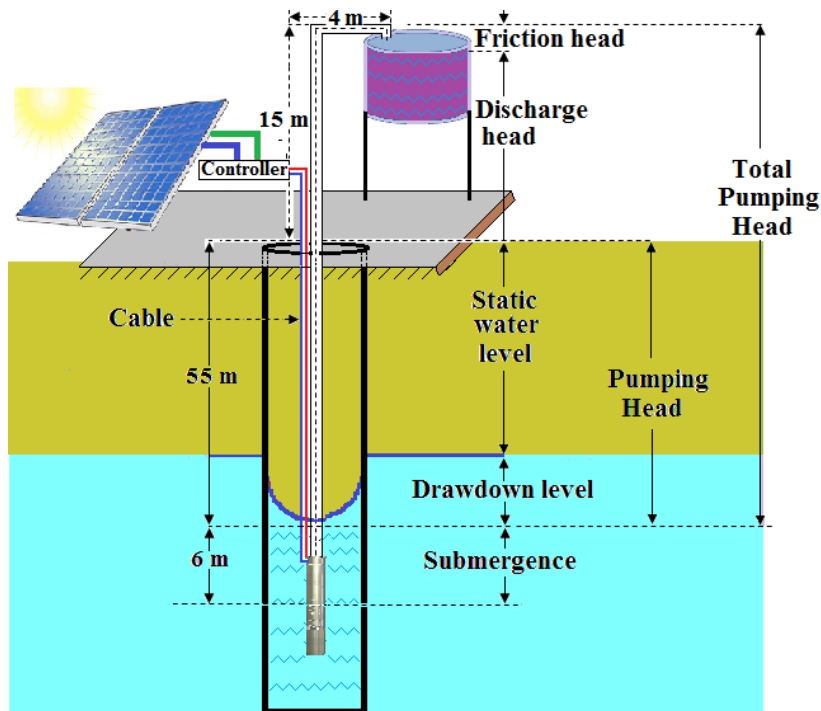
Fig. 5.6 Schematic diagram of Total Dynamic Head(TDH) of water-pumping

P_l: Pumping level = 55 m.

V_r: Vertical rise = 15 m. F_l: Friction loss, which can be defined as:

$$F_l = [L_t + \Sigma(n_f f_e)]\frac{F_h}{100} \tag{5.12}$$

where L_t:Total length of pipe =80 m.

n_f:Number of same fittings = 2 elbows.

f_e:Fittings, a standard value in feet, depending on the pipe's diameter and type = 4. Appendix[C]

F_h:Friction loss of head per $30.48\,m$ (or $100\,feet$) of pipe, depending on the pipe's diameter and flow rate. According to data are given in Appendix [B]. Friction loss is equivalent to 8.5 in this system, which has a 2-inch diameter and a 15.57 m3/h (or 57.08 GPM) flow rate.So $F_h = 6.8$.

Numerical application of Equation 3 gives the total dynamic head, TDH = 63.8 m.

5.3.2   Pump power Calculation

The rotation of the motor creates a movement of water from one point to another, which produces hydraulic power in addition to electrical power.

Electrical Power

A delta configuration has only three wires, most types of three-phase power calculations are performed using this equation:

$$P_e = VI\sqrt{3}PF \tag{5.13}$$

where V: voltage, I: current, PF: power factor.

Hydraulic Pump Power

The ideal hydraulic power depends on: differential pressure, fluid density, viscosity and flow.

$$P_H(\omega) = \frac{\rho g H Q}{3600} \tag{5.14}$$

Q = flow ($Q = 15.57\,m^3/h$)
ρ = density of fluid ($997\,kg/m^3$)
g = acceleration of gravity ($9.81\,m/s^2$)
H = differential head ($TDH = 63.81m$)

In the suggested numerical application, the differential pressure and the differential height have been set to the previous values ($H = 63.8m$, $Q = 15.57m^2$). the power will be: $P_H = 2.7\,Kw\,(3.62\,hp)$.

Shaft Pump Power

The shaft power (P_{Sh}) is the power transferred from the motor to the pump shaft. It depends on the efficiency of the pump and can be calculated as:

$$P_{Sh} = \frac{P_H}{\eta_P} \tag{5.15}$$

Depending on the characteristics of the motor chosen later (Fig.(5.8)), the pump efficiency is $\eta_P = 69.3\%$, the numerical application of the power shaft will be: $P_{Sh} = 3.89\,Kw\,(5.22\,hp)$.

5.3.3 Efficiency of the Motor-Pump

The efficiency of a combined pump-motor system is the ratio of Hydraulic power delivered (P_{Sh}) by the electric power provided to the pumping group (P). [49, 141]

$$\eta_{PM} = \eta_M \eta_P = \frac{P_{sh}}{P_e} \frac{P_H}{P_{Sh}} = \frac{P_H}{P_e} \tag{5.16}$$

5.4 Typical pump characteristics at constant speed provided by manufacturers

As a result of the previous calculations, the most suitable pump that will provide a flow rate of $15.57\,m^3/h$ to a water tank with 63 m TDH is the Grundfos pump SP 14-17-12AB6908 [54]. This submersible wellbore pump is ideal for pumping clean water and can be installed either vertically or horizontally [39,20]. This pump is also equipped with a 4 kW MS4000 motor with sand guard, mechanical shaft seal, water-lubricated plain bearings and volume compensation diaphragm. The motor is a fixed type submersible motor that offers good mechanical stability and high efficiency.

Figure 5.7 shows the system curve, pump curve, NPSH curve and efficiency curves. Graphically, the operating point is the intersection between the H-Q curve of the pump and the system curve ($H = 63.81m$, $Q = 15.57\,m^3/h$). the displayed parameters are:

- H Head. The curve H-Q of the pump is usually called the "pump curve".

- NPSH (Net Positive Suction Head).

- P1 (Electric input power), $P_1 = P_e = P_{Sh}/\eta_M$.

- P2 Shaft power.

- η_P Pump efficiency.

- η_{PM} Motor-pump efficiency

From the above values, the pump-motor efficiency was calculated as a product of the motor and pump efficiency.

The motor curves, efficacy, power factor, current, shaft power, and shaft speed of the motor are shown in Figure 5.8.
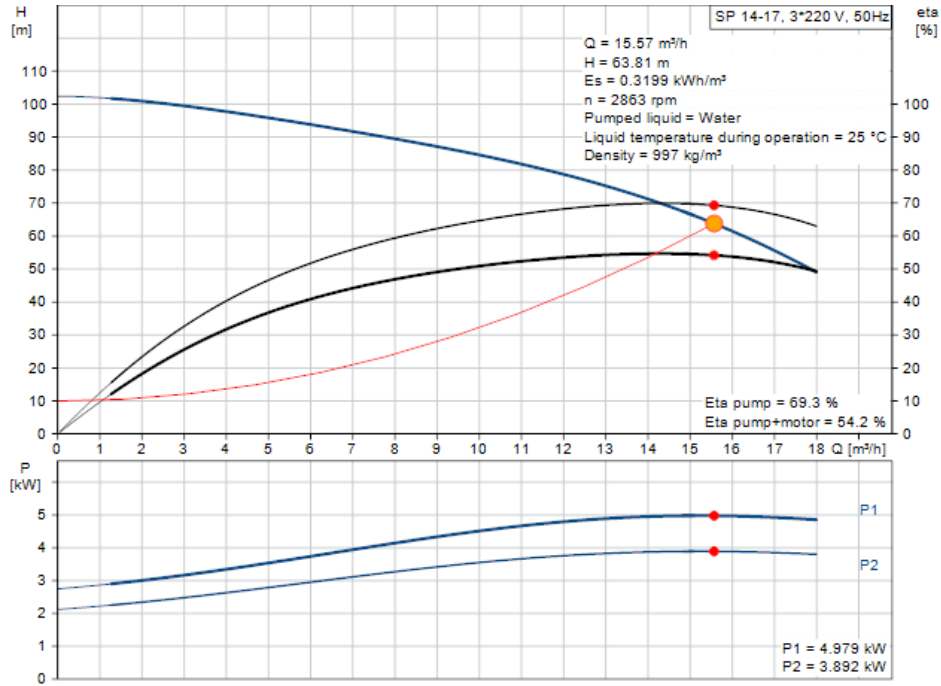
Fig. 5.7 Pump performance curves [54]

The moment of inertia of a pump is calculated using the following equation 5.17 provided by the manufacturer Appendix[D]:

$$J = (4.0 + n2.0)10^{-4} \tag{5.17}$$

where: n = number of stages = 6. The moment of inertia will be $J = 5.210^{-4}\, kg.m^2$.
The electromagnetic load torque (T_L) can be established from the power of the pump shaft in Figure (5.9)

$$T_L = \frac{P_{Sh}}{\omega_n} \tag{5.18}$$

where: $P_{Sh}=P_2 = 3892\, w$ and $\omega_n = 2\pi n/60$, the load torque: $(T_L) = 13\, Nm$.

5.5   Pumping control strategy

This proposed PV systems includes the MPPT controller, the voltage boost converter, and the load current control in a single stage, which must handle all functions on its own. This configuration leads to a reduced number of components, a low cost and a high efficiency compared to the traditional two power stage (Fig. 5.9).
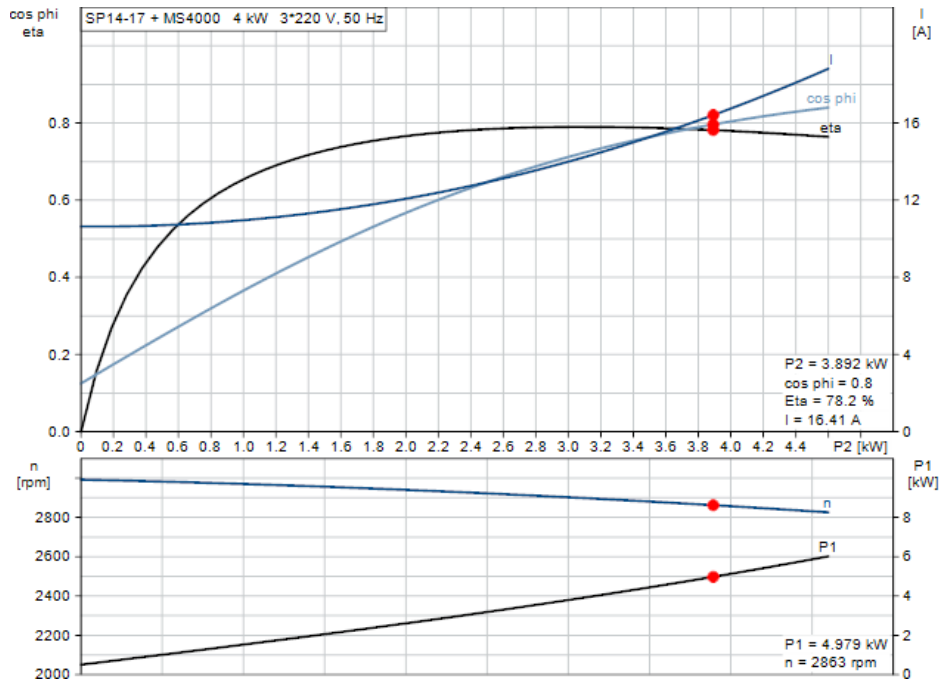
Fig. 5.8 efficiency of the motor [54]

5.5.1   PV SYSTEM

5.5.2   Maximum power point tracker (MPPT) Controller

The PV panel should be operated at point of maximum power to improve GPV system efficiency. This is achieved by using the ripple correlation control (RCC) algorithm studied in the previous chapter.

5.5.3   Current-control of induction motor drive

The current regulation loop in voltage source inverters offers significant advantages to improve the dynamics of the drive system. These inverters can achieve high dynamic current control with an excellent transient response as a result of a direct comparison of the inverter output current with the current reference signal.

The control strategy is shown in figur 5.10, this strategy is a series set of control loops using a single stage, the first control loop is the MPPT to extract the maximum power.

The motor torque in the water pumping system depends on the head, and as long as the head is constant, the load torque is also constant. This is why the power of the load is only determined by the speed of the motor equ (5.19).
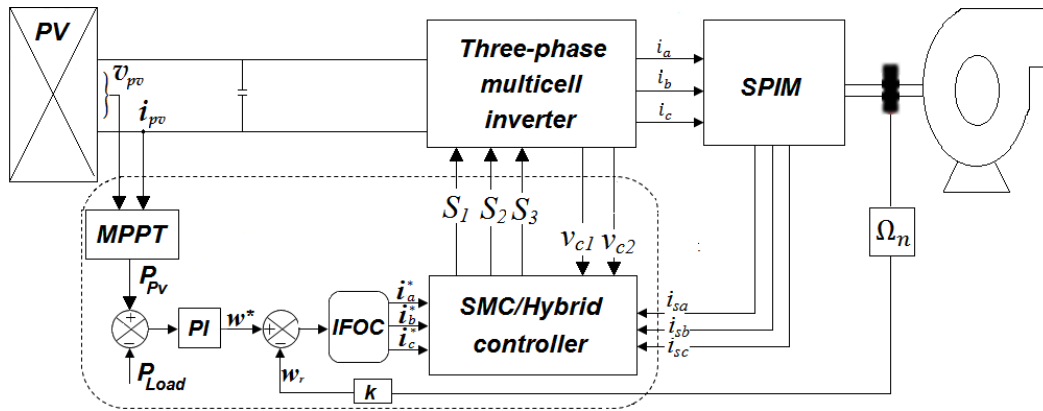
Fig. 5.9 Schematic diagram of a standalone PV water pumping system control

$$P_{Load} = P_{Sh} = \omega_r T_e = \frac{2\pi N}{60} T_e \qquad (5.19)$$

In the power-based control strategy, the reference pump speed (N^*) is generated by a controller (PI) from the difference between P_{pv} and P_{Load}. The angular speed reference (ω^*) is obtained by multiplying (N^*) by $120/P$ P being the number of poles of the IM. In order to protect the inverter and motor in the event of low power or when the power exceeds the rated value, a speed limiter is connected after the PI controller as shown in Figure 5.10. The reference speed provided generates an appropriate reference torque. Using the IFOC command to generate the current source references (i_a^*, i_b^*, i_c^*).
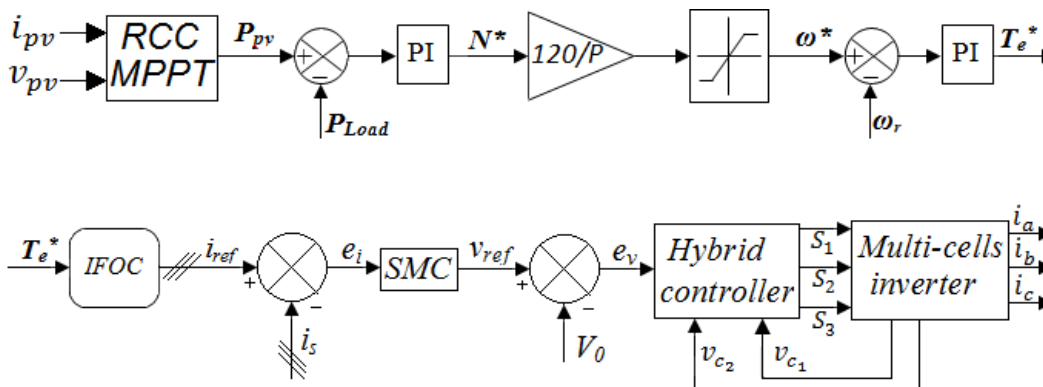
Fig. 5.10 Pumping control strategy

The reference current is obtained for the control of the multi-cell inverter. This latter is controlled by two cascading loops. The first loop is the current control, which is handled by

SMC as discussed previously. The second loop is the voltage control which is provided by the hybrid control, proposed in Chapter 3.

5.6 Simulated performance of the system

The proposed single stage solar PV feeding the IFOC controlled IM drive is modeled for water pumping, to assess the performance of the new controller of inverter for induction motor drive; simulation schematic is developed in PSIM. Based on the parameters shown in Table 5.1, a string of PV modules; 10 panels in series and 2 in parallel connected was chosen as the PV source, with the data shown in table 5.2 and appendix (1 & 2) as input.

Table 5.2 GPV characteristics

Photovoltaic Panel LG Neon2 330w	
Prameter	Value
MPP Voltage (V_{mpp})	33.3 V
MPP Current (I_{mpp})	9.77 A
Solar panels in series	10
Solar panels in parallel	2
Pole pair (P)	2

The simulation results are discussed considering the following three case studies.

5.6.1 Case study-I: Change in solar irradiance without load (Pump)

In this study, a variation in solar irradiation is simulated, starting with a full irradiation $1000 W/m^2$ and without load torque (empty). The irradiance is initially at maximum level $1000 W/m^2$ for up to 0.4 s. and then reduced from 1000 to 500 W/m^2 (Fig. 5.11 (a)). And rises again to 800 W/m^2. Despite this entire gap, the MPPT controller still delivered maximum power (Fig. 5.11.b). Figure 5.11.(c and d) show the simulated steady-state waveforms of the DC bus. The voltage is maintained constant around the desired value of $320 V$ showing an acceptable voltage ripple, while the PV current is reduced to half.

The floating voltages are shown in the Figure 5.12. Despite the low solar irradiation $500 W/m^2$, the controller was able to start the system and operate normally. These voltages perfectly follow their references $E/3$ and $2E/3$ with a short transient response as shown in Figure 5.12 (b, c and d).
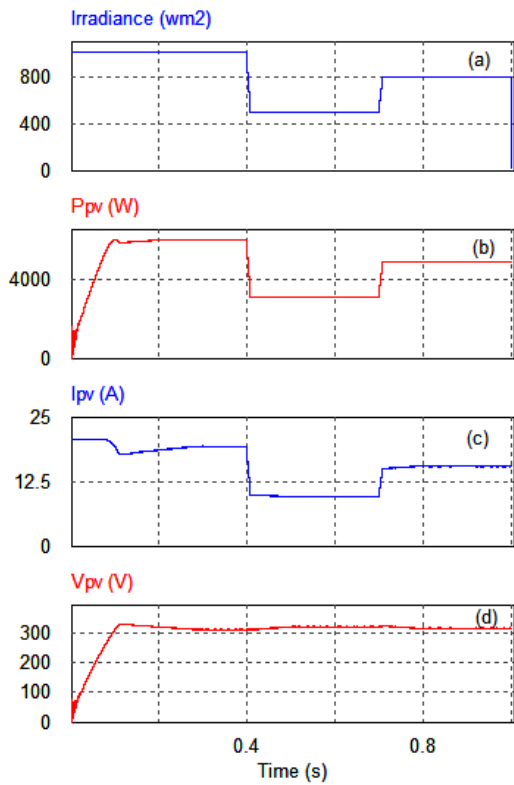
Fig. 5.11 Steady-state response of the GPV system output
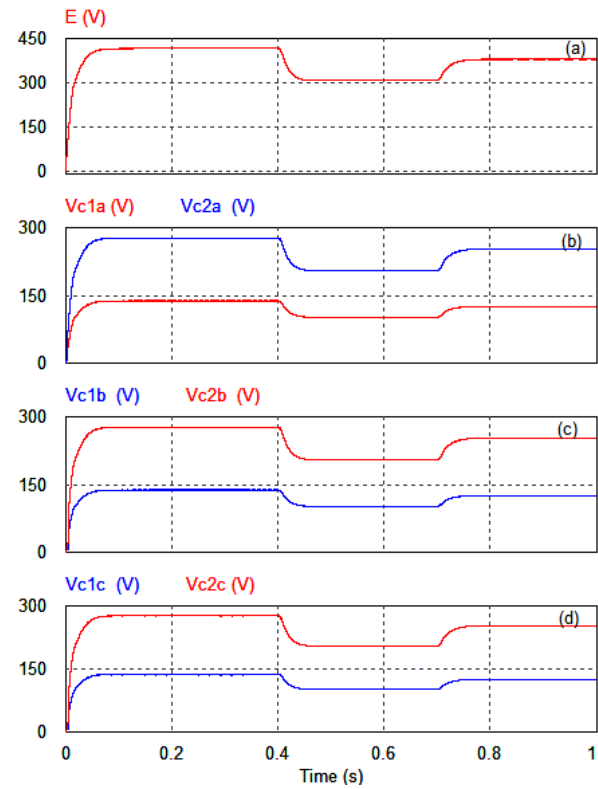
Fig. 5.12 Floating voltages (Vc1 and Vc2 a,b,c)
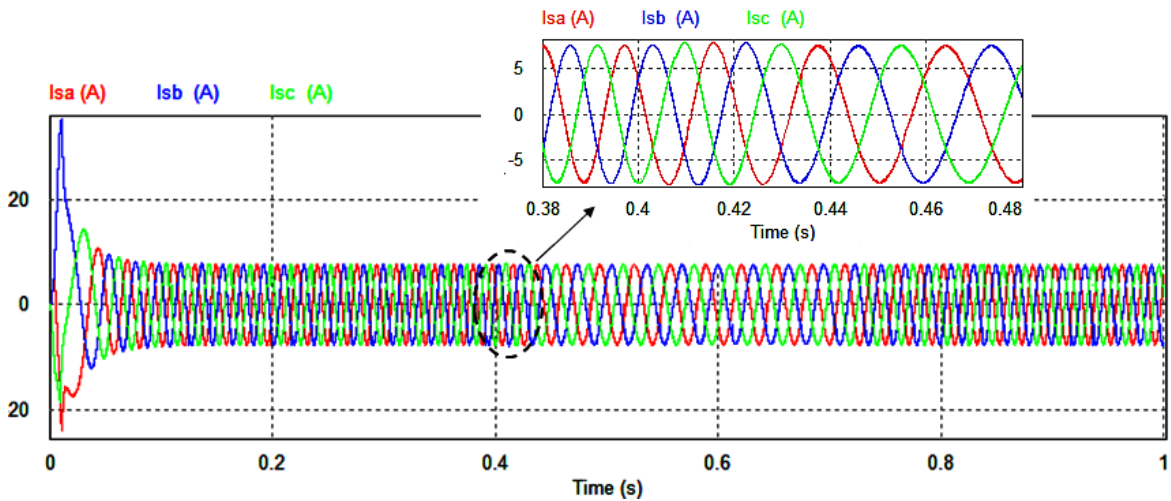
Fig. 5.13 stator currents of induction motor

Despite the change of half of the solar radiation at $t = 0.4\ s$, the amplitude of the stator currents remain stable around $I_{eff} = 7.6/\sqrt{2} = 5.37A$, only the frequency varies. Stator current frequencies are changed depending on the speed control. This shows the performance

of the inner current control loop (Fig. 5.13).

It should be noted that the no-load stator current is larger than the stator current of the induction motor. This is due to the design and construction of induction motors (IM) with a higher pole number in a small diameter.
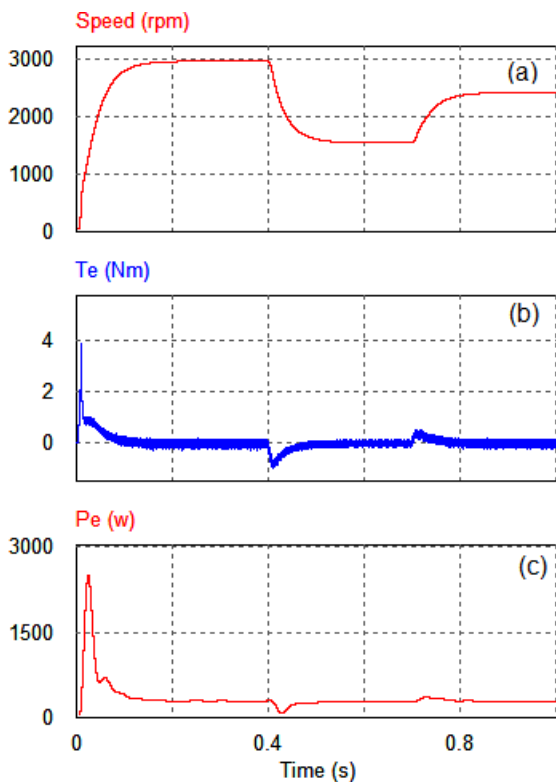
Fig. 5.14 Rotor speed, torque and electrical power response of IFOC
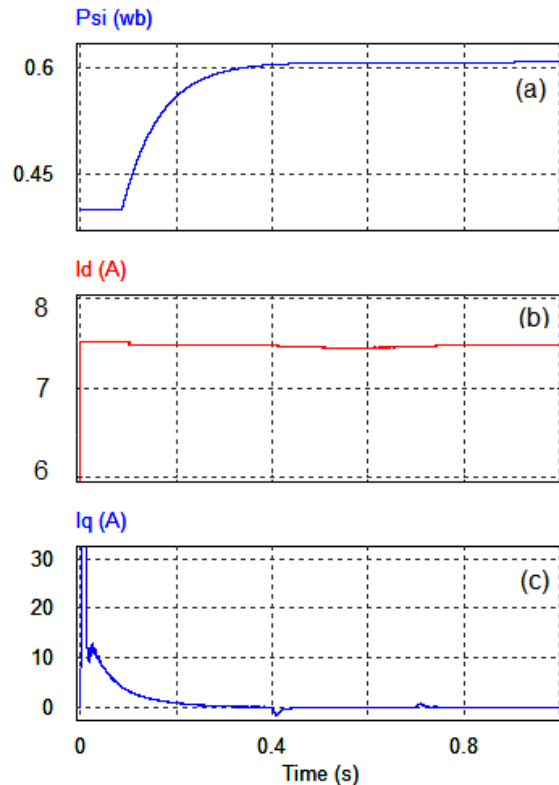
Fig. 5.15 Rotor flux, d-axis current and d-axis current response

Figure 5.14 shows the speed response of the rotor, which is proportional with the irradiance. In steady state, the motor rotates at a speed of approximately 2900 rpm, confirming that the output frequency of the inverter is 50 Hz. The variation in power supply does not greatly affect the electromagnetic torque as shown in 5.14 (b). The electric power absorbed by the induction motor operating at no load is shown in Figure 5.14 (c).

The rotor flux reaches a value of 0.6 Wb after 0.3 s, The change in solar irradiation did not affect the rotor flux. The quadrature current is the image torque; they have the same shape as shown in Fig 5.15.

5.6.2   Case study-II: Stabilization of solar irradiation with the introduction of the load

In this scenario, the system is initially started without load, then a nominal load torque of 13 Nm is introduced (Fig. 5.16.c). From Fig. 5.16 it can be seen that when the irradiations are at the maximum $(1000 \, W/m^2)$, the IM operates without load at a speed of 2900 rpm. The motor reaches its rated speed in 0.05 s. The stator currents are close to their nominal values and the electromagnetic torque is zero in steady state. At $t = 0.4 \, s$ a nominal load torque of $13 Nm$ is introduced. The stator currents are higher than in the no-load case (Fig. 5.16.a), but the rotor speed remains the same as before as shown in (Fig. 5.16.b).

 Figure 5.17 shows the powers and the flow produced by the pump, the maximum of the
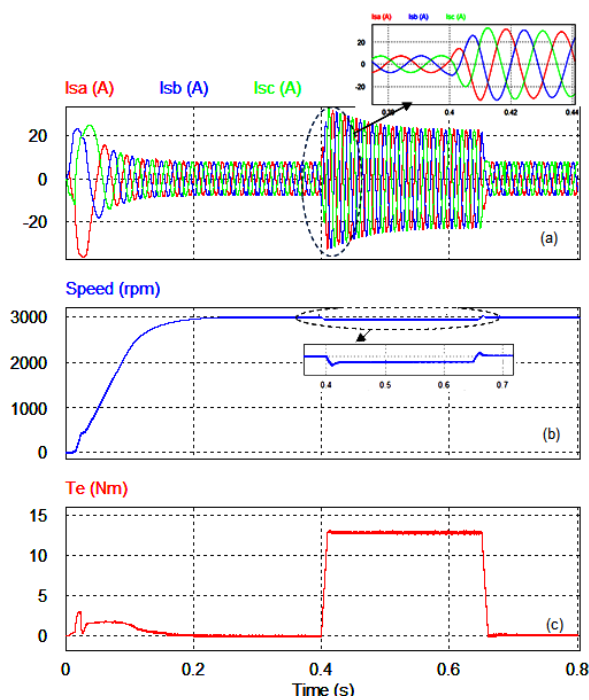
Fig. 5.16 Stator current, rotor speed and torque response of IFOC
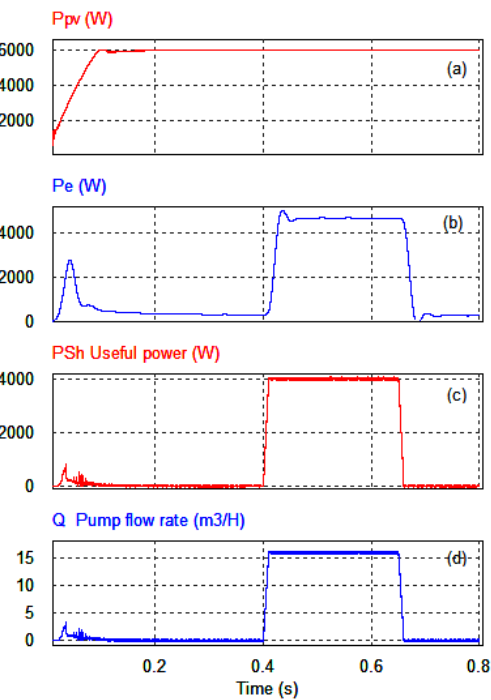
Fig. 5.17 GPV output power, electrical and useful power, and pump flow rate

power delivered by the PV generator with the irradiation of $(1000 \, W/m^2)$ is $P_{pv} = 6.0 \, kW$ (Fig. 5.17.a). The power absorbed by the motor is the same as the electric power, which is equal to $\sqrt{3}vi \cos\phi = 220 \times 16.41 \times \sqrt{3} \times 0.8 = 4.9 \, Kw$ (Fig. 5.17.b). It can be noticed that the no-load power in steady-state does not exceed $300 \, W$, and the useful power is zero because of no-load, therefore no water is pumped.

After t = 0.4 s, the pump is switched on, the motor requires more energy, and the current increases $I_{eff} = 22.06/\sqrt{2} = 15.59 \, A$, the electric power is at the maximum $P_e = vi\sqrt{3}PF =$

4.755 kW, the power transmitted to the pump is $P_{Sh} = 3.9 \, kW$ (Fig. 5.17.c). the water flow is also at max $Q = 15.3 \, m^3/H$ (Fig. 5.17.d).

5.6.3 Case study-III: Starting with load and changing in solar irradiance
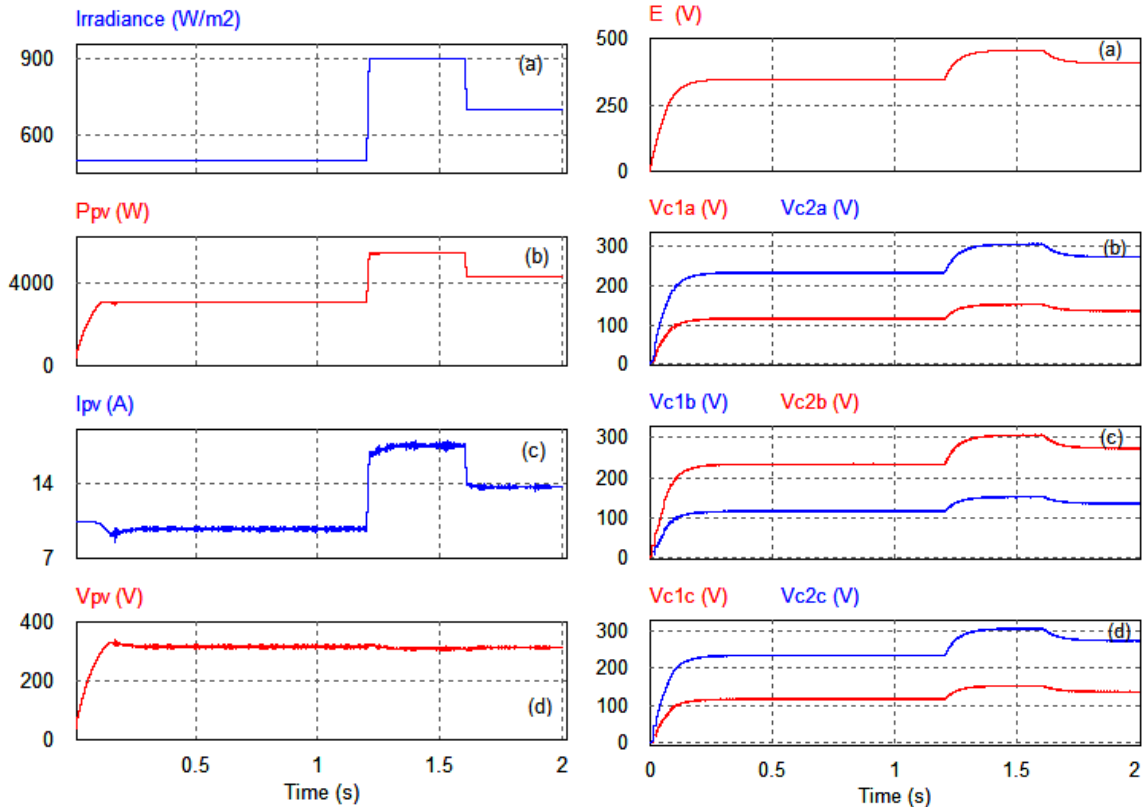
Fig. 5.18 Irradiance, GPV output power, current and voltage

Fig. 5.19 Input dc voltage, Floating voltages (Vc1 and Vc2 a,b,c)

In this case, starting the motor under load (pump) with variable solar irradiation, this is the practical case because this motor is hermetically closed coupled to the pump body. The entire assembly is submerged in the fluid to be pumped.

The following figures illustrate over two seconds.

The simulation is performed under rapidly varying solar irradiation levels starting at $500 \, W/m^2$, then is increased to $900 \, W/m^2$ at 1.2s to be dropped down to $700 \, W/m^2$ at the time of 1.6s (Fig. 5.18.a).

Figure 5.18.b shows that, the *MP&O* accurately tracked the maximum power point under varying irradiation levels. The simulation results show good steady-state performance. The

oscillation around the peak power point has been eliminated in the steady-state.

The PV array current and voltage are shown in Fig 5.18.c It is obvious that the PV array current changes when the PV system is subjected to change in the irradiation. Therefore, the the voltage is slightly changed (Fig 5.18.d).

From Figure 5.19 can be easily verified that the floating voltages across capacitors (V_{c1}) and (V_{c2}) of each phase converge towards their references $E/3$ and $2E/3$ respectively.

The speed of the pump motor is depicted in Fig. 5.20.a and the torque in Fig. 5.20.b. it is
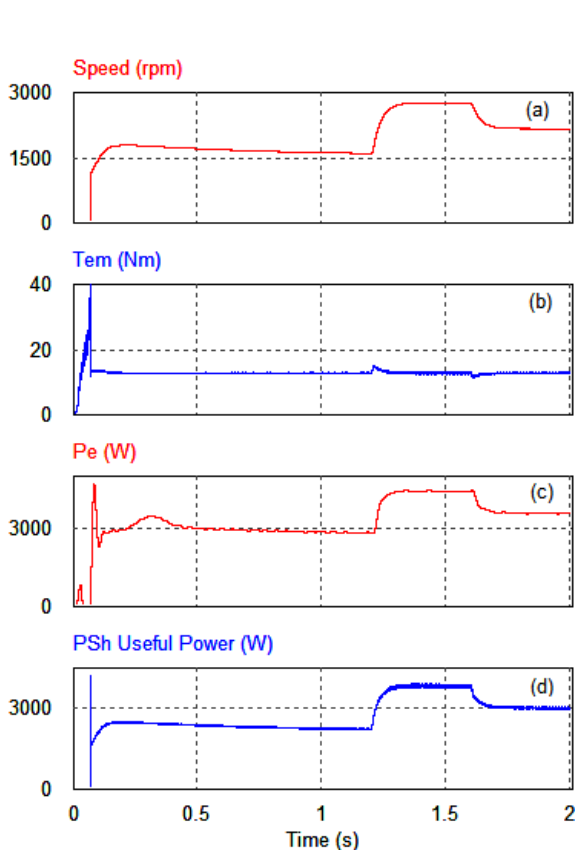
Fig. 5.20 Rotor speed, torque, Electrical and useful Power response
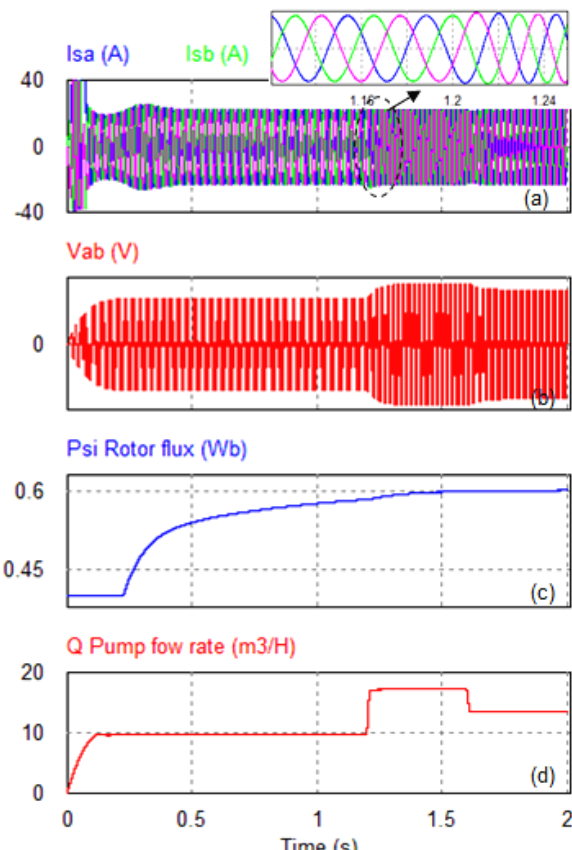
Fig. 5.21 Stator current, Vab voltage, rotor flux, and pump flow rate response

constant over time $(13Nm)$, The electric power absorbed by the motor is important because of the starting at the transient regime, at the steady state converges towards pv 3000 W and after increasing the maximum power (Fig. 5.20.c). The power received by the pump (P_{Sh}) to convert into hydraulic energy set illustrated by the figure 5.20.d.

The stator currents remain stable in amplitude (nominal values) and vary with the solar radiation; this is due to the current controller $I_{eff} = 23/\sqrt{2} = 16.26\,A$ (Fig. 5.21.a), therefore the magnitude of the voltages between the phases changes with the change of the DC voltage (Fig. 5.21.b).

Starting under load does not affect the flow. The response is the same as in the case of starting without load (Fig. 5.21.c). The water flow rate varies proportionally with solar irradiation, as seen in Figure 5.21.d).
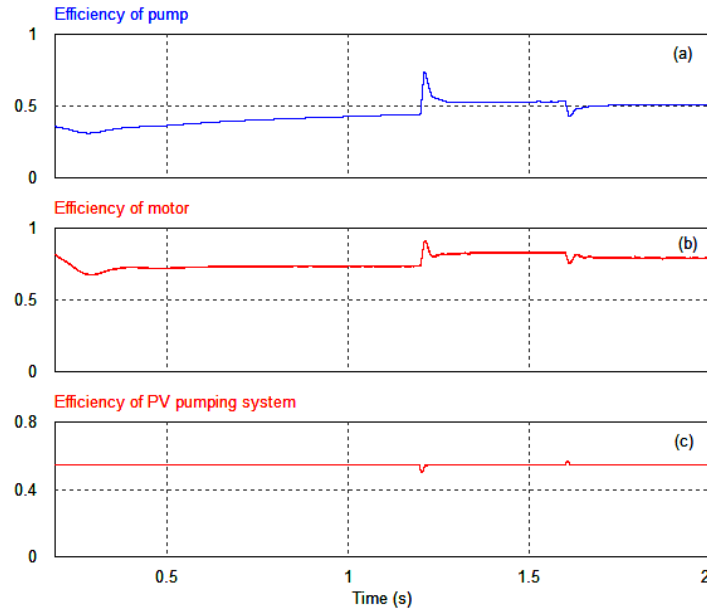
Fig. 5.22 Efficiency of the pump, motor and PV system

The efficiency of the pump, motor, and PV system is illustrated in figure 5.22. The pump efficiency is defined as the ratio of Hydraulic power to output (P_H) from the pump to the shaft power input for the pump (P_{Sh}). The efficiency of pump increases with the increase in solar radiation, In addition, this efficiency increases with the decrease in pumping head, while the efficiency of IM is related to the mechanical power supplied to the load.
The efficiency of the pump is about 0.54 as seen previously by the data given by the manufacturer.

5.7   Conclusion

Stand-alone Photovoltaic System based on a multi-cell voltage inverter that powers an induction motor is presented. This configuration allowed maintaining the energy balance between PV and load, as well as reducing energy waste. IM modelling is studied, followed by the modelling and calculation of the pump and the required power of IM.
Sliding mode control strategy of voltage source inverter based on load current compared with LS strategies, the novel control strategy has the superiority of simplicity and adaptability to

three-phase inverter. Thus, the HSMC strategy is more attractive to stand-alone PV systems than others. Finally, the performance and simulation results of the given system are shown the feasibility, reliability and dynamic performance of the new controller for pumping PV system.

Chapter 6

Conclusion

Chapter 6

Conclusion

This research work focused on the modeling and control design of a solar photovoltaic water pumping system. The different components of a photovoltaic energy conversion system have been presented. In this proposed PV systems configuration, a submersible pump has been connected as a load to a three-phase squirrel-cage IM powered by a multi-cell inverter. The entire system has been powered by a GPV.

In the first section the Loop-Shaping control is presented for the control of a high gain boost converter with a midpoint to generate the impulses. Loop shaping (LS) involves selecting the frequency domain characteristics of the open and closed-loop systems and specifying the desired performance and robustness before designing the controller, The controller was successfully implemented on the system and produced the desired results.

A new cascaded hybrid robust loop shaping control of three cell inverter has been developed. The three cells instantaneous model is derived and the control scheme was formulated as two cascaded current/voltages loops. Then, the hybrid model of the inverter is discussed. Next, a new algebraic condition is introduced to fulfill the adjacency constraint that allows minimizing energy losses.

Of particular importance is the asymptotic stability of the overall control system and this is proven by Lyapunov theory using a suitable Lyapunov function. In this algorithm, the states of the inverter are directly controlled by a predefined selection table chosen such as to force the Lyapunov function time derivative to be negative.

The feasibility and effectiveness of the proposed control scheme are assessed through extensive simulations. A HLS controller, designed offline, was used with a predefined selection table to control the switches. The results obtained show that the proposed control scheme is more efficient and robust compared to existing approaches. In addition, the proposed

approach is very simple to implement and requires a low computation time which makes it suitable for real-time applications.

Despite LS being a robust and reliable control strategy, however, when system parameters are changed, the controller transfer function need to be redesigned. It has been found that sliding mode control of the current loop in cascade with a hybrid algorithm of the voltage loop was appropriate.
HSMC is proposed to regulate the current from the PV system to the load. Finally, a new controller for the PV pumping system based on a multi cell voltage inverter feeding three-phase squirrel cage induction motor (IM) is proposed.
The sliding mode control strategy of voltage source inverter based on load current has been compared with LS strategies and the proposed new control strategy gave superior performance. It is simple and can be easily adapted to a three-phase inverter. Thus, the HSMC strategy is more attractive for stand-alone PV systems than others. Finally, the feasibility, reliability and dynamic performance of the new controller for pumping PV system have been assessed via extensive simulations and the results have been presented and discussed.

The proposed cascade control has been successfully implemented and tested in the case of a three-cell inverter. In a comparison of the proposed algorithms SMC and LS, the control has been improved, including response time, dynamic performance, and algorithm stability.

Proposed Future Work

For future work we propose:

- The design of an experimental set up for the stand-alone PV systems and analyze the frequency response of the system with and without battery.

- The Installation of a monitoring system to remotely control, evaluate, and guarantee photo- voltaic performance, as well as fault detection for increased reliability.

- The design and implementation of new algorithm using different photovoltaic system configurations appropriate for the site.

- It would be better to replace the IFOC command of the IM command with another powerful command that is unaffected by motor parameters.

References

References

[1] Abdel-Salam, M., El-Mohandes, M. T., and El-Ghazaly, M. (2020). An efficient tracking of mpp in pv systems using a newly-formulated p&o-mppt method under varying irradiation levels. *Journal of Electrical Engineering & Technology*, 15(1):501–513.

[2] Abouadane, H., Fakkar, A., Sera, D., Lashab, A., Spataru, S., and Kerekes, T. (2020). Multiple-power-sample based p&o mppt for fast-changing irradiance conditions for a simple implementation. *IEEE Journal of Photovoltaics*, 10(5):1481–1488.

[3] Ahmed, M. T., Rashel, M. R., Faisal, F., TlemÃ, M., et al. (2020). Non-iterative mppt method: A comparative study. *International Journal of Renewable Energy Research (IJRER)*, 10(2):549–557.

[4] Aktas, M., Awaili, K., Ehsani, M., and Arisoy, A. (2020). Direct torque control versus indirect field-oriented control of induction motors for electric vehicle applications. *Engineering Science and Technology, an International Journal*, 23(5):1134–1143.

[5] Ali, J. S. M. and Krishnaswamy, V. (2018). An assessment of recent multilevel inverter topologies with reduced power electronics components for renewable applications. *Renewable and Sustainable Energy Reviews*, 82:3379–3399.

[6] Alkarrami, F., Iqbal, T., Pope, K., Rideout, G., et al. (2020). Dynamic modelling of submersible pump based solar water-pumping system with three-phase induction motor using matlab. *Journal of Power and Energy Engineering*, 8(02):20.

[7] Almér, S., Mariéthoz, S., and Morari, M. (2010). Piecewise affine modeling and control of a step-up dc-dc converter. In *Proceedings of the 2010 American Control Conference*, pages 3299–3304. IEEE.

[8] Alskran, F. and Simões, M. G. (2020). Multilevel current source converter-based statcom suitable for medium-voltage applications. *IEEE Transactions on Power Delivery*, 36(2):1222–1232.

[9] Antoniewicz, K., Jasinski, M., Kazmierkowski, M. P., and Malinowski, M. (2016). Model predictive control for three-level four-leg flying capacitor converter operating as shunt active power filter. *IEEE transactions on industrial electronics*, 63(8):5255–5262.

[10] Aroussi, H. A., Ziani, E., Bouderbala, M., and Bossoufi, B. (2020). Improvement of direct torque control applied to doubly fed induction motor under variable speed. *International Journal of Power Electronics and Drive Systems*, 11(1):97.

[11] Ashari, A. B., Suprianto, B., and Hermawan, A. C. (2020). Kontrol kecepatan motor induksi menggunakan metode field orientation control (foc) berbasis fuzzy-pid. *Jurnal Teknik Elektro*, 9(3):763–771.

[12] Atoyebi, A., Akinnuli, B., and Ajobo, J. (2015). Total dynamic head determination model for submersible pumps installation. *International Journal of Applied Science and Technology*, 5(1):95–102.

[13] Bakar Siddique, M. A., Asad, A., Asif, R. M., Rehman, A. U., Sadiq, M. T., and Ullah, I. (2021). Implementation of incremental conductance mppt algorithm with integral regulator by using boost converter in grid-connected pv array. *IETE Journal of Research*, pages 1–14.

[14] Basabi, S. T. and Farzanehfard, H. (2020). Novel transistor-less series power decoupling in conventional current source inverter for pv application. In *2020 11th Power Electronics, Drive Systems, and Technologies Conference (PEDSTC)*, pages 1–5. IEEE.

[15] Bayod-Rújula, Á.-A. and Cebollero-Abián, J.-A. (2014). A novel mppt method for pv systems with irradiance measurement. *solar energy*, 109:95–104.

[16] Bechouche, A., Sediki, H., Abdeslam, D. O., and Haddad, S. (2011). A novel method for identifying parameters of induction motors at standstill using adaline. *IEEE Transactions on Energy Conversion*, 27(1):105–116.

[17] Beg, O. A., Abbas, H., Johnson, T. T., and Davoudi, A. (2017). Model validation of pwm dc–dc converters. *IEEE Transactions on Industrial Electronics*, 64(9):7049–7059.

[18] Benmansour, K., Benalia, A., Djemai, M., and De Leon, J. (2007). Hybrid control of a multicellular converter. *Nonlinear Analysis: Hybrid Systems*, 1(1):16–29.

[19] Benmansour, K., Djemai, M., Tadjine, M., and Boucherit, M. (2008). On sliding mode observer for hybrid three cells converter: Experimental results. pages 373–377.

[20] Bharath, K. and Suresh, E. (2017). Design and implementation of improved fractional open circuit voltage based maximum power point tracking algorithm for photovoltaic applications. *International Journal of Renewable Energy Research (IJRER)*, 7(3):1108–1113.

[21] Bhattacharjee, B., Sadhu, P. K., Ganguly, A., and Naskar, A. K. (2021). Integrated green submersible pumping system for future generation. *Facta Universitatis, Series: Electronics and Energetics*, 34(1):037–051.

[22] Bollipo, R. B., Mikkili, S., and Bonthagorla, P. K. (2020). Critical review on pv mppt techniques: classical, intelligent and optimisation. *IET Renewable Power Generation*, 14(9):1433–1452.

[23] Boonmee, C. and Kumsuwan, Y. (2013). Control of single-phase cascaded h-bridge multilevel inverter with modified mppt for grid-connected photovoltaic systems. In *IECON 2013-39th Annual Conference of the IEEE Industrial Electronics Society*, pages 566–571. IEEE.

[24] Boudjana, S. and Tadjine, M. (2019). On cascaded loop-shaping/hybrid mode control design of three-cell inverter. *Electrical Engineering*, pages 1–13.

[25] Bourhichi, S. E., Oukassi, A., Bahir, L. E., and Adnani, M. E. (2021). Indirect vector control of induction motor based on five-level inverter cascaded h-bridge using space vector modulation. In *2021 8th International Conference on Electrical and Electronics Engineering (ICEEE)*, pages 112–116. IEEE.

[26] Brinner, T. R., McCoy, R. H., and Kopecky, T. (2013). Induction versus permanent-magnet motors for electric submersible pump field and laboratory comparisons. *IEEE Transactions on industry applications*, 50(1):174–181.

[27] Caracas, J. V. M., de Carvalho Farias, G., Teixeira, L. F. M., and de Souza Ribeiro, L. A. (2013). Implementation of a high-efficiency, high-lifetime, and low-cost converter for an autonomous photovoltaic water pumping system. *IEEE Transactions on Industry Applications*, 50(1):631–641.

[28] Chandak, S., Bhowmik, P., and Rout, P. K. (2020). Dual-stage cascaded control to resynchronise an isolated microgrid with the utility. *IET Renewable Power Generation*, 14(5):871–880.

[29] Cheerangal, M. J., Jain, A. K., and Das, A. (2020). Control of rotor field oriented induction motor drive during input supply voltage sag. *IEEE Journal of Emerging and Selected Topics in Power Electronics*.

[30] Chen, C. and Yu, H. (2020). Backstepping sliding mode control of induction motor based on disturbance observer. *IET Electric Power Applications*, 14(12):2537–2546.

[31] Chen, M., Fong, Y.-C., and Loh, P. C. (2020). A cascaded flying capacitor multilevel inverter with double-boost voltage gain and reduced capacitor count for solar pv systems. In *2020 8th International Conference on Power Electronics Systems and Applications (PESA)*, pages 1–4. IEEE.

[32] Chigane, K. and Ouassaid, M. (2019). Improvement of power quality using back-stepping control strategy for a transformerless dual-stage grid-connected photovoltaic system. In *Recent Advances in Electrical and Information Technologies for Sustainable Development*, pages 193–200. Springer.

[33] Cortes, B., Araujo, L. R., and Penido, D. R. (2019). Electrical submersible pump system model to assist oil lifting studies. *Journal of Petroleum Science and Engineering*, 174:1279–1289.

[34] Costabeber, A., Carraro, M., and Zigliotto, M. (2014). Convergence analysis and tuning of a sliding-mode ripple-correlation mppt. *IEEE Transactions on Energy Conversion*, 30(2):696–706.

[35] Deng, F., Lü, Y., Liu, C., Heng, Q., Yu, Q., and Zhao, J. (2020). Overview on submodule topologies, modeling, modulation, control schemes, fault diagnosis, and tolerant control strategies of modular multilevel converters. *Chinese Journal of Electrical Engineering*, 6(1):1–21.

[36] Devanshu, A., Singh, M., and Kumar, N. (2020). Adaptive predictive current control of field-oriented controlled induction motor drive. *IETE Journal of Research*, pages 1–13.

[37] Diaz, J. M., Costa-Castello, R., and Dormido, S. (2019). Closed-loop shaping linear control system design: an interactive teaching/learning approach [focus on education]. *IEEE Control Systems Magazine*, 39(5):58–74.

[38] Dimitrijević, M., Stošović, M. A., and Litovski, V. (2020). An mppt controller model for a standalone pv system. *International Journal of Electronics*, 107(8):1345–1363.

[39] Domínguez, J. R., Dueñas, I., and Ortega-Cisneros, S. (2020). Discrete-time modeling and control based on field orientation for induction motors. *IEEE Transactions on Power Electronics*, 35(8):8779–8793.

[40] Dorf, R. C. and Bishop, R. H. (2011). *Modern control systems*. Pearson.

[41] Ebrahimi, J. and Karshenas, H. (2018). N-tuple flying capacitor multicell converter—a generalized modular hybrid topology. *IEEE Transactions on Industrial Electronics*, 66(7):5004–5014.

[42] El Merrassi, W., Abounada, A., and Ramzi, M. (2021). Advanced speed sensorless control strategy for induction machine based on neuro-mras observer. *Materials Today: Proceedings*.

[43] Elnozahy, A., Yousef, A. M., Abo-Elyousr, F. K., Mohamed, M., and Abdelwahab, S. A. M. (2021). Performance improvement of hybrid renewable energy sources connected to the grid using artificial neural network and sliding mode control. *Journal of Power Electronics*, pages 1–14.

[44] Elsanabary, A. I., Konstantinou, G., Mekhilef, S., Townsend, C. D., Seyedmahmoudian, M., and Stojcevski, A. (2020). Medium voltage large-scale grid-connected photovoltaic systems using cascaded h-bridge and modular multilevel converters: A review. *IEEE Access*, 8:223686–223699.

[45] Fallahzadeh, S. A. A., Abjadi, N. R., Kargar, A., and Blaabjerg, F. (2021). Applying sliding-mode control to a double-stage single-phase grid-connected pv system. *Journal of Renewable Energy and Environment*, 8(1):1–12.

[46] Feroz Mirza, A., Mansoor, M., Ling, Q., Khan, M. I., and Aldossary, O. M. (2020). Advanced variable step size incremental conductance mppt for a standalone pv system utilizing a ga-tuned pid controller. *Energies*, 13(16):4153.

[47] Filipe, J., Bessa, R. J., Reis, M., Alves, R., and Póvoa, P. (2019). Data-driven predictive energy optimization in a wastewater pumping station. *Applied Energy*, 252:113423.

[48] Gateau, G., Maussion, P., and Meynard, T. (1997). De la mod{\{}'e{\}}lisation a la commande non lin{\{}'e{\}}aire des convertisseurs multicellulaires s{\{}'e{\}}rie. application {\{}'a{\}} la fonction hacheur. *Journal de Physique III*, 7(6):1277–1305.

[49] Gevorkov, L. and Šmídl, V. (2020). Simulation model for efficiency estimation of photovoltaic water pumping system. In *2020 19th International Symposium INFOTEH-JAHORINA (INFOTEH)*, pages 1–5. IEEE.

[50] Ghanes, M., Trabelsi, M., Abu-Rub, H., and Ben-Brahim, L. (2016). Robust adaptive observer-based model predictive control for multilevel flying capacitors inverter. *IEEE transactions on industrial electronics*, 63(12):7876–7886.

[51] Ghedhab, N., Youcefettoumi, F., Loukriz, A., and Jouama, A. (2020). Maximum power point tracking for a stand-alone photovoltaic system using artificial neural network. In *E3S Web of Conferences*, volume 152, page 01007. EDP Sciences.

[52] Ghlib, I., Messlem, Y., and Chedjara, Z. (2019). Adaline-based speed control for induction motor drive. In *2019 International Conference on Advanced Electrical Engineering (ICAEE)*, pages 1–6. IEEE.

[53] Gopal, B. V., Shivakumar, E., and Ramesh, H. (2020). An experimental setup for implementation of fuzzy logic control for indirect vector-controlled induction motor drive. In *Advances in Control Instrumentation Systems*, pages 193–203. Springer.

[54] GRUNDFOS (2021). Grundfos data booklet. sp a, sp. submersible pumps, motors and accessories. 50 hz.

[55] Guo, B., Su, M., Sun, Y., Wang, H., Dan, H., Tang, Z., and Cheng, B. (2019). A robust second-order sliding mode control for single-phase photovoltaic grid-connected voltage source inverter. *IEEE Access*, 7:53202–53212.

[56] Guo, B., Su, M., Sun, Y., Wang, H., Liu, B., Zhang, X., Pou, J., Yang, Y., and Davari, P. (2020). Optimization design and control of single-stage single-phase pv inverters for mppt improvement. *IEEE Transactions on Power Electronics*, 35(12):13000–13016.

[57] Haddadi, K., Gazzam, N., and Benalia, A. (2019). Algebraic observer design for switched linear systems applied to multicellular converters for estimating capacitor voltages. *Electrotehnica, Electronica, Automatica*, 67(1):28–34.

[58] Hadole, M. V., Tiwari, K. N., and Bajpai, P. (2020). Energy generation and flow rate prediction of photovoltaic water pumping system for irrigation. *Environment, Development and Sustainability*, pages 1–12.

[59] Hammami, M., Grandi, G., and Rudan, M. (2016). An improved mppt algorithm based on hybrid rcc scheme for single-phase pv systems. In *IECON 2016-42nd Annual Conference of the IEEE Industrial Electronics Society*, pages 3024–3029. IEEE.

[60] Hammami, M., Ricco, M., Ruderman, A., and Grandi, G. (2019). Three-phase three-level flying capacitor pv generation system with an embedded ripple correlation control mppt algorithm. *Electronics*, 8(2):118.

[61] Hammoud, H. A. A. K. and Bazzi, A. M. (2020). Model-based mppt with corrective ripple correlation control. In *2020 IEEE Power and Energy Conference at Illinois (PECI)*, pages 1–6. IEEE.

[62] Hanafi, S., Fellah, M. K., Yaichi, M., and Benkhoris, M.-F. (2014). Nonlinear feedback decoupling control applied to stacked multicellular converter. *Rev. Roum. Sci. Techn.– {\{}'E}lectrotechn. et {\{}'E}nerg*, 59(1):97–106.

[63] Harrag, A. (2021). Modified p&o-fuzzy type-2 variable step size mppt for pem fuel cell power system. In *Advances in Renewable Hydrogen and Other Sustainable Energy Carriers*, pages 363–370. Springer.

[64] Heydari, E., Varjani, A. Y., and Diallo, D. (2020). Fast terminal sliding mode control-based direct power control for single-stage single-phase pv system. *Control Engineering Practice*, 104:104635.

[65] Hong, C.-M., Chen, C.-H., and Tu, C.-S. (2013). Maximum power point tracking-based control algorithm for pmsg wind generation system without mechanical sensors. *Energy conversion and management*, 69:58–67.

[66] Huda, M., Hidayat, M. N., Ronilaya, F., and Setiawan, A. (2018). Dual-stage flyback inverter controlled by sensorless current for microinverter. In *2018 International Conference on Information and Communications Technology (ICOIACT)*, pages 802–807. IEEE.

[67] Humayun, M., Khan, M. M., Hassan, M. U., and Zhang, W. (2021). Analysis of hybrid switches symmetric flying capacitor multilevel inverter based statcom. *International Journal of Electrical Power & Energy Systems*, 131:107054.

[68] Humayun, M., Khan, M. M., Muhammad, A., Xu, J., and Zhang, W. (2020). Evaluation of symmetric flying capacitor multilevel inverter for grid-connected application. *International Journal of Electrical Power & Energy Systems*, 115:105430.

[69] Ibrahim, W., Mohamed, M., and Ismail, R. (2020). Direct power control method of maximum power point tracking (mppt) algorithm for pico-hydrokinetic river energy conversion system. pages 691–703.

[70] Jday, M., Vidal, P.-E., Haggège, J., and Rotella, F. (2019). Observability and sliding mode observer design for multi-cell series converter. In *2019 6th international conference on control, decision and information technologies (CoDIT)*, pages 1486–1491. IEEE.

[71] Kariem, H., Touti, E., and Fetouh, T. (2020). The efficiency of pso-based mppt technique of an electric vehicle within the city. *Measurement and Control*, 53(3-4):461–473.

[72] Khan, K., Shukla, S., and Singh, B. (2020). Improved performance design realization of fractional kw induction motor with predictive current control for water pumping. *IEEE Transactions on Industry Applications*.

[73] Khodja, M., Rahiel, D., Benabdallah, M., Boulouiha, H. M., Allali, A., Chaker, A., and Denai, M. (2017). High-performance multicell series inverter-fed induction motor drive. *Electrical Engineering*, 99(3):1121–1137.

[74] Laamiri, S., Ghanes, M., and Santomenna, G. (2019). Observer based direct control strategy for a multi-level three phase flying-capacitor inverter. *Control Engineering Practice*, 86:155–165.

[75] Li, C., Yang, Y., Zhang, K., Zhu, C., and Wei, H. (2021a). A fast mppt-based anomaly detection and accurate fault diagnosis technique for pv arrays. *Energy Conversion and Management*, 234:113950.

[76] Li, J., Di, C., and Bao, X. (2021b). Efficiency improvement for submersible motors by optimizing the ratio of diameter to shaft length. *IEEE Transactions on Magnetics*.

[77] Liu, Y.-H., Chen, J.-H., and Huang, J.-W. (2015). A review of maximum power point tracking techniques for use in partially shaded conditions. *Renewable and Sustainable Energy Reviews*, 41:436–453.

[78] Lumbreras, D., Barrios, E. L., Balda, J., Gonzalez, R., and Sanchis, P. (2020). Novel three-phase topology for cascaded multilevel medium-voltage conversion systems in large-scale pv plants. In *2020 IEEE 21st Workshop on Control and Modeling for Power Electronics (COMPEL)*, pages 1–8. IEEE.

[79] Mahmud, S. (2020). *Development and Simulation of Maximum Power Point Tracking (MPPT) Controller with Ripple Correlation Control (RCC) for Deep Space Spacecraft*. PhD thesis, University of Toledo.

[80] Majumdar, S., Mahato, B., and Jana, K. C. (2019). Implementation of an optimum reduced components multicell multilevel inverter (mc-mli) for lower standing voltage. *IEEE Transactions on Industrial Electronics*, 67(4):2765–2775.

[81] Mehazzem, F., Reama, A., Charles, P., and Soubdhan, T. (2021). Integral backstepping improvement versus classical and multiscalar backstepping controllers for water im-pump fed by backstepping mppt pv source based on solar measurements in a tropical insular region. *IET Renewable Power Generation*.

[82] Menaga, D. and Sankaranarayanan, V. (2021). Performance comparison for grid connected photovoltaic system using sliding mode control. *Journal of King Saud University-Engineering Sciences*, 33(4):276–283.

[83] Menghal, P. M. and Laxmi, A. J. (2016). Modelling, simulation & analysis of induction motor using artificial intelligent controller. *International Journal of Modelling and Simulation*, 36(4):120–135.

[84] Meradi, S., Benmansour, K., Herizi, K., Tadjine, M., and Boucherit, M. (2013). Sliding mode and fault tolerant control for multicell converter four quadrants. *Electric power systems research*, 95:128–139.

[85] Meynard, T. A., Foch, H., Forest, F., Turpin, C., Richardeau, F., Delmas, L., Gateau, G., and Lefeuvre, E. (2002). Multicell converters: Derived topologies. *IEEE transactions on Industrial Electronics*, 49(5):978–987.

[86] Meziane, S., Toufouti, R., and Atarsia, L. (2021). Non-linear adaptive control of induction motor drive for standalone photovoltaic water pumping system. In *Handbook of Research on Modeling, Analysis, and Control of Complex Systems*, pages 450–476. IGI Global.

[87] Mishra, J., Das, S., Kumar, D., and Pattnaik, M. (2021). A novel auto-tuned adaptive frequency and adaptive step-size incremental conductance mppt algorithm for photovoltaic system. *International Transactions on Electrical Energy Systems*, page e12813.

[88] Mishra, S., Pradhan, S. K., and Rath, S. K. (2020). Network intrusion detection system using soft computing technique—fuzzy logic versus neural network: A comparative study. In *Cognitive Informatics and Soft Computing*, pages 627–634. Springer.

[89] Mohammadhassani, F. and Narm, H. G. (2021). Dynamic sliding mode control of single-stage boost inverter with parametric uncertainties and delay. *IET Power Electronics*.

[90] Mohanty, M. D. and Mohanty, M. N. (2020). Design of fuzzy controller for patients in operation theater. In *Cognitive Informatics and Soft Computing*, pages 547–555. Springer.

[91] Moosavi, M. and Toliyat, H. A. (2018). A multicell cascaded high-frequency link inverter with soft switching and isolation. *IEEE Transactions on Industrial Electronics*, 66(4):2518–2528.

[92] Mousa, H. H., Youssef, A.-R., and Mohamed, E. E. (2021). State of the art perturb and observe mppt algorithms based wind energy conversion systems: A technology review. *International Journal of Electrical Power & Energy Systems*, 126:106598.

[93] Mouton, H. T., Enslin, J. H., and Akagi, H. (2003). Natural balancing of series-stacked power quality conditioners. *IEEE transactions on power electronics*, 18(1):198–207.

[94] Muhsen, D. H., Khatib, T., and Nagi, F. (2017). A review of photovoltaic water pumping system designing methods, control strategies and field performance. *Renewable and Sustainable Energy Reviews*, 68:70–86.

[95] Muntashir, A. A., Purwanto, E., Sumantri, B., FAkhruddin, H. H., and Apriyanto, R. A. N. (2021). Static and dynamic performance of vector control on induction motor with pid controller: An investigation on labview. *Automotive Experiences*, 4(2):83–96.

[96] Murshid, S. and Singh, B. (2020). Single stage autonomous solar water pumping system using pmsm drive. *IEEE Transactions on Industry Applications*.

[97] Neumayr, D., Knabben, G. C., Varescon, E., Bortis, D., and Kolar, J. W. (2020). Comparative evaluation of a full-and partial-power processing active power buffer for ultra-compact single-phase dc/ac converter systems. *IEEE Journal of Emerging and Selected Topics in Power Electronics*.

[98] Ngan, M. D. H., Le Tien, D., and Phung, Q. N. (2021). Period doubling bifurcations and its control in induction motor drives. In *2020 Applying New Technology in Green Buildings (ATiGB)*, pages 6–11. IEEE.

[99] Nguyen, T. L., Vo, T. H., and Le, N. D. (2020). Backstepping control for induction motors with input and output constrains. *Engineering, Technology & Applied Science Research*, 10(4):5998–6003.

[100] Owusu-Nyarko, I., Elgenedy, M. A., and Ahmed, K. (2019). Combined temprature and irradiation effects on the open circuit voltage and short circuit current constants for enhancing their related pv-mppt algorithms. In *2019 IEEE Conference on Power Electronics and Renewable Energy (CPERE)*, pages 343–348. IEEE.

[101] Pan, J., Ke, Z., Al Sabbagh, M., Li, H., Potty, K. A., Perdikakis, W., Na, R., Zhang, J., Wang, J., and Xu, L. (2020). 7-kv 1-mva sic-based modular multilevel converter prototype for medium-voltage electric machine drives. *IEEE Transactions on Power Electronics*, 35(10):10137–10149.

[102] Peng, Z., Huibin, S., and Hongmei, K. (2019). An improved variable step size p&o mppt algorithm based on constant voltage and k division technology. In *Journal of Physics: Conference Series*, volume 1346, page 012026. IOP Publishing.

[103] Pichan, M., Arab Markadeh, G., and Blaabjerg, F. (2020). Continuous finite-time control of four-leg inverter through fast terminal sliding mode control. *International Transactions on Electrical Energy Systems*, 30(6):e12355.

[104] Pires, V. F., Foito, D., Baptista, F., and Silva, J. F. (2016). A photovoltaic generator system with a dc/dc converter based on an integrated boost-ćuk topology. *Solar Energy*, 136:1–9.

[105] Pires, V. F., Foito, D., and Silva, J. F. (2017). A single switch hybrid dc/dc converter with extended static gain for photovoltaic applications. *Electric Power Systems Research*, 146:228–235.

[106] Prabhakaran, K., Karthikeyan, A., Varsha, S., Perumal, B. V., and Mishra, S. (2020). Standalone single stage pv-fed reduced switch inverter based pmsm for water pumping application. *IEEE Transactions on Industry Applications*, 56(6):6526–6535.

[107] Pradhan, P. K., Roy, S., and Mohanty, A. (2019). Detection of broken impeller in submersible pump by estimation of rotational frequency from motor current signal. *Journal of Vibration Engineering & Technologies*, pages 1–8.

[108] Pragathi, B., Nayak, D. K., and Poonia, R. C. (2020). Mitigation of power quality issues for grid connected photo voltaic system using soft computing techniques. *Journal of Interdisciplinary Mathematics*, 23(2):631–637.

[109] Prayag, A., Bodkhe, S., and Raisoni, G. (2018). A comparative study of symmetrical and asymmetrical cascaded h bridge multilevel inverter topology for industrial drive. *International Research Journal of Engineering and Technology*, 5(2).

[110] Priyadarshi, N., Bhaskar, M. S., Padmanaban, S., Blaabjerg, F., and Azam, F. (2020a). New cuk–sepic converter based photovoltaic power system with hybrid gsa–pso algorithm employing mppt for water pumping applications. *IET Power Electronics*, 13(13):2824–2830.

[111] Priyadarshi, N., Bhoi, A. K., Sahana, S. K., Mallick, P. K., and Chakrabarti, P. (2020b). Performance enhancement using novel soft computing aflc approach for pv power system. In *Cognitive Informatics and Soft Computing*, pages 439–447. Springer.

[112] Priyadarshi, N., Bhoi, A. K., Sharma, A. K., Mallick, P. K., and Chakrabarti, P. (2020c). An efficient fuzzy logic control-based soft computing technique for grid-tied photovoltaic system. In *Cognitive Informatics and Soft Computing*, pages 131–139. Springer.

[113] Qi, W., Li, S., Tan, S.-C., and Hui, S. (2018). A single-phase three-level flying-capacitor pfc rectifier without electrolytic capacitors. *IEEE Transactions on Power Electronics*, 34(7):6411–6424.

[114] Rai, R., Shukla, S., and Singh, B. (2020). Sensorless field oriented smcc based integral sliding mode for solar pv based induction motor drive for water pumping. *IEEE Transactions on Industry Applications*.

[115] Rai, T. and Debre, P. (2016). Generalized modeling model of three phase induction motor. In *2016 International Conference on Energy Efficient Technologies for Sustainability (ICEETS)*, pages 927–931. IEEE.

[116] Remoaldo, D. and S Jesus, I. (2021). Analysis of a traditional and a fuzzy logic enhanced perturb and observe algorithm for the mppt of a photovoltaic system. *Algorithms*, 14(1):24.

[117] Ricco, M., Hammami, M., Mandrioli, R., and Grandi, G. (2020). Ripple correlation control mppt scheme applied to a three-phase flying capacitor pv system. In *ELECTRI-MACS 2019*, pages 13–24. Springer.

[118] Rosa, F. C. and Bim, E. (2020). A constrained non-linear model predictive controller for the rotor flux-oriented control of an induction motor drive. *Energies*, 13(15):3899.

[119] Sadanala, C., Pattnaik, S., and Singh, V. P. (2020). A flying capacitor based multilevel inverter architecture with symmetrical and asymmetrical configurations. *IEEE Journal of Emerging and Selected Topics in Power Electronics*.

[120] Sadigh, A. K. and Dargahi, V. (2020). Flying-capacitor voltage-balancing control in five-level active neutral-point-clamped (a-npc) converters using phase-disposition pwm. In *2020 IEEE Transportation Electrification Conference & Expo (ITEC)*, pages 1–6. IEEE.

[121] SAHOO, A. K., Das, S. R., Ray, P. K., Balasubramanian, K., and Reddy, G. S. (2020). Improvement of power quality in three phase system using adaline based multilevel inverter. *Frontiers in Energy Research*, 8:23.

[122] Sahoo, B., Routray, S. K., and Rout, P. K. (2021). Execution of robust dynamic sliding mode control for smart photovoltaic application. *Sustainable Energy Technologies and Assessments*, 45:101150.

[123] Sahu, P., Sharma, A., and Dey, R. (2020). Ripple correlation control maximum power point tracking for battery operated pv systems: A comparative analysis. In *2020 IEEE International IOT, Electronics and Mechatronics Conference (IEMTRONICS)*, pages 1–6. IEEE.

[124] Said, B., Mohamed, T., and Mohamed, F. (2017a). Characterization of bifurcation dynamics in multicell inverter. In *2017 6th international conference on systems and control (ICSC)*, pages 127–132. IEEE.

[125] Said, S. B., Saad, K. B., and Benrejeb, M. (2017b). Hil simulation approach for a multicellular converter controlled by sliding mode. *International journal of hydrogen energy*, 42(17):12790–12796.

[126] Saikumar, V. V., Sathyavani, B., and Suresh, J. (2020). Mathematical modeling of five-phase and three-phase induction motor and their result comparison. In *IOP Conference Series: Materials Science and Engineering*, volume 981, page 042059. IOP Publishing.

[127] Salam, Z. and Ahmed, J. (2014). The application of soft computing techniques to improve the performance of maximum power point tracker for pv system during partial shading. In *2014 IEEE 8th International Power Engineering and Optimization Conference (PEOCO2014)*, pages 237–242. IEEE.

[128] Saleh, A. L., Obed, A. A., Hassoun, Z. A., and Yaqoob, S. J. (2020). Modeling and simulation of a low cost perturb& observe and incremental conductance mppt techniques in proteus software based on flyback converter. In *IOP Conference Series: Materials Science and Engineering*, volume 881, page 012152. IOP Publishing.

[129] Salinas, F., Gonz{\{}’a}lez, M. A., Escalante, M. F., and de Le{\{}’o}n Morales, J. (2015). Control design strategy for flying capacitor multilevel converters based on petri nets. *IEEE Transactions on Industrial Electronics*, 63(3):1728–1736.

[130] Serrasolses, J., Vallvé, X., and Chiva, P. (2020). Pv systems for stand-alone electrification: The user's point of view. In *Sixteenth European Photovoltaic Solar Energy Conference*, pages 2884–2887. Routledge.

[131] Sheir, A., Youssef, M. Z., and Orabi, M. (2018). A novel bidirectional t-type multi-level inverter for electric vehicle applications. *IEEE Transactions on Power Electronics*, 34(7):6648–6658.

[132] Shrey, S., Subhankar, A., and Subhashree, A. (2020). Solar pv powered water pumping system – a review. *Materials Today: Proceedings*.

[133] Shukla, S. and Singh, B. (2018). Single-stage pv array fed speed sensorless vector control of induction motor drive for water pumping. *IEEE transactions on industry applications*, 54(4):3575–3585.

[134] Shukla, S. and Singh, B. (2020). Single stage pv-grid interactive induction motor drive with improved flux estimation technique for water pumping with reduced sensors. *IEEE Transactions on Power Electronics*.

[135] Singh, S. and HOD, P. S. (2021). Speed control analysis and performance comparison of induction motor using improved hybrid pid fuzzy controller.

[136] SUBBARAO, K. and KALYAN, K. P. (2021). Comparitive analysis of a mppt control techniques.

[137] Tabasian, R., Ghanbari, M., Esmaeli, A., and Jannati, M. (2021). Indirect field-oriented control of star-connected three-phase induction machine drives against single-phase open-circuit fault. *International Transactions on Electrical Energy Systems*, page e12873.

[138] Tiwari, A. K., Kalamkar, V. R., Pande, R. R., Sharma, S. K., Sontake, V. C., and Jha, A. (2020). Effect of head and pv array configurations on solar water pumping system. *Materials Today: Proceedings*.

[139] Travieso-Torres, J. C., Vilaragut-Llanes, M., Costa-Montiel, Á., Duarte-Mermoud, M. A., Aguila-Camacho, N., Contreras-Jara, C., and Álvarez-Gracia, A. (2020). New adaptive high starting torque scalar control scheme for induction motors based on passivity. *Energies*, 13(5):1276.

[140] Wang, D. and Chen, X. (2017). A tutorial on loop-shaping control methodologies for precision positioning systems. *Advances in mechanical engineering*, 9(12):1687814017742824.

[141] Wang, H., Long, B., Yang, Y., Xiao, Y., and Wang, C. (2020). Modelling the influence of inlet angle change on the performance of submersible well pumps. *Int. J. Simul. Model*, 19:100–111.

[142] Wang, Z. and Peng, L. (2020). Grouping capacitor voltage estimation and fault diagnosis with capacitance self-updating in modular multilevel converters. *IEEE Transactions on Power Electronics*, 36(2):1532–1543.

[143] Wibisono, G. (2019). Model mppt metode fractional short circuit current menggunakan jst-ag untuk solar panel. *Journal of Telecommunication, Electronics, and Control Engineering (JTECE)*, 1(01):63–69.

[144] Wilkinson, R. H., Meynard, T. A., and du Toit Mouton, H. (2006). Natural balance of multicell converters: The two-cell case. *IEEE Transactions on Power Electronics*, 21(6):1649–1657.

[145] Winarno, T., Palupi, L. N., Pracoyo, A., and Ardhenta, L. (2020). Mppt control of pv array based on pso and adaptive controller. *Telkomnika*, 18(2):1113–1121.

[146] Xia, Y., Roy, J., and Ayyanar, R. (2020). A single stage common ground three-level pv inverter with integrated power decoupling. *IEEE Open Journal of Power Electronics*, 1:227–237.

[147] YALÇIN, N. A. and VATANSEVER, F. (2020). Comparison of prony and adaline method in inter-harmonic estimation. *Uludağ University Journal of The Faculty of Engineering*, 25(1):405–418.

[148] Yang, S., Wang, P., and Tang, Y. (2017). Feedback linearization-based current control strategy for modular multilevel converters. *IEEE Transactions on Power Electronics*, 33(1):161–174.

[149] Yashin, A. and Khakimyanov, M. (2020). Characteristics analysis of linear submersible electric motors for oil production. In *2020 Russian Workshop on Power Engineering and Automation of Metallurgy Industry: Research & Practice (PEAMI)*, pages 15–19. IEEE.

[150] Zand, S. J., Hsia, K.-H., Eskandarian, N., and Mobayen, S. (2021). Improvement of self-predictive incremental conductance algorithm with the ability to detect dynamic conditions. *Energies*, 14(5):1234.

[151] Zhao, B., Abramovitz, A., Liu, C., Yang, Y., and Huangfu, Y. (2020a). A family of single-stage, buck-boost inverters for photovoltaic applications. *Energies*, 13(7):1675.

[152] Zhao, B., Huangfu, Y., and Abramovitz, A. (2020b). Derivation of occ modulator for grid-tied single-stage buck-boost inverter operating in the discontinuous conduction mode. *Energies*, 13(12):3168.

[153] Zhou, M., Cheng, S., Feng, Y., Xu, W., Wang, L., and Cai, W. (2021). Full-order terminal sliding-mode based sensorless control of induction motor with gain adaptation. *IEEE Journal of Emerging and Selected Topics in Power Electronics*.

Appendices

Appendix A
LG Neon2 330W Solar Panel Datasheet A

LG NeON 2 Black

Mechanical Properties

Cells	6 x 10
Cell Vendor	LG
Cell Type	Monocrystalline/N-type
Cell Dimensions	161.7 x 161.75 mm
# of Busbar	12 (Multi Wire Busbar)
Dimensions (L x W x H)	1,686 x 1,016 x 40 mm
Weight	17.1 kg
Mechanical Test Load*:	6,000 Pa (Front)
	5,400 Pa (Rear)
Junction Box	IP68 with 3 Bypass Diodes
Length of Cables	2 x 1,000 mm
Front cover	Tempered Glass with AR Coating
Frame	Anodized Aluminum

* Manufacturer Declaration according to IEC 61215 : 2005 (Preliminary)
# Mechanical Test Loads 5400 Pa / 4000 Pa based on IEC61215-2 : 2016
 (Test Load = Design Load x Safety Factor (1.5))

Certifications and Warranty

Certifications	IEC 61215-1/-1-1/2:2016, IEC 61730-1/2:2016
	ISO 9001, ISO 14001, ISO 50001
Salt Mist Corrosion Test	IEC 62701 : 2012 Severity 6
Ammonia Corrosion Test	IEC 62716 : 2013
Module Fire Performance	Class C, Fire class 2
Product Warranty	25 years
Output Warranty of Pmax (Measurement Tolerance ± 3%)	25 years linear warranty[1]

[1] 1) 1st year. min. 98 %. 2) After 2nd year. max. 0.35 % p annual degradation.
 3) Min. 89.6 % for 25 years.

Temperature Coefficients

NOCT	42 ± 3 °C
Pmpp	-0.36 %/°C
Voc	-0.27 %/°C
Isc	0.03 %/°C

Characteristic Curves
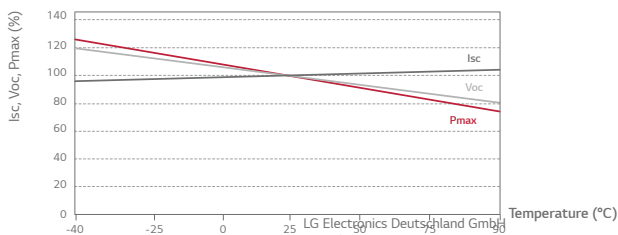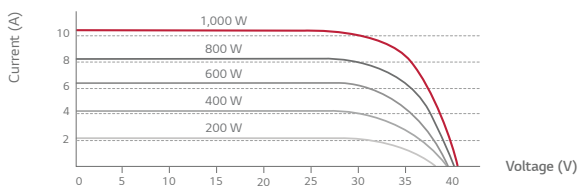
Electrical Properties (STC[2])

Model		LG330N1K-V5	LG325N1K-V5	LG320N1K-V5
Maximum Power Pmax	[W]	330	325	320
MPP Voltage Vmpp	[V]	34.1	33.7	33.3
MPP Current Impp	[A]	9.69	9.65	9.62
Open Circuit Voltage Voc	[V]	41.0	40.9	40.8
Short Circuit Current Isc	[A]	10.27	10.23	10.19
Module Efficiency	[%]	19.3	19.0	18.7
Operating Temperature	[°C]	-40 ~ +90		
Maximum System Voltage	[V]	1,000		
Maximum Series Fuse Rating	[A]	20		
Power Tolerance	[%]	0 ~ +3		

[2] 1) STC (Standard Test Condition): Irradiance 1,000 W/m², Module Temperature 25 °C, AM 1.5.

Electrical Properties (NMOT)

Model		LG330N1K-V5	LG325N1K-V5	LG320N1K-V5
Maximum Power Pmax	[W]	247	243	239
MPP Voltage Vmpp	[V]	31.9	31.5	31.2
MPP Current Impp	[A]	7.73	7.69	7.67
Open Circuit Voltage Voc	[V]	38.5	38.4	38.3
Short Circuit Current Isc	[A]	8.26	8.23	8.19

Dimensions (mm)

LONG FRAME

SHORT FRAME

The distance between the center of the mounting/grounding holes

LG Life's Good
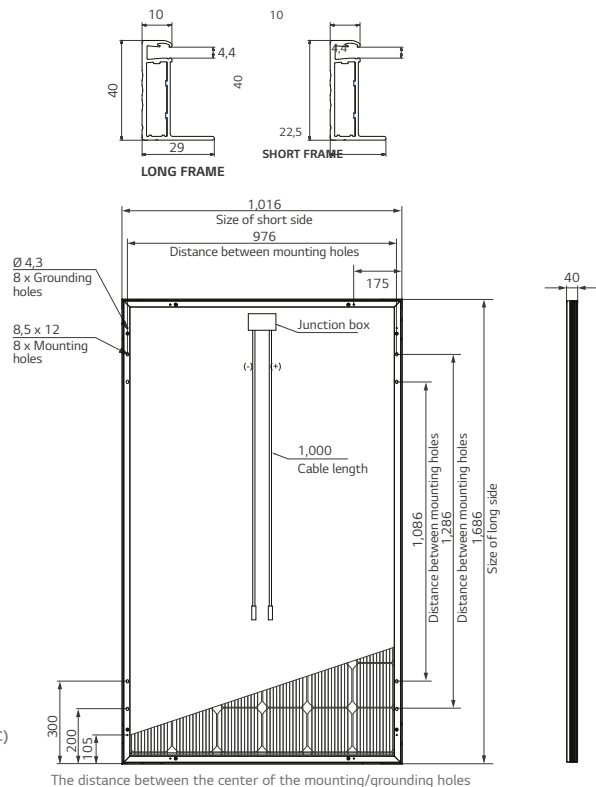
All details in this data sheet comply with DIN EN 50380.
Subject to errors and alterations.
Date: 02/2019
Document: DS-N1K-V5-EN-201902

Appendix B

GRUNDFOS ms4000 motor

GRUNDFOS	**Company name:** **Created by:** **Phone:** **Date:** 09/06/2021

Qty.	Description
1	**MS 4000**

Note! Product picture may differ from actual product

Product No.:   79104510

Phase: The motor is a 3-phase motor of the canned
type with sand shield, liquid-lubricated bearings
and pressure equalizing diaphragm.

Liquid:
Max liquid t at 0.15 m/sec: 40 °C

Technical:
Shaft seal for motor: HM/CER
Approvals on nameplate: CE,GOST2

Materials:
Motor: Stainless steel
                                               DIN W.-Nr. 1.4301
                                               AISI 304

Installation:
Maximum ambient pressure: 60 bar
Motor diameter: 4 inch

Electrical data:
Motor type: MS4000
Rated power - P2:   4 kW
Mains frequency: 50 Hz
Rated voltage: 3 x 220-230 V
Voltage tolerance: +6/-10 %
Rated current: 17.4-17.6 A
Starting current: 520-540 %
Cos phi - power factor: 0.80-0.77
Rated speed: 2865-2875 rpm
Locked-rotor torque: 180-200 %
Moment of inertia: 0.0022 kg m²
Start. method: direct-on-line
Enclosure class (IEC 34-5):   IP58
Insulation class (IEC 85):   F
Built-in temp. transmitter: no
Winding resistance: 1.38 ohm

Others:
Net weight: 21 kg

Appendix C

Performance curves and technical data SP 14

Performance curves for SP 14, 50 Hz, ISO 9906:2012 Grade 3B, showing head H [m] and pressure p [kPa] versus flow Q [m³/h] and Q [l/s] for pump curves -4, -6, -8, -11, -13, -15, -17, -20, -23, -27, -31.
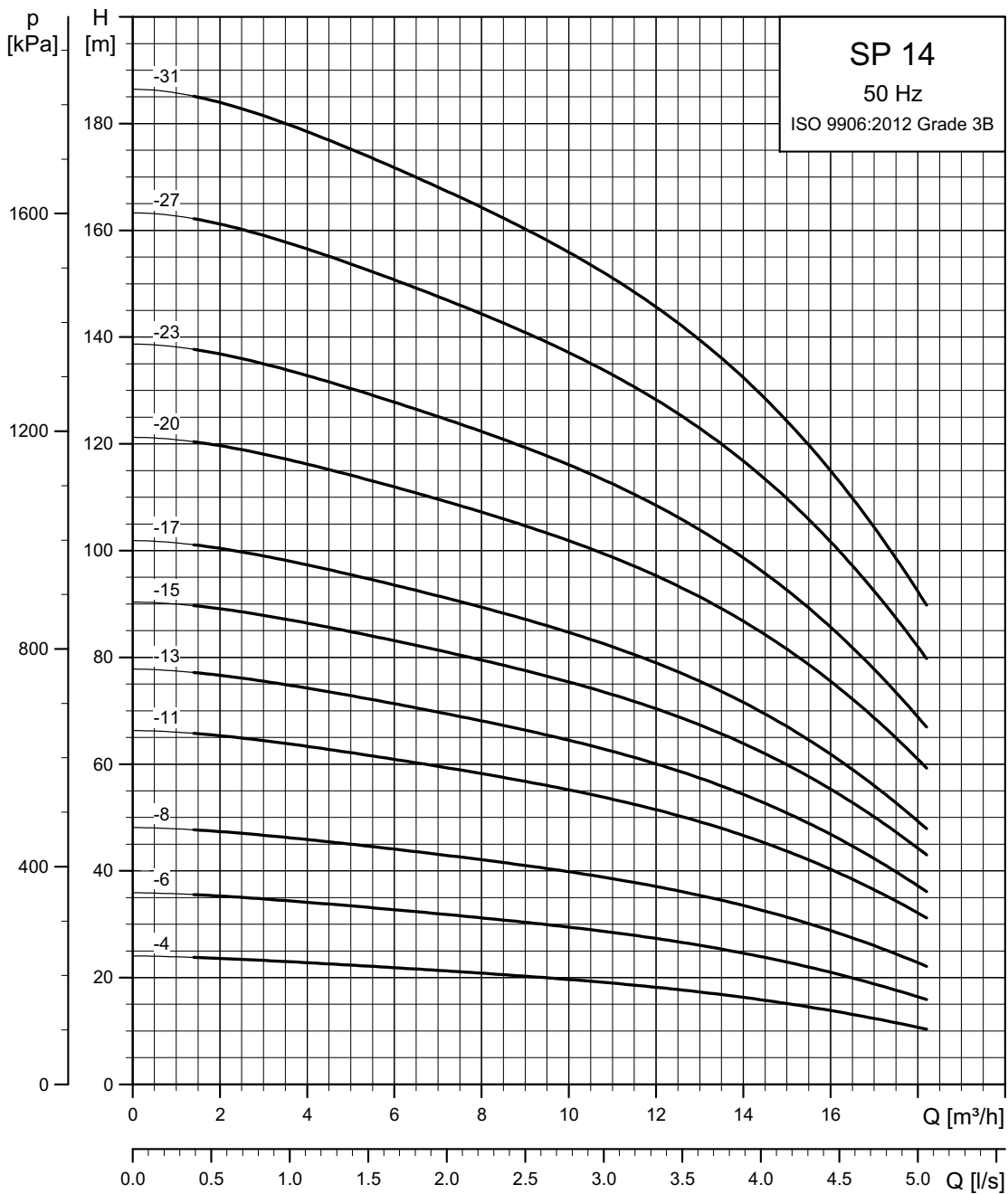
Appendix D

Calculate the moment of inertia SP 14

Moment of inertia

Calculate the moment of inertia by use of one of the formulas below. Choose the formula from pump and motor size 4", 6", 8", 10" or 12" and insert the number of stages.

Pump type		Moment of inertia [kgm^2]				
		Motor size 4"	Motor size 6"	motor size 8"	Motor size 10"	Motor size 12"
SP 1A	Splined shaft	$(9.4 + n \times 21.4) \times 10^{-6}$				
	Smoot shaft	$(11.7 + n \times 27.8) \times 10^{-6}$				
SP 1.5A	Splined shaft	$(9.4 + n \times 20.4) \times 10^{-6}$				
SP 2A	Splined shaft	$(9.4 + n \times 28.4) \times 10^{-6}$				
	Smoot shaft	$(11.7 + n \times 40.8) \times 10^{-6}$				
SP 3A	Splined shaft	$(9.4 + n \times 27.9) \times 10^{-6}$				
	Smoot shaft	$(11.7 + n \times 40.7) \times 10^{-6}$	$(415.68 + n \times 40.7) \times 10^{-6}$			
SP 5A	Splined shaft	$(9.4 + n \times 27.9) \times 10^{-6}$				
	Smoot shaft	$(11.7 + n \times 41.7) \times 10^{-6}$	$(415.97 + n \times 41.7) \times 10^{-6}$			
SP 7		$(0.5 + n \times 2.0) \times 10^{-4}$	$(4.0 + n \times 2.0) \times 10^{-4}$			
SP 9		$(0.5 + n \times 2.0) \times 10^{-4}$	$(4.0 + n \times 2.0) \times 10^{-4}$			
SP 11		$(0.5 + n \times 2.0) \times 10^{-4}$	$(4.0 + n \times 2.0) \times 10^{-4}$			
SP 14		$(0.5 + n \times 2.0) \times 10^{-4}$	$\color{red}{(4.0 + n \times 2.0) \times 10^{-4}}$			
SP 17		$(0.5 + n \times 2.0) \times 10^{-4}$	$(4.0 + n \times 2.0) \times 10^{-4}$			
SP 30		$(0.5 + n \times 5.1) \times 10^{-4}$	$(4.0 + n \times 5.1) \times 10^{-4}$	$(6.0 + n \times 5.1) \times 10^{-4}$		
SP 46		$(0.5 + n \times 3.6) \times 10^{-4}$	$(4.0 + n \times 3.6) \times 10^{-4}$	$(6.0 + n \times 3.6) \times 10^{-4}$		
SP 60		$(0.5 + n \times 4.1) \times 10^{-4}$	$(4.0 + n \times 4.1) \times 10^{-4}$	$(6.0 + n \times 4.1) \times 10^{-4}$		
SP 77			$(5.5 + n \times 19) \times 10^{-4}$	$(7.0 + n \times 19) \times 10^{-4}$		
SP 95			$(5.5 + n \times 22) \times 10^{-4}$	$(20 + n \times 22) \times 10^{-4}$		
SP 125			$(5.5 + n \times 33) \times 10^{-4}$	$(20 + n \times 33) \times 10^{-4}$	$(25 + n \times 33) \times 10^{-4}$	$(25 + n \times 33) \times 10^{-4}$
SP 160			$(5.5 + n \times 33) \times 10^{-4}$	$(20 + n \times 33) \times 10^{-4}$	$(25 + n \times 33) \times 10^{-4}$	$(25 + n \times 33) \times 10^{-4}$
SP 215			$(25 + n \times 100) \times 10^{-4}$	$(25 + n \times 100) \times 10^{-4}$	$(30 + n \times 100) \times 10^{-4}$	$(30 + n \times 100) \times 10^{-4}$

n = number of stages.